Quantum Tunneling and Heterodyne Detection in Superconducting Tunnel Junctions

A Dissertation

Presented to the Faculty of the Graduate School

of

Yale University

in Candidacy for the Degree of

Doctor of Philosophy

by

Nuray George Ugras

November, 1993

Abstract

Quantum Tunneling and Heterodyne Detection in Superconducting Tunnel Junctions

Nuray George Ugras

Yale University

1993

The quasiparticle susceptance and conductance of a superconducting tunnel junction was measured including the singularity in the quasiparticle susceptance at the gap voltage. Results are compared to existing theories of superconductive tunneling, and the results agree well with theory. An analogy to a two-level atomic system is developed to explain the photon assisted tunneling process and its dependence on the dc bias voltage and the signal frequency.

A w-band SIS receiver with no mechanical tuners was built. This receiver performed as well as other comparable receivers in its frequency range. Mixer gain larger than unity was observed over the full frequency band. The quasiparticle susceptance was utilized as a voltage controlled tuning element for a SIS mixer. This is the first integrated and electronically variable tuning element demonstrated for a SIS mixer.

Acknowledgments

I thank my advisor, Daniel Prober, for supporting me; for teaching me about the scientific research process; and especially for guiding me into the real world. Dag Winkler conceived most of the experiments and designed the mixer and the dewar. I thank him for being unselfish and patient with me. Bob Wheeler served on my committee, and was always very enthusiastic about my research. Peter Kindlmann gave me a philosophical (and practical) understanding of design. A Yale education is not complete without the long teach-ins by Stanley Mroczkovski on life; I hope I have learned. I also thank Richard Chang for serving on my committee, Jonas Zmuidzinas for acting as an external reader, and Oded Millo for his support.

Among my fellow students I thank Curt for his decadent tendencies; it is a good thing that we are leaving. Jim for his companionship during the many lonely conferences. Paul and Bruce (ex-Yalies) for the many coffee and Gypsy outings. I also thank the Prober Lab clan: Mike, Mark, Stefan, Anurag, Sean, and of past members Elie Track and especially Hodge Worsham.

Jayne Miller and Pat Brodka have been very supportive, and patient with my many complaints about science and life. I thank Katrina for providing food in desperate times and Mary Lally for keeping my paperwork in order. The technical staff at Yale made most of this project possible: Dicky, Dexter, Lou, Skip, Stanley, and Andy. There were many others at Yale who have helped me and were friends. I apologize for any omissions. Much technical help came from outside of Yale: Mike Rooks at Cornell, Neil Erickson and Paul Goldsmith at UMass, Toni Kerr and S. K. Pan at NRAO, A. Skalare at Chalmers, and Mark Feldman at Univ. of Rochester.

Anne Frederick's love and care lifted me from the many downfalls these past years. Her encouragement made it possible to finish this thesis. The last six years would have comprised a much different experience (and a more sober one) without the invaluable friendship of Blake Hill. I thank Bill Nelson for the intense backgammon-bourbon-discussion sessions. Laura Efros, Nancy Neiman, Carolyn Buser, Matty Woodruff, Betsy Bolton, and Michaela Kiernan have provided much support over the last six years. I thank Mucit for still being involved in my affairs and remaining such a good friend for 14 years.

Outside of Yale, I must acknowledge the contribution my high school, Robert College, made to my general education. I learned more there than anywhere else I have been. In the U.S., Fairleigh Dickinson University provided me with a scholarship which enabled me to study there. The Physics Department at F.D.U. in spite of its limited funds supported my undergraduate research and got me involved in this field. Financial support at Yale came from Becton and Adler Fellowships, and the National Science Foundation.

I thank my family for all they have endured in my absence. My brother, Yusuf, was instrumental in my coming to the U.S. to study. I thank my sister Virma for her support. Most special thanks go to my parents, who, in spite of their lack of any formal education, have encouraged me in my endless studies. I view this thesis in a sense as their accomplishment; a product of their unselfish support for my education.

I would like to dedicate this work to everyone who has over the years loved and supported me; to those who have taught me on science and thought, and on love and living. Thank you.

Table of Contents

List of Symbols

α	Normalized rf voltage, $\alpha = eV_\omega/\hbar\omega$
α'	Attenuation per unit length
B	Bandwidth
B_Q	Quasiparticle susceptance
β_g	Phase constant
Δ	Superconducting energy gap
DSB	Double side band
G_Q	Quasiparticle conductance
G_m	Mixer gain
γ	Relative attenuation in dB
Γ	Reflection coefficient
G_Q	The quantum conductance
G_{sg}	Subgap conductance
I_c	Junction critical current
IF	Intermediate frequency
I_J	Josephson current
I_{LO}	Magnitude of the LO current source
I_o	The dc current
I-V	Current (I) vs. Voltage (V)
J_c	Junction current density
J_n	n^{th} order Bessel function of the first kind
j_p	Pair response function
j_{qp}	Quasiparticle response function
λ_c	The waveguide cut-off wavelength
λ_g	Wavelength in the waveguide
λ_m	Wavelength in the microstripline
L_J	Josephson inductance
LO	Local oscillator
N(0)	Density of States at the Fermi level for a normal metal
ω_J	Josephson frequency
ω_m	The mixer frequency
P_{IF}	Intermediate frequency power
P_{in}	Input power
P_s	Power at the signal frequency

R_n	Normal state tunnel junction resistance
ρ	Reflection coefficient
ρ_m	Reflection coefficient at the mixer output
rf	Radio frequency
SIS	Superconductor-Insulator-Superconductor
σ	Attenuation factor
θ	Phase angle
θ_R	Constant phase offset
T_{if}	IF noise temperature
T_c	Superconducting transition temperature
T_m	Mixer noise temperature
T_R	Receiver noise temperature
V_g	The gap voltage
V_o	The dc bias voltage
VSWR	Voltage standing wave ratio
V_ω	Amplitude of the voltage at the frequency ω
Y_{emb}	Embedding admittance
Y_L	Load admittance
Y_o	Line admittance
YIG	Yttrium-Iron-Garnet
Y_{LO}	Admittance at the local oscillator frequency
Y_m	Admittance seen by the mixer at the frequency ω_m
Y_S	Signal admittance
Z_{IF}	Output impedance of the mixer
Z_L	Load impedance
Z_o	Waveguide impedance
Z_r	Radial stub impedance

List of Figures

List of Tables

I - Introduction

A theoretical understanding of the superconducting tunnel junction was achieved over two decades ago. Applications of the tunneling current include extremely sensitive magnetometers, high frequency oscillators, and detectors. This thesis examines mainly the quasiparticle tunneling currents in a superconducting tunnel junction. The Cooper pair currents are briefly discussed as possible tuning elements.

Quasiparticle tunneling currents flowing in a superconducting tunnel junction were discovered by Giaever in 1960. Subsequently it was discovered that the tunneling of electrons was enhanced by a radiation field in a quantized manner. This led to attempts at using this effect to detect electromagnetic radiation at high frequencies. Since then superconducting tunnel junctions have found extensive use as radiation detectors. The most sensitive detectors use the strong non-linearity in the quasiparticle tunneling current as a heterodyne mixing element. Such receivers based on the SIS (superconductor-insulator-superconductor) tunnel junction are now the dominant technology for astronomical receivers in the mm-wave band.

In spite of the rapid and impressive progress in this field, it still is more a field of research than one of development. This is due to the many materials issues, and the need of the radioastronomy and cosmology communities for detectors with quantum sensitivities which can only be achieved with very careful and application specific design. There are also some unanswered questions relating to the understanding of the tunnel junction. This thesis will try to address some of these.

The SIS receivers with the lowest noise and highest gain have often had mechanical tuning elements or a narrow bandwidth. This is a drawback for the development of focal plane arrays, where a large number of imaging elements would have to be tuned individually for every frequency. We have demonstrated a

good model for a single channel of a focal plane array receiver. The receiver employs a SIS mixer mount with a large instantaneous bandwidth around 100 GHz without mechanical tuning elements. This mixer performs comparably well as other SIS receivers.

Even though SIS mixers have employed quasiparticle tunneling currents, the currents were not observed until very recently. This recent work was very limited in its scope, i.e. it only looked at a limited bias range for a very small rf power level. We have, in this work, measured these tunneling currents for all bias voltages and for various rf power levels. This is the first observation of the singularity in the reactive quasiparticle current at the gap voltage. In this thesis I will examine how these currents scale with frequency and what the implications might be for mixers at high frequencies.

The reactive quasiparticle admittance of a superconducting tunnel junction is then successfully employed as the tuning element for a SIS mixer. This is the first demonstration of an electronic on-chip tuning element for a superconducting detector. We observe an increase in the dynamic resistance and an improvement in mixer gain and noise temperature as the dc bias voltage of the tuning junction array is varied.

Finally a new device concept is presented. The proposal is to use the voltage dependent quasiparticle admittance of the superconducting tunnel junction as a voltage controlled phase shifter. Three configurations are presented, which would provide voltage-variable on-chip phase shifting. The upper frequency limit of these elements may be as high as the gap frequency of the superconductor (0.7 THz for Nb). Such circuit elements could be utilized in superconducting systems in telecommunications, phased-array radar antennas, oscillators and in superconducting receivers.

II - Theory of SIS Tunneling and Heterodyne Detection

The work presented in this thesis relies on the tunneling characteristics of a superconducting tunnel junction. In this chapter the relevant theoretical conclusions of SIS tunneling related to heterodyne mixing are presented. This is a very brief summary of a rather complicated theory, and relates the significant results without trying to duplicate the rigorous mathematical derivations.

2.1 SIS Tunneling:

Excellent reviews exist for the tunneling properties of superconducting junctions [Tinkham, 1975; Bruynseraede, 1990; Barone, 1982; Van Duzer and Turner, 1981]. In a superconductor at zero temperature, all electrons exist in a ground state in pairs called Cooper pairs. Excitations from this ground state occupy single electronic states and are called quasiparticles [Bardeen, 1957]. A superconducting tunnel junction, also referred to as a superconductor-insulator-superconductor (SIS) junction consists of two superconducting electrodes separated by a thin insulating layer. The thickness of the insulator must be small enough to allow tunneling. In such a tunnel junction quasiparticles are of primary importance as they cause a sharp non-linearity in the dc I-V curve at the gap voltage. The full tunneling current in a superconducting junction has been theoretically studied by Werthamer (1966), Harris (1974,1975) and others.

At zero voltage the Josephson coupling between the two electrodes results in a finite dc current. This current is due to the flow of Cooper pairs and its magnitude depends on the phase difference across the barrier. The Josephson current is discussed further in Chapter 6. Most of this thesis work concerns the measurement and applications of the quasiparticle currents. Thus, the Josephson currents will be ignored. This is justified when the devices are biased far from

zero voltage and the junction capacitance is relatively large. Both of these conditions are met in our devices.

The quasiparticle dc current depends on the density of states in the two electrodes. This density is given by:

$$D(E)dE = N(0)\frac{E}{\left(E^2-\Delta^2\right)^{1/2}}dE \qquad |E| \geq \Delta$$

$$D(E)dE = 0 \qquad |E| < \Delta \qquad 2.1$$

where N(0) is the density of states for the metal at the Fermi energy [Bardeen, 1957]. To describe tunneling, these excitations can be thought of as hole-like excitations for k states below the Fermi wavevector and electron-like excitations for above the Fermi. An applied voltage shifts the Fermi level of one electrode with respect to the other. The tunneling current can then be calculated from the density of available states that the quasiparticles can tunnel into. The quasiparticle density of states at T=0 is shown in Fig. 2.1a for a tunnel junction with identical electrodes.

Fig. 2.2 shows the dc tunneling I-V curve for an ideal tunnel junction at T=0. The current at zero voltage is the Josephson current. In the quasiparticle branch of the I-V curve, there is no current flowing for voltages below the gap voltage since there are no available states for tunneling. The gap voltage measures the sum of the gap energies of the two superconducting electrodes:

$$V_{gap} = (\Delta_1 + \Delta_2)/e, \qquad 2.2$$

and for identical superconductors $V_{gap} = 2\Delta/e$. Since the gap energy depends on temperature, so does the gap voltage. At the gap voltage the singularities in the densities line up across the tunneling barrier, thus, there is a sharp onset of

tunneling current. The magnitude of this current rise is determined by the coupling between the electrodes, i.e. the barrier thickness.

In the presence of rf radiation, the tunnel junction I-V curve exhibits photon assisted tunneling steps [Tien and Gordon, 1963]. Figure 2.3 shows such steps for a given rf power for two different embedding circuits for the junction. Fig.2.1b is illustrative in understanding the origin of photon assisted tunneling. In this figure it is shown that a quasiparticle can absorb a photon and tunnel across resulting in a net dc current while the junction is biased below the gap voltage. The onset of this current for a single photon absorption process is at one photon energy below the gap voltage. This process is discussed in detail in Chapter 5.

2.2 Heterodyne Detection:

SIS heterodyne detectors have proven to be the most sensitive detectors for radioastronomy [for a review see Wengler, 1992; Blundell, 1992; Gundlach, 1989] in the frequency range extending from 100 GHz up to 700 GHz. Primary subjects of investigation in this field include interstellar molecular clouds, and star formation [Phillips and Keene, 1992]. The frequencies of interest are determined by the spectrum of molecular transitions, and limited by the absorption of the earth's atmosphere. Currently there is substantial effort to improve the existing SIS detectors and also to develop new detectors for the 700 - 1000 GHz frequency range. Since molecules are line sources, heterodyne detection is desirable, and yet a large bandwidth of tunability is necessary to observe at more than one frequency.

In a heterodyne detector a small amplitude signal is fed into a non-linear (mixing) element along with a large amplitude local oscillator signal (Fig.2.4). The output of the mixer at the difference (or intermediate) frequency carries

information about the phase and magnitude of the signal [Torrey and Whitmer, 1948]. The intermediate frequency is usually low enough to be amplified and detected using readily available technology. The mixer in a heterodyne system is usually the most critical element in determining the system noise. The figure of merit for a heterodyne detector is the receiver noise temperature given by:

$$T_r = T_m + \frac{T_{if}}{G_m}, \qquad 2.3$$

where T_m is the mixer noise temperature, T_{if} is the noise temperature of the if system, and G_m is the mixer gain defined as the ratio of the if output power of the mixer to the input signal power. The Dicke radiometer formula [Dicke, 1946] states that the integration time Δt necessary to obtain a given signal to noise ratio in a given bandwidth Δf is related to the receiver noise temperature by:

$$SNR = \frac{T_S}{T_R}\sqrt{\Delta t\, \Delta f}. \qquad 2.4$$

Thus a factor of two improvement in noise temperature can decrease the observation time by a factor of four.

The sharp non-linearity of SIS junctions makes them desirable as mixing elements. In the classical analog we assume that the dc I-V curve is modulated by the local oscillator signal (ω_{lo}), and this in turn mixes with the input signal (ω_s) due to the non-linear I-V characteristics. The amplitude modulated output has a component at the difference frequency, $\omega_{if} = \omega_{lo} - \omega_s$. This component can be detected and carries amplitude and phase information about the input signal. In a classical mixer both the input lo admittance and the output if admittance are usually close to dI/dV at the bias point. The double sideband gain in a classical

mixer is limited to one half, and the noise is the sum of all shot noise and other noise components [Torrey and Whitmer, 1948].

2.3 Quantum Theory of Mixing:

Introducing quantum effects results in a more accurate explanation [Tucker, 1979]. The response of the tunnel junction to a single frequency is complicated and will be discussed in detail in Chapter 5. For understanding of basic mixer concepts, the existence of photon assisted tunneling steps is sufficient. The shape of these steps depend on the embedding admittance of the device as shown in Figure 2.3. For certain embedding admittances the tunneling steps can be flat or even have negative slopes [McGrath, 1981; Smith, 1981; Kerr, 1981]. The slope in the center of a step is defined as $1/R_D$ where R_D is the dynamic resistance. The simplified circuit models for the dc bias, signal input and if output are shown in Figure 2.5.

When the junction is biased in the middle of a photon step and a test signal is applied along with the local oscillator signal, mixing between the two signals occurs. This produces a voltage at the input port of the if amplifier. If the intermediate frequency is much lower than the signal frequency, then the output admittance of the mixer at the if port is equal to the dynamic resistance (R_D) at the bias voltage, V_o. The dynamic resistance as shown in Fig. 2.3 can be infinite or negative for certain range of embedding admittances. In this circuit model the SIS mixer acts as a constant current source and the available output power is $(I_{if})^2R_D/8$ [McGrath, 1981]. Thus the *available* output power scales with the dynamic resistance and the gain is much larger than unity when the dynamic resistance is very large or negative. The measured gain however depends on the impedance mismatch between the mixers if output and the amplifiers input. For example a SIS mixer with a very large or negative dynamic resistance will have a

large available gain, but the measured gain will be small if the if amplifier input impedance is 50Ω. Gain larger than one has been observed in some SIS mixers [for example: Winkler, 1991a; Kerr 1981; McGrath, 1981], however there are practical limits as to how high the gain can be. One limitation is due to saturation which occurs when the if output voltage swing approaches a small fraction of the width of one photon step [Feldman, 1987a].

It should be pointed out that the main difference between the classical analog and the full quantum theory is the admittance of the device. In the classical analog the device conductance is equal to the first derivative of the dc I-V curve. In the quantum theory the device conductance is more complicated, and in addition there is a voltage dependent susceptance. This susceptance has been established to be necessary to observe gain larger than unity in these devices [Mears, 1991b].

A matrix formalism is used to correlate the response of the SIS tunnel junction at different relevant frequencies. This multiport heterodyne mixer model includes ports for the local oscillator, the signal, the intermediate frequency, and their harmonics. The conversion properties are determined from the dc I-V characteristics of the SIS tunnel junction, and the embedding admittance. A small signal admittance matrix relates the voltages and currents at all frequencies involved:

$$i_m = \sum_{m'} Y_{mm'} \cdot v_{m'}, \qquad 2.5$$

where m is a number denoting the frequency ω_m in consideration:

$$\omega_m = m\omega + \omega_o, \qquad 2.6$$

where ω is the local oscillator frequency and ω_0 is the output (or intermediate) frequency. In this formalism m=1 corresponds to the input signal port and m=0 to the if output port; for example Y_{01} is the ratio of the if output current to the signal input voltage. In a classical mixer the elements of this admittance matrix are inferred from the dc I-V curve and its first derivative which gives the conductance. Tucker formulated these matrix elements for a quantum mixer, where the conductance is quantized and there is a finite quantum susceptance [Tucker, 1979; Tucker and Feldman 1985]. This explains the interaction of the junction with the local oscillator, the signal and their higher harmonics. Considering all harmonics requires knowledge of the admittances relating currents and voltages at all frequencies. This results in a very lengthy calculation as the admittance matrix becomes large.

One common case is when the intermediate frequency is small and a three port approximation can be used. In this case, two situations pertain: 1) the local oscillator and the signal are close enough in frequency such that the junction admittance is the same for both, and the detector is in the double side band (DSB) mode, 2) the junction is not in the quantum regime at the if frequency. Then the if port admittance is the dynamic resistance at the bias voltage and the admittance of the junction at the lo frequency is all that is needed for calculating mixing parameters.

Here I will quote some important results of such a calculation. Let us define some dimensionless parameters used to characterize the mixer:

$$L_o \equiv \frac{2G_{10}}{G_{01}} \qquad \eta \equiv \frac{G_{01}G_{10}}{G_{00}G_{11}}$$
$$g_S \equiv \frac{G_S}{2G_{11}} \qquad g_L \equiv \frac{G_L}{G_{00}} \qquad 2.7$$

In these equations the subscripts S and L refer to the source (local oscillator) and load (if) respectively. The conversion gain of the mixer is then given by:

$$L^{-1} = L_o^{-1} \frac{\eta G_S}{(1+g_S)^2} \frac{4g_L}{(g_L + g_L^{\circ})^2} \qquad 2.8$$

where

$$g_L^{\circ} \equiv 1 - \frac{\eta}{1+g_S}. \qquad 2.9$$

The expression for the gain diverges for $g_L^{\circ} < 0$. Thus, infinite gain can be obtained in a SIS mixer for certain embedding admittances which in turn determine the G (or Y) matrix elements above.

The shot noise current of the SIS mixer is usually the main source of noise. This is given by the H-matrix elements relating input/output currents. An interesting result of the quantum theory of mixer noise is that the shot noise is not directly related to the magnitude of the photon assisted dc current. A possibly more obvious result is that the subgap leakage current is the main contribution to the shot noise. There is a minimum achievable noise temperature in a double sideband heterodyne mixer approximately equal to $\hbar\omega / k_B$ (7K at 100 GHz). Another source of noise is the thermal fluctuations in the dissipative terminations at various ports. The noise in the SIS mixers reported in this thesis and also in most other mixers operating away from the quantum limit is believed to be mostly due to the shot noise. This proves the importance of high quality tunnel junctions in obtaining low noise. Noise in this context is discussed in detail by various authors [Feldman, 1987a; Wengler and Woody, 1986; Caves, 1982]. The effect of the embedding circuitry on receiver performance is mostly on the mixer gain.

Recently, due to an increase in computational capabilities 5-port and 8-port calculations have been carried out as well [Kerr, 1993; Tong, 1990]. The implication of that calculation for this thesis is that for most of the devices reported here the three port approximation may introduce large uncertainties. This is because the $\omega R_n C$ products of our devices ranged from 0.9 to 4. For devices with an $\omega R_n C$ product of one, the three port approximation can underestimate the mixer noise by a factor of two [Kerr, 1993].

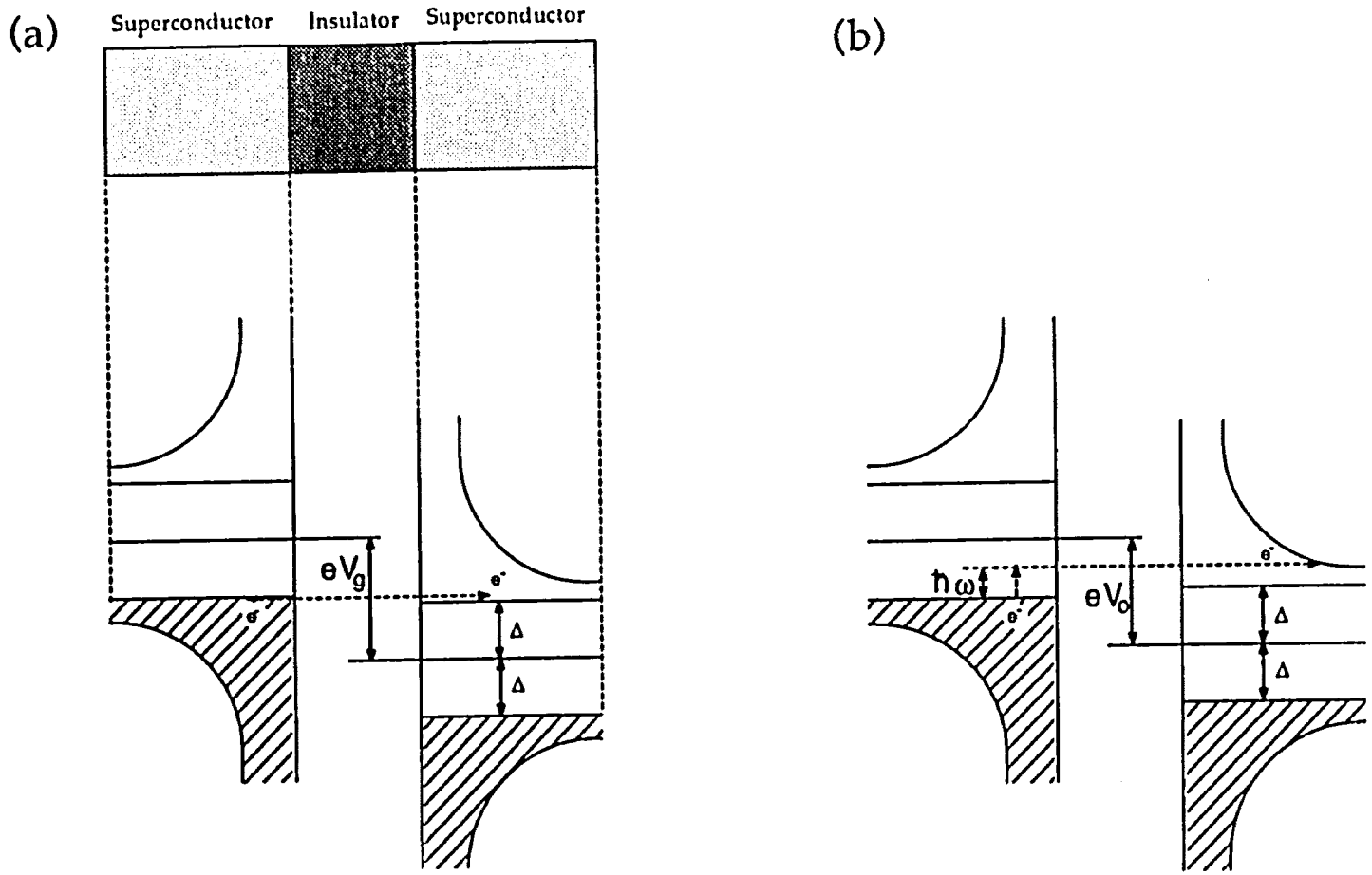

Figure 2.1: The semiconductor representation of the quasiparticle density of states for a tunnel junction with two superconducting electrodes of the same material. a) The junction is biased at the gap voltage which is $\geq 2\Delta$. A quasiparticle can tunnel across at this voltage as the singularities are lined up in energy. Thus the quasiparticle tunnels across to an available state, creating a hole like excitation in the left electrode. b) The junction is biased below the gap voltage. A quasiparticle absorbs a photon and tunnels across resulting in a net current.

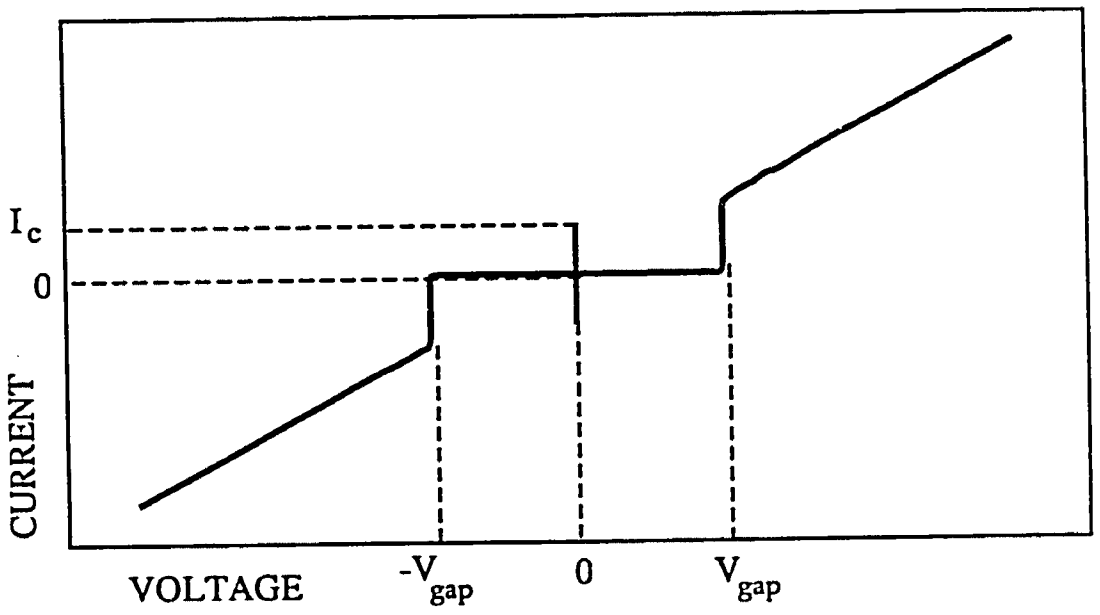

Figure 2.2: The dc I-V curve for an ideal SIS tunnel junction. The zero voltage current I_c is the Josephson current due to the flow of Cooper pairs. The rest of the curve is called the quasiparticle branch. No quasiparticles flow at voltages below the gap voltage as there are no states to tunnel into. Above the gap, the resistance approaches the normal state resistance, R_n.

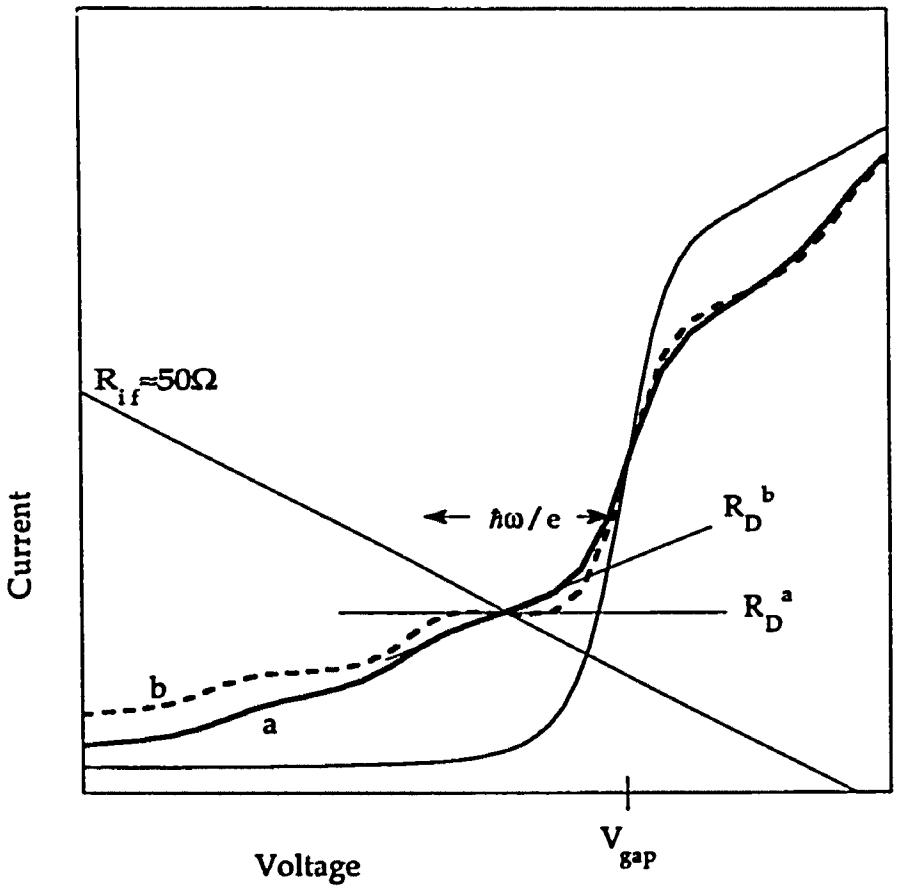

Figure 2.3: Theoretical photon assisted tunneling curves for a $Nb/AlO_x/Nb$ tunnel junction at 90 GHz for two embedding admittances. Curve a is for an inductive embedding admittance of Y_{emb}=1-j0.5. Curve b is for a capacitive embedding admittance of Y_{emb}=1+j1. These admittances are normalized to the normal state conductance, R_n^{-1}.

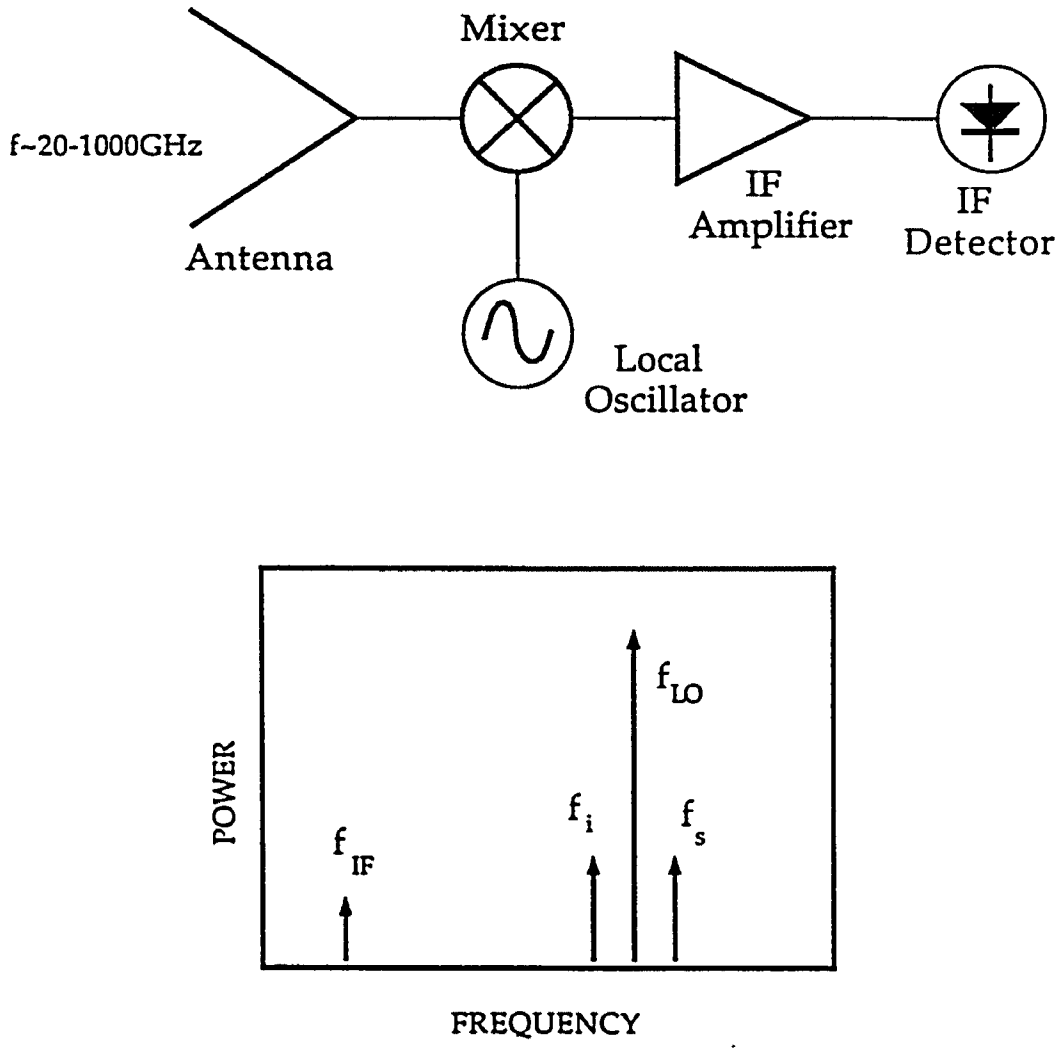

Figure 2.4: Schematic diagram of a heterodyne detector for radioastronomy. The coupling into the mixer can be quasioptical or waveguide based. The power spectrum to first order includes the local oscillator , the signal, the intermediate frequency, and the image frequency. A double side band (DSB) receiver responds evenly to the image and the signal.

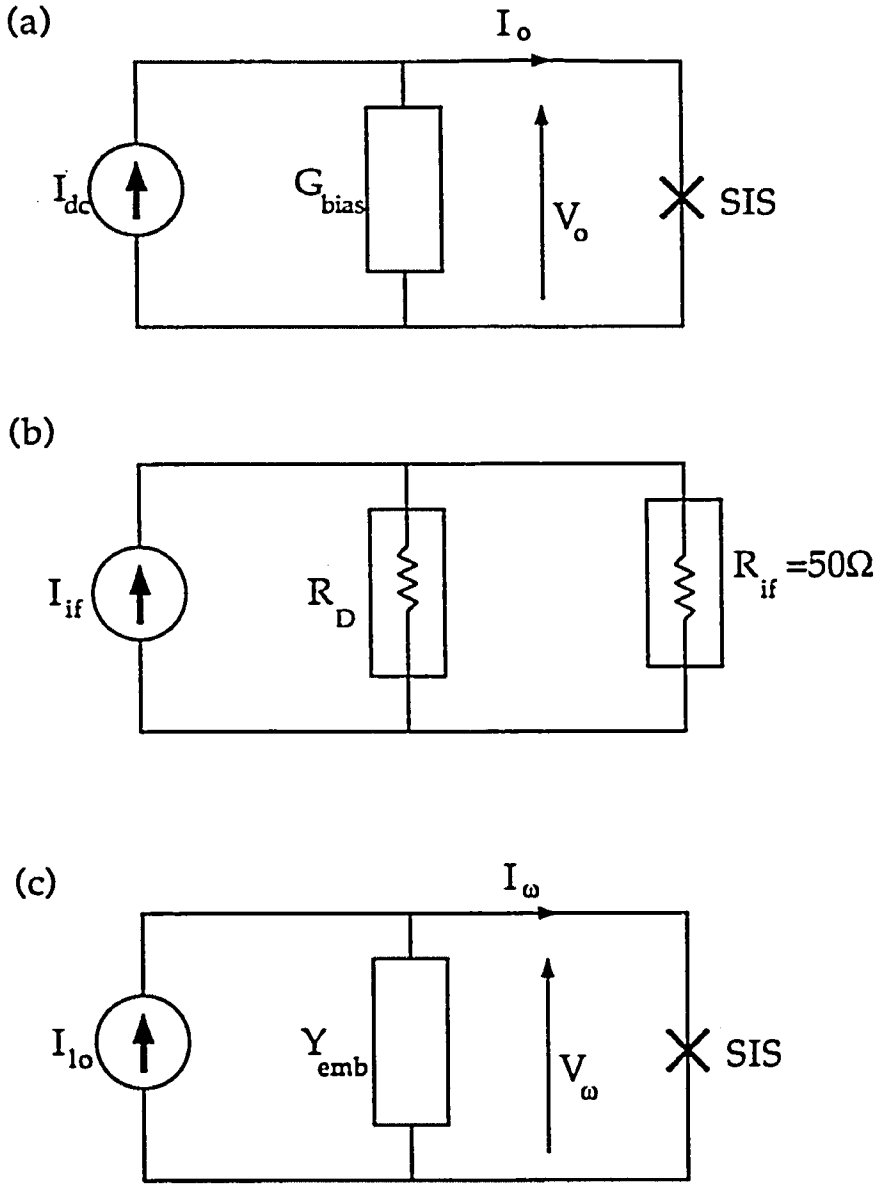

Figure 2.5: Simplified circuit models representing bias conditions for the mixer at various frequencies (ports). a) The dc bias circuit. The load line is determined by the load resistor in the control circuitry and can be varied. b) The if output circuit. For a small if, R_D is the dynamic resistance of the junction at the bias point. The if output of the junction is represented as a current source. c) The rf equivalent circuit. Y_{emb} includes the local oscillator output admittance and the junction capacitance.

III - Yale Mixer Design

The goal of our receiver work is to demonstrate the applicability of SIS mixers for focal plane array receivers in radioastronomy. The requirements for such a system are that:

a) each channel has about the same rf input and if output impedance,

b) no mechanical tuning elements are needed,

c) individual elements are robust.

3.1 Design Considerations:

For this goal a single channel SIS receiver is constructed. A waveguide coupling scheme is chosen since waveguide structures, in general, can be easily and accurately reproduced. The alternative approach is a quasioptical coupling scheme, which in the past suffered from poor coupling efficiency [Xizhi, 1985]. More recent advances in quasioptical systems however have overcome this shortcoming [Zmuidzinas and LeDuc, 1992].

The if output resistance of the mixer is the differential resistance of the dc I-V curve in the middle of the first photon step, for a small if as discussed in Chapter 2. This resistance can be rather large or even negative for a well rf-matched device. To obtain large gain in such a case one must use an if transformer to transform this output impedance to the 50 Ω input impedance of a typical if amplifier [Zmuidzinas and LeDuc, 1992]. Since if transformers limit the operational bandwidth of a receiver, and introduce possible problems of non-reproducibility, we do not use one. The tunnel junction has to directly drive the 50 Ω input impedance of the if amplifier at 1.5 GHz. Simultaneously the rf impedance of the mixer needs to be matched to the source impedance of 346 Ω at

mid-band. In the final design this impedance is transformed to 50 Ω, and the SIS tunnel junctions are also designed to have a normal state resistance of 50 Ω.

The ωR_nC product, where R_n is the normal state resistance of the tunnel junction, is a very important quantity in determining various junction properties. The Q factor and the bandwidth of the quasiparticle mixer is a function of the ωR_nC product. It also determines the effect of the capacitance for a given embedding circuit. For an SIS tunnel junction the Q factor is given by;

$$Q= \omega R_{rf}C, \qquad 3.1$$

where R_{rf} is the resistance of the junction at the signal frequency.

One would want a low Q circuit for easier rf coupling; for Q<1 one does not need a tuning inductor to resonate the capacitance. A small Q for a given rf resistance means a smaller capacitance. Since tunnel junctions are highly non-linear, they can respond to and also generate higher harmonics of the input signal. These harmonics can produce noise components within the bandwidth of the device and saturate the if output or add output noise [D'Addario, 1988]. A finite capacitance is desirable to shunt these higher frequency currents. From experimental evidence at 100GHz, $\omega R_nC \approx 3$-4 is believed to be a good compromise, when the capacitance is resonated [Tucker and Feldman, 1985].

There have been attempts to calculate how the ωR_nC product should scale with frequency for optimum operation. One needs to consider the junction resistance at the signal frequency and at its harmonics. The ratio of these two resistances is approximately constant as a function of frequency. Kerr and Pan (1990) empirically derive at a scaling function using this approximation for a constant Q factor. Blundell and Winkler (1991) use a piecewise approximation to the dc I-V curve and assume $R_{rf}=2R_n$, which is accurate for a frequency equal to half the gap frequency.

The resulting scaling functions are given by:

$$\omega R_n C = \frac{400}{f(GHz)} \qquad \text{(Kerr and Pan)}$$

$$\omega R_n C = \frac{(2+\gamma)}{4\gamma} \qquad \text{(Blundell and Winkler)} \qquad 3.2$$

where γ is the normalized signal frequency ($\gamma = f/f_g$, f_g~700 GHz for Nb).

My calculations use a real I-V curve for a typical power level ($\alpha = 1$) used in mixing experiments. The bias voltage is fixed in the middle of the first photon step where most mixing experiments are performed. The results of these calculations are shown in Fig. 3.1. All figures are normalized such that $\omega R_n C = 4$ at 100 GHz. We see that there is not a large difference between the calculations in spite of the different approaches. The practical implication is that $\omega R_n C$ should approximately scale as 1/f. Note that all these calculations ignore two very important effects: the quasiparticle susceptance and the Josephson currents. These effects are discussed later in this thesis.

The capacitance of a tunnel junction depends on the barrier thickness, d, and on the area, A as: $C = \varepsilon_r \varepsilon_o A/d$, where ε_r is the dielectric constant of the insulator. The normal state resistance, R_n depends on the area and the critical current density, $J_c(d)$; $R_n \sim 1/[J_c(d)\, A]$. J_c is approximately an exponentially decreasing function of the barrier thickness [Kleinsasser, 1993]. This dependence on barrier thickness is much stronger than that of the capacitance (linear vs. exponential). Thus the R_nC product is nearly independent of the junction area and depends on the current density as:

$$R_n C \propto \frac{1}{J_c} \qquad 3.3$$

Since the calculations above indicate that for optimum rf matching to a constant impedance source ωR_nC should scale as $1/\omega$, the current density J_c must increase approximately as ω^2.

Another factor determined by the ωR_nC product is the relative strength of the reactance of the device. As we will see in Chapter 5, the magnitude of the quasiparticle reactance is proportional to the normal state resistance. Thus for a given R_nC, the effect of the reactance is smaller for a large capacitance device. This reactance can have a substantial effect on mixer performance. This further complicates the choice of the ωR_nC product necessary to obtain good performance with SIS mixers. This is because most of the previous experiments and calculations involved junctions with large ωR_nC products (>4), in which case the capacitive admittance or the external tuning inductive admittance dominates. Recently devices with lower ωR_nC products (<4) have been tested and modeled. In our work and that at Berkeley the calculations have shown that at 100 GHz for devices in the quantum regime mixing parameters cannot be accurately determined if the quasiparticle susceptance is ignored [Mears, 1991a; Mears, 1991b]. Figure 3.2 shows the quasiparticle susceptance as a function of frequency along with the conductance for a junction biased in the middle of the first photon step. Note that there is a sharp decrease in the susceptance at high frequencies. This implies that the effect of the susceptance in mixing experiments becomes less important as the frequency is increased.

3.2 Mixer Block and Chip Layout:

Figure 3.3 shows the waveguide mount and the circuit setup used in scale modeling measurements. Figures 3.4 shows the microstrip circuit and an equivalent electrical model, while Fig. 3.5 has the detail of the chip area. The transformation of the waveguide impedance from the mid-band value of 346 Ω to

50Ω is done by a 4-step Chebychev transformer circuit (Fig. 3.3). In theory this should produce a 1.05:1 VSWR (Voltage standing wave ratio) over the waveguide band. VSWR is a measure of the coupling efficiency such that a VSWR of 6:1 corresponds to a reflection loss of 3dB. Scale modeling results are close to this value. The physical realization of the circuit consists of a single ridge in the E-plane canter of a WR-284 waveguide (WR-10 in the actual mixer mount), with four $\lambda_g/4$ long steps each of different height, where the height determines the impedance of each section. Stray capacitances and inductances are ignored in the design.

Aside from the impedance transformation, the ridge also transforms the TE_{10} waveguide mode to a quasi-TEM microstrip mode. The mode of propagation in the last step of the ridge is a TEM mode, but the E-field lines close to the edges are bent. This is close to the quasi-TEM mode that propagates in a microstrip. The 50Ω output of this final step then makes contact to the 50Ω input microstripline (point A), with a length of $\lambda_m/4$ ($\lambda_m \approx \lambda_o/3$, λ_o is the free space value). This quarterwave length of stripline serves the same purpose as in anti-reflection coatings in optical systems, i.e. reflections interfere destructively to minimize standing waves. The tunnel junction is placed between this input microstrip and a radial stub (point B).

Radial stubs provide rf-grounds at their apex when the dimensions are properly chosen [Vinding,1967; Syrett,1980; Atwater, 1983]. In general the radius determines the center frequency while the angle sets the effective bandwidth. They have about three times the bandwidth of quarterwave transformers, and are less sensitive to variations in dimensions. Thus the rf-voltage is developed across the tunnel junction. The if signal generated by the junction is extracted via the high impedance line connected to the apex of the radial stub. This line is also used to dc-bias the tunnel junction. The dc and if ground is thus provided by the

waveguide which is connected to the ground plane of the microstrip and the dewar. At the if frequency the length of the microstripline circuitry is less than $\lambda_m/20$, with a lumped capacitance of about 0.5 pF to the ground plane. The if and dc biasing lines are subsequently separated via a bias tee consisting of a wirewound inductor and a capacitor. The two radial stubs at E and F following the 90° stub provide additional isolation of the rf signal and increase the effective bandwidth of the rf-ground.

3.3 Devices:

The Nb/Al-O_x/Nb trilayer tunnel junctions used in this work were fabricated at the Westinghouse Science and Technology Center by A.H. Worsham [Worsham,1991a]. Typical device characteristics are listed in Table 3.1. The fabricated device areas were as small as 0.5 μm^2, with expected current densities up to 5000 A/cm^2, and V_m-values of 40mV (at 2 mV and 4.4K). The device area is estimated from visual inspection, and the capacitance is calculated using this area and a specific capacitance of 45 fF/μm^2. The inferred $\omega R_n C$ product for these devices ranges from 1 to about 3. The $\omega R_n C$ product does not seem to scale with J_c as expected from Eq.3.3. This could be due to errors in estimating J_c, the junction area, or the specific capacitance. A modified SNIP technique is developed to produce such small junctions. Fifteen different configurations in a total of 102 mixer chips are fabricated on 25.4 mm x 25.4 mm x 50 μm fused and crystal quartz wafers. Fused quartz is used as the substrate due to its low loss and low dielectric constant ($\epsilon_r = 3.8$). A substrate thickness of 50 μm is chosen as the maximum thickness at which radiation losses and substrate modes do not have a major effect. Single SIS junctions as well as 2 and 4 junction arrays with individual junction areas of 0.5 μm^2 up to 4 μm^2 are included in the designs.

Table 3.1: Parameters of devices tested as mixers in this work. The quoted J_c values are determined from measurements of large area junctions. The capacitances are calculated from the expected device area using a specific capacitance of 45fF/μm^2.

Device	Junction Area $(\mu m)^2$	Number of Junctions	J_c (A/cm^2) (expected)	$R_n(\Omega)$ (measured)	$\omega R_n C$ (100GHz, estimated)
A	0.5	1	5000	71	1
B	0.5	2	3000	431	3
C	0.5	2	3000	125	0.9
E	0.5	4	3000	619	2.2
I	4	4	3000	124	3.5

3.4 Integrated Tuner:

The initial testing is done with no tuning elements, and also with an integrated inductor to resonate the geometric capacitance of the junction. Tunnel junctions with $\omega R_n C$ products less than unity have a large bandwidth such that a tuning inductor is not necessary. Devices with larger $\omega R_n C$ products, however, require an inductive tuning element to resonate the capacitance at the frequency of operation. Mechanical tuning elements in the form of waveguide backshorts have been used successfully by others to tune out the capacitance, but are cumbersome and not practical for array applications. Some designs have utilized integrated inductors in the form of open or short circuited transmission lines; these are easy to implement. For example an open-circuited transmission line

has an input impedance that is purely reactive. However since this reactance is a very strong function of the electrical length of the stub, the bandwidth of such a configuration is relatively small. Such a tuning scheme restricts the operational bandwidth to about one third of the bandwidth which can be obtained with a real inductor. This bandwidth is given by $\omega R_{rf} C$.

Ideally one would like to place a non-dissipative inductor in rf-parallel with the tunnel junction, without shorting the currents flowing at dc and if frequencies. We have used a second radial stub to provide a dc and if-isolated rf ground for the tuning inductor. The tuning inductor consists of a thin wire between the input microstripline and the lower radial stub. The location of the rf-ground provided by the upper radial stub is very close to the rf-ground of the lower stub. There is also substantial capacitive coupling between the two radial stubs through the 2μm wide gap between them. This capacitance is shown by the dashed line in Fig. 3.4. The tuning inductor, at the rf frequency, is in parallel with the tunnel junction.

The magnetic inductance of such a wire is given by [Terman, 1943]:

$$L(nH) = 0.2\ l\left\{\ln(l/[w+t]) + 1.19 + 0.2235[w+t]/l\right\} \qquad 3.4$$

where w is the width, l the length, and t the thickness of the wire in mm. This wire is 2 μm wide and about 0.2 μm thick. Since both of these dimensions are larger than the superconducting penetration depth in niobium (~0.07 μm for thin film) [Javadi,1992], the kinetic inductance of the electrons is ignored.

In the original design the effects of the two 90° bends in the wire and the capacitive coupling between them is neglected. Subsequent computer modeling shows up to a twenty percent reduction in the inductive susceptance of the wire due to capacitive coupling between the closest segment. In other words,

substantial amount of the rf-signal can be shunted through the first section into the radial stub. This effect is less in devices with longer wires (with a larger junction capacitance to resonate). The reason for having the wires separated by only 2μm is to have the rf-grounds provided by the two radial stubs close together. Careful CAD modeling[1] however shows that this can be accomplished without sacrificing on tunability. Unfortunately the second iteration devices have not been fabricated.

The chip designs included devices with multiple shorting bars across the two wires. These ladder-like structure would enable one to vary the inductance by eliminating branches via microlithography. Since the $\omega R_n C$ products of our devices are in general rather small, and receiver results satisfactory, these devices have not been used.

3.5 Scale Model :

We have scale modeled our SIS mixer design discussed above at a much lower frequency (2.5 - 4 GHz). The main advantage of scaled measurements at lower frequencies is that the mixer mount and circuitry are usually much easier to fabricate and thus several approaches can be evaluated before the design is finalized. Also, even though microwave CAD programs are quite accurate [1], they still have some shortcomings in estimating stray field effects, especially with waveguide to microstrip transitions, and discontinuities. Finally, vector network analyzers are more readily available at lower frequencies.

An HP8410 Network Vector Analyzer [2] is used for impedance measurements. With a Reflection-Transmission test unit, phasor information on all 2-port parameters could be obtained. Elements of the design such as the ridge and radial stubs are first tested individually and then final measurements of the mixer mount were made. In the final measurements we use Stycast 3.75 [3] as the

microstrip substrate, since it is more readily available and machinable than quartz. The microstrip lines and circuits were cut out of 75 μm thick adhesive copper tape [4].

The proper radius and angle of the radial stub are determined from the measurements of the scattering parameter S11. A number of measurements are performed on 90° and 180° radial stubs with radii from 7.3 mm to 10.5 mm. The 180° stubs provide slightly more broadband terminations as expected. The termination impedance at the center frequency which depends on the radius, changes little with the different radii. The optimum radius is $r_0 \sim 9 - 9.5$ mm (350μm). The numbers in parentheses following scale model results indicate the corresponding properties for the real mixer. Stray radiation from the substrate becomes very significant in the upper part of the band for substrates thicker than 3.2 mm (100μm).

The dc /if probe line slightly degrades the performance of the rf ground termination. To minimize this effect we use two radial stubs along the microstrip at positions that are determined empirically. These radial stubs have the same radius as the first rf ground termination stubs. The first (90° radial stub) has its major effect in the middle and upper part of the band, while the second one (45° radial stub) affects the lower part of the band. This is due to the locations of these stubs relative to the first stub. The rf ground termination provided by the first radial stub is such that no changes in S11 are observed for various load terminations on the end of the dc/if line.

The ridged waveguide Chebychev transformer is designed from formulas given by Hoefer (1982) and 4 sections are used to transform the waveguide impedance down to 50 Ω at the last ridge with a theoretical VSWR of 1.08:1 between 2.64 - 3.87 GHz (75 - 110 GHz). In the scale model this 4.6 mm (6.4 mils) wide transformer is mounted in a WR284 (WR-10) waveguide.

To test the performance of the scale model the return loss is measured with a 50 Ω chip resistor between the λ/4 long 50 Ω microstrip-line and the center of the top radial stub ground termination. A 1 pF chip capacitor is added in parallel to observe the rf matching to an untuned SIS element (Fig. 3.3). This is the equivalent capacitance of a 0.8 μm^2 SIS junction in the actual mixer design. Finally, a 75 μm diameter and about 5 mm long copper wire is used as an inductor between the input microstripline and the lower radial stub in order to tune out the capacitance. The measured reflection coefficient is shown in Fig. 3.7 for an untuned element (R || C) and an inductor tuned element (R || C || L).

The embedding impedance seen by the SIS element is inferred from the reflection measurements on the single ridge Chebychev transformer and on the microstrip-line circuit. This is done by modeling both the waveguide transformer and the radial stub as single port elements characterized by S11 measurements done on the scale model. The measured S11 parameters are used as input parameters, and the resulting circuit is modeled using TouchStone. Table 3.2 summarizes the scale modeling results on the microstrip circuit and the total mixer mount.

Table 3.2: The VSWR values and the embedding impedance at 90GHz derived from S11 parameter measurements of the microstripline circuit and the full mixer mount. (3 dB return loss corresponds to a VSWR of about 6:1.)

Configuration	**Microstripline**	**Total mount**	**Zemb(90GHz)**
50Ω	1.33:1	1.38:1	50-i10
50Ω//1pF	3:1	4:1	25-i35
50Ω//1pF//L	1.8:1	3:1	55+i15

[1] Touchstone, EEsof, Westlake Village, CA.

[2] Hewlett Packard, Palo Alto CA.

[3] Stycast 375, Emerson & Cuming Inc. Canton MA.

[4] Electrical tape No. 1245, 3-M Co., St. Paul, Minnesota.

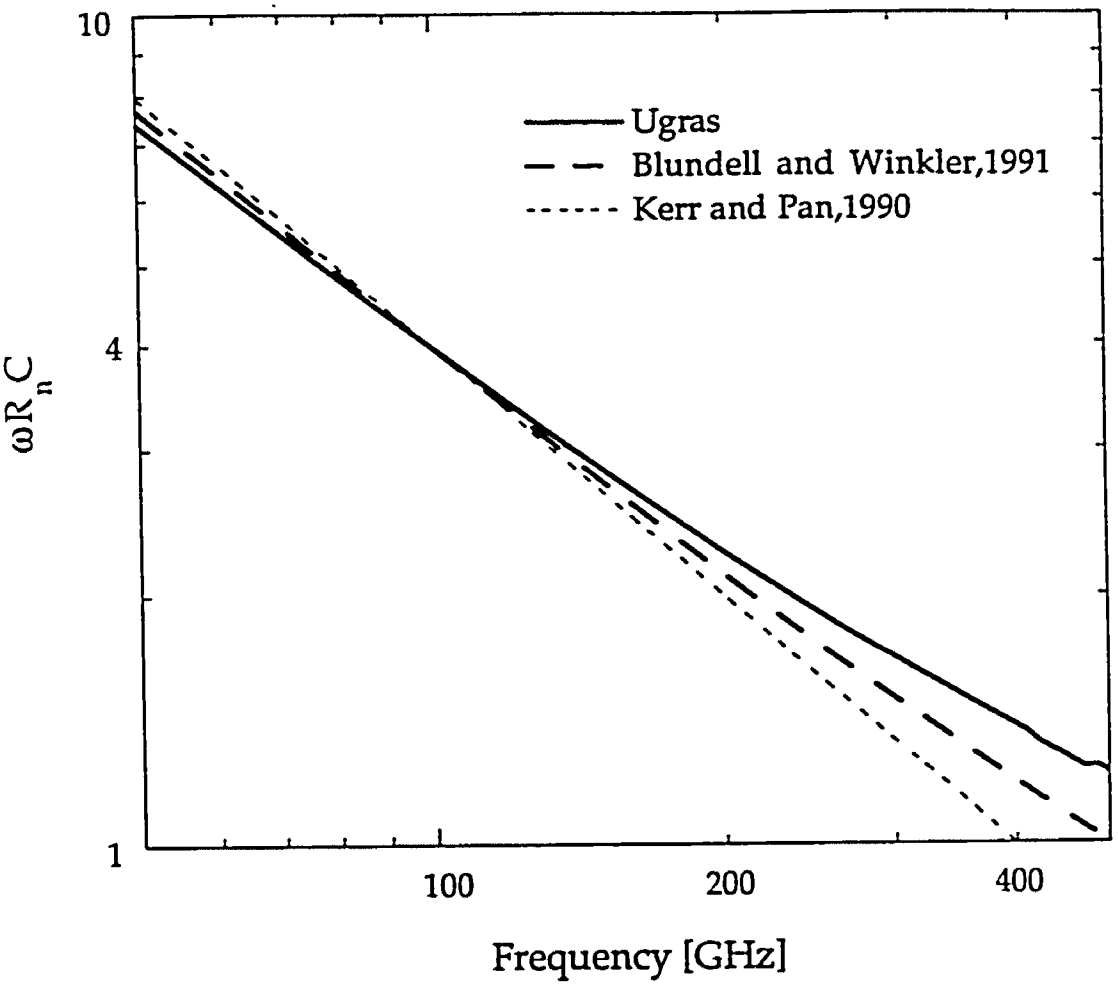

Figure 3.1: Results of three different calculations on the optimum scaling of the $\omega R_n C$ product as a function of frequency for fixed if impedance. The curves have been normalized to $\omega R_n C=4$ at 100 GHz from experimental data at that frequency.

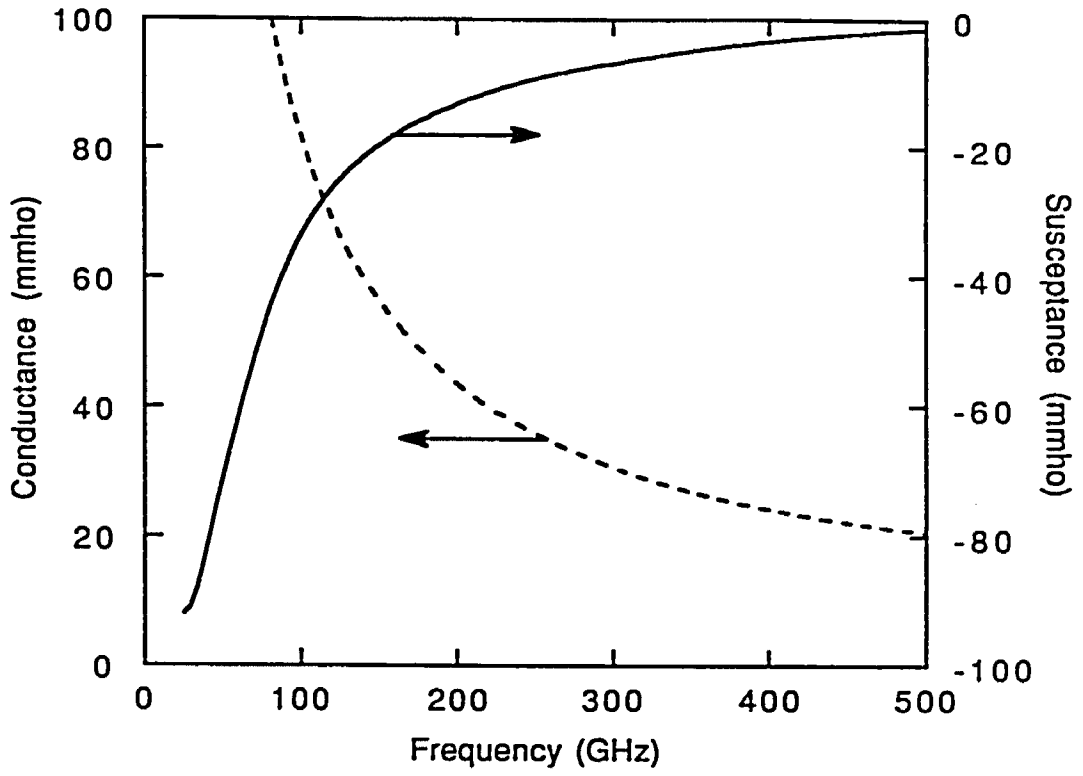

Figure 3.2: The quasiparticle susceptance and conductance as a function of frequency for a 50Ω device biased in the middle of the first photon step calculated for α=1. These are the experimental conditions for most mixers. Both quantities scale inversely with the normal state resistance, and are independent of the capacitance.

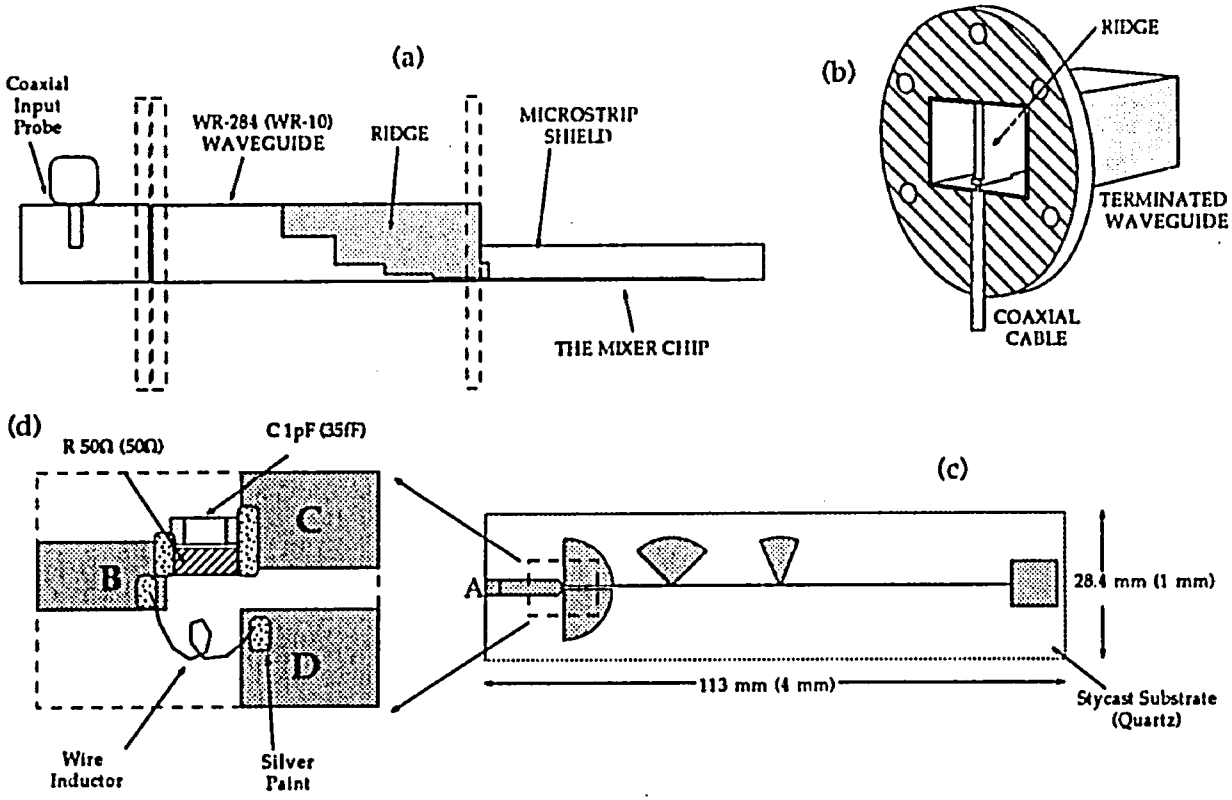

Figure 3.3: The mixer design as implemented in the scale model. Parameters corresponding to the actual mixer are shown in parentheses. a) Test setup for S11 measurements on the signal/lo input port. The single ridge Chebychev impedance transformer made electrical contact to the microstrip circuit at point A. b) Measurement setup for testing the ridge transformer. This S11 data was used in determining the embedding impedance. c) The chip layout. The metallized areas were Cu in the scale model. d) Detail of the chip. The chip capacitor and resistor and the wire inductor were attached using silver paint.

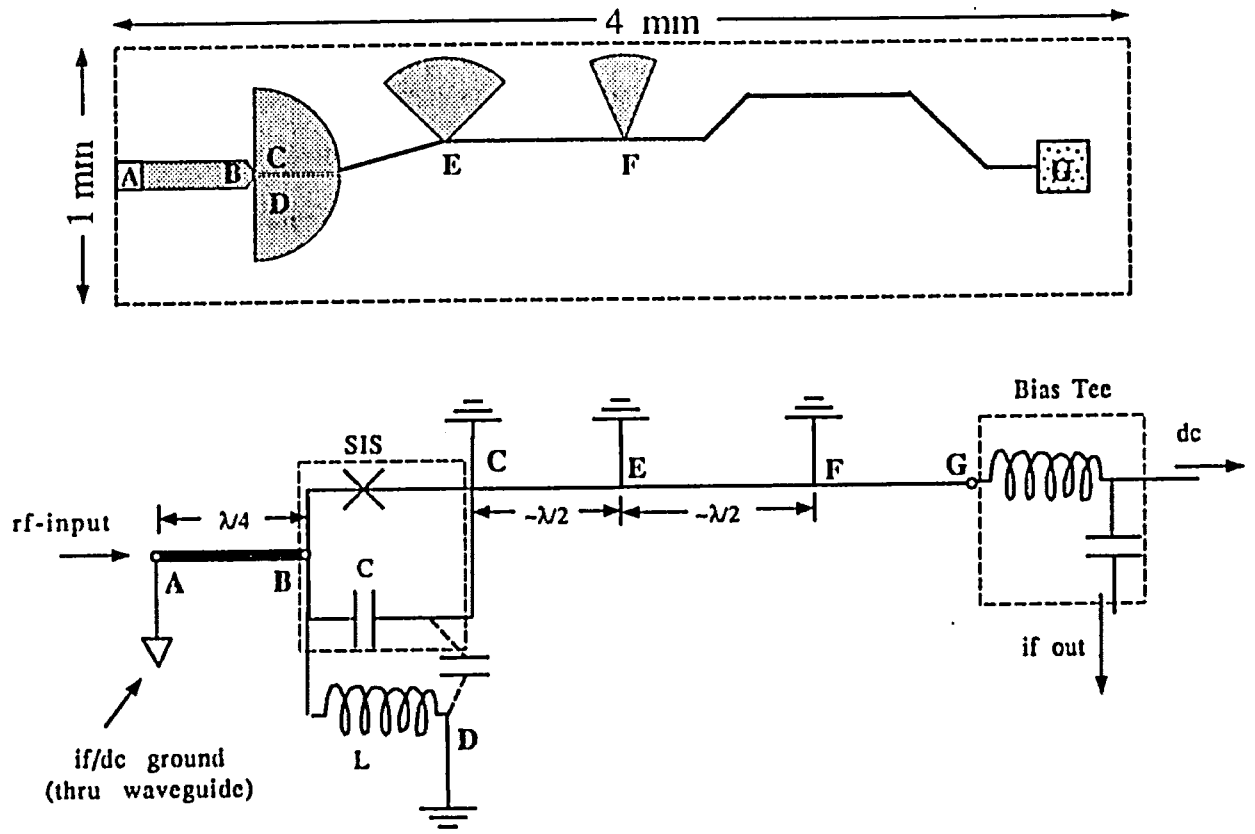

Figure 3.4: Layout of the actual mixer chip and a simplified electrical model showing dc, if, and rf grounds. The capacitive coupling between the upper and lower radial stubs is shown by the dashed line. Points E and F are rf short circuits with different frequency characteristics. When impedance transformed to point C, they reduce the effect of the high impedance if/dc line and preserve the bandwidth. The dc and if signals were isolated using a bias tee which made contact to point G with an indium pad.

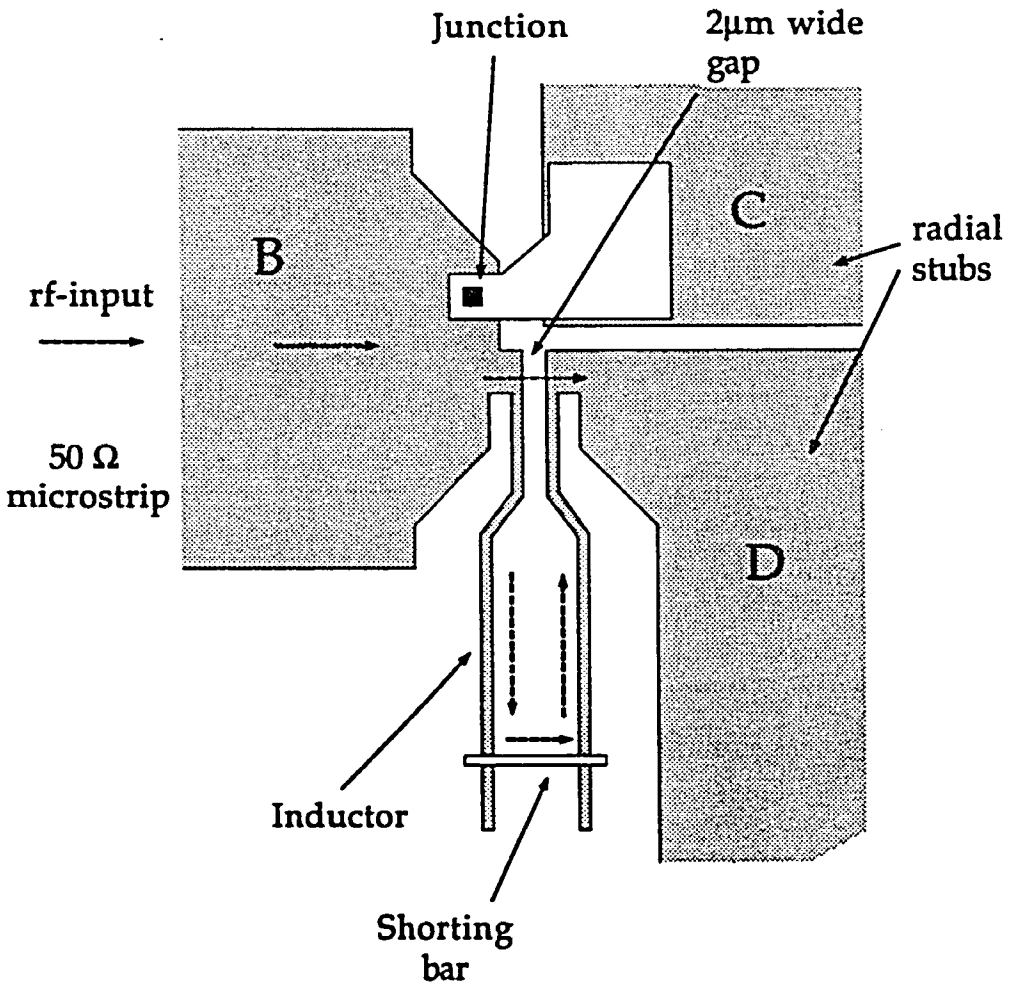

Figure 3.5 Detail of the junction area. This is a single junction tuned by a thin film inductor. Dashed lines show the path of the rf signal. Some of the signal is coupled through the 2μm gap which results in less inductive tuning. The gap between the stubs was kept to 2μm to increase the coupling.

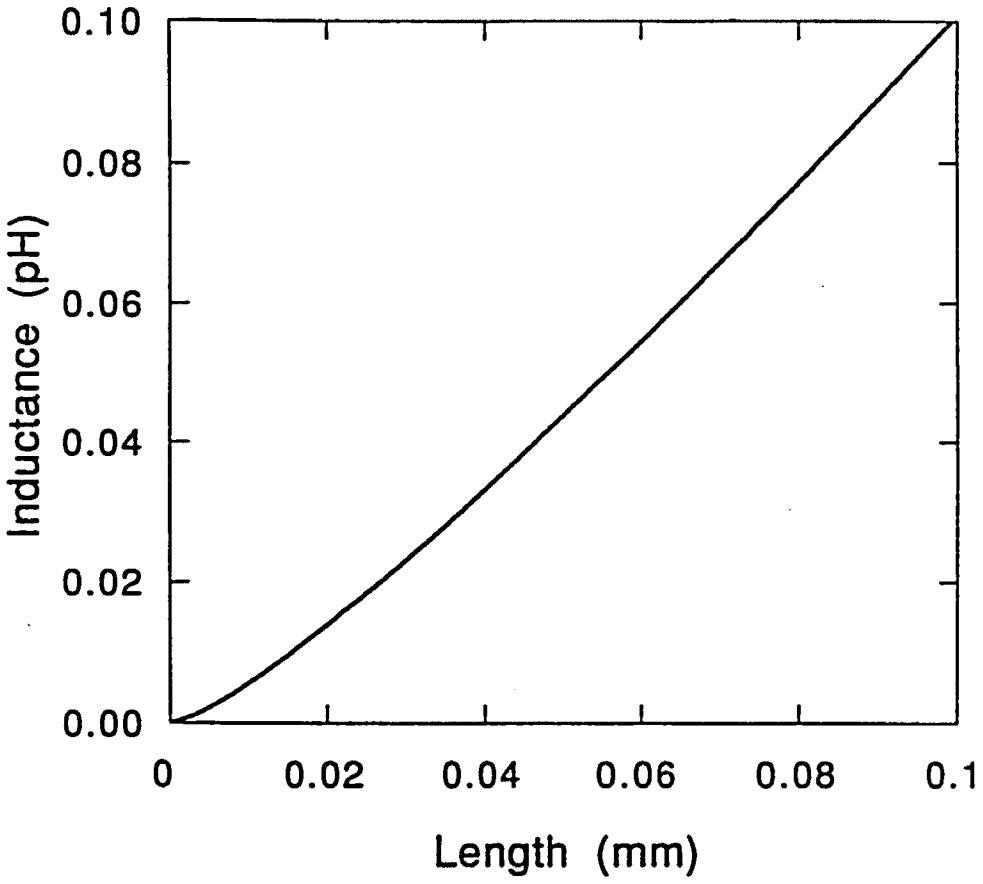

Figure 3.6 Inductance of a 2μm wide thin film wire calculated from Eq. 3.4 . The inductance necessary to resonate the capacitance of a $1\mu m^2$ junction is 0.05 pH.

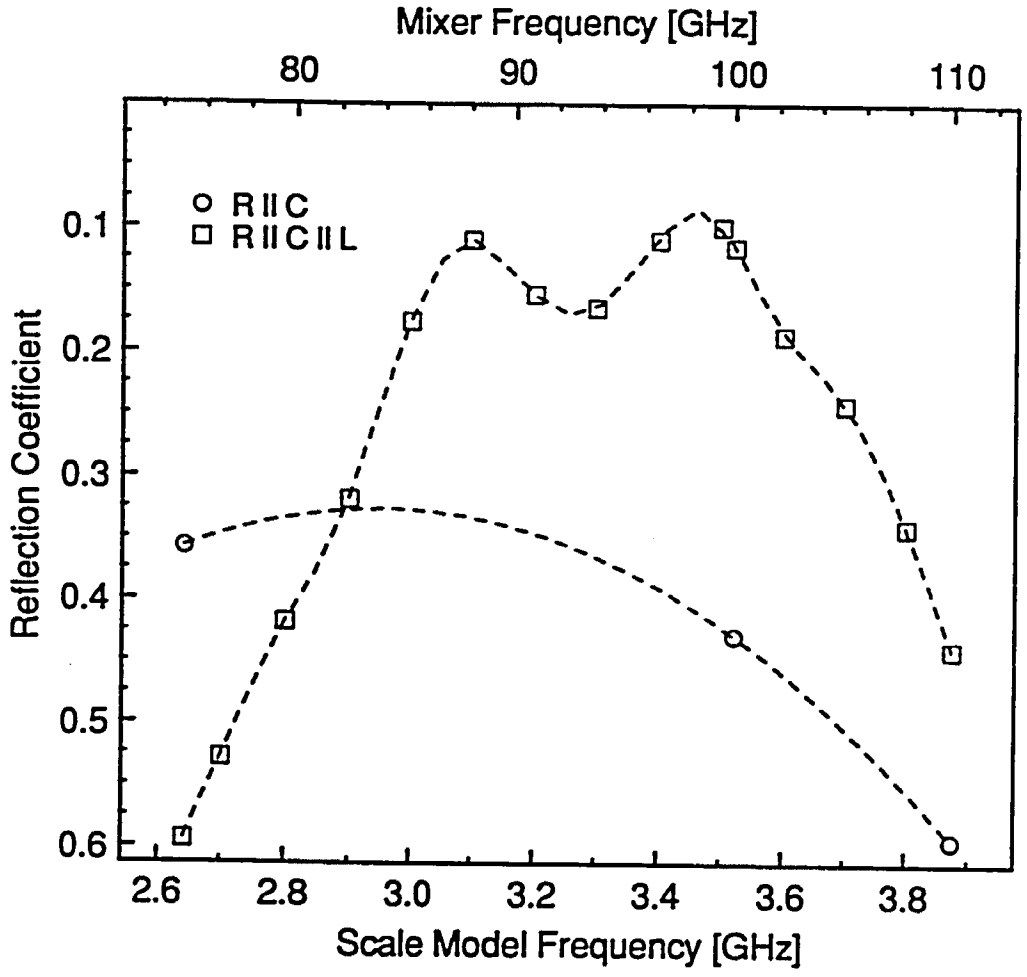

Figure 3.7 Reflection coefficient from scale model measurements. Not that the inductance substantially improves the rf coupling. The upper x scale shows the corresponding mixer frequency.

IV - Receiver Design and Results

The receiver system (see Fig. 4.1) is built to determine the receiver and the mixer (T_r and T_m) noise temperatures, the coupled and available gain of the mixer (G_m and G_a), and the if system noise temperature. This is a similar receiver configuration to ones used previously at NRAO. The distinguishing features are:

a) a variable temperature cryogenic rf hot/cold load which can be brought in and out of the waveguide using electromagnets,

b) a 50Ω coaxial cryogenic if hot/cold load,

c) a cryogenic coaxial switch.

4.1 The RF System:

The rf test signal source in most receivers is provided by a 77K/300K blackbody source outside the dewar, which is coupled into the dewar through a vacuum window. The window losses then need to be considered in the mixer calculations, which causes substantial uncertainty [Pan,1989]. Even though this is an easier approach, we chose to construct a cryogenic variable temperature load for obtaining more accurate measurements [Winkler,1993; McGrath,1985].

The internal *rf* hot/cold load consists of a cold waveguide termination and a heated silicon vane that can be moved in and out through a slot in the waveguide (Fig. 4.2). The part of the vane that is inserted into the waveguide is etched down to 14μm from an initial thickness of 10 mils. An 80 nm thick NiCr resistive layer is deposited on one side of the vane to provide uniform heating and a better match to the waveguide impedance. The heating is provided by a 100Ω carbon resistor heat sunk to the Si vane, while the temperature is read out by a diode thermometer. The heat distribution on this membrane is uniform

enough such that there are no non-linearities in the if output of the mixer for large temperature variations of the vane (Fig. 3.3). If the temperature of the vane were non-uniform, this would not have been the case. The vane can be heated up to ~100 K while in the He dewar.

One advantage of this approach is that the vane can be flipped in and out of the waveguide with two electromagnets. Then the hot vane and the cold termination can alternatively be presented to the mixer. This enables fast and reliable optimization of the receiver noise temperature. A circuit is designed and constructed to drive the vane in and out of the waveguide. With this circuit, one can switch the position of the vane using a SPDT switch, or with an external oscillator, the vane can alternate between the two positions continuously. Both of these processes are found to be reliable and reproducible. During the use of this dewar the vane is switched >5,000 times with no effects on the reproducibility of the data. The highest frequency at which the vane can oscillate is about 20 Hz. This limit is due to the inductance of the electromagnets and also due to the inertia of the vane. To reduce the error due to rf-mismatches, the vane is used as both the hot and the cold source while taking the reported data.

The lo source is a YIG-tuned oscillator [1] which is tripled to 77.5 - 120 GHz with a multiplier circuit [2]. A YIG-tuned oscillator consists of a Yttrium-Iron-Garnet cavity which changes its resonant frequency with the application of a dc current to an electromagnet. This source is chosen for its tunability, even though it is not very temperature stable. The combination with the tripler suffered from various resonances in the output power spectrum. In the mixer measurements, most of these issues are not problematic, as the FM noise is negligible, and the temperature is kept rather stable. In some array measurements the lo power is not sufficient for frequencies above 110 GHz.

The lo signal was brought into the cryogenic dewar through a thin Mylar[3] membrane between two waveguide flanges. After a gold plated stainless steel waveguide section, it is coupled to the mixer input waveguide through a cross coupler with 23dB attenuation. The hot/cold load signal from the Si vane is on the non-attenuating arm of the coupler. For molecular line measurements the vane could be taken out and replaced by a waveguide horn and a feedthrough to a room temperature line source or antenna. The dewar is set up for such a modification.

4.2 The IF System:

The if signal generated across the tunnel junction is extracted from the mixer chip at point G in Fig 3.4 via an indium pad. This makes contact to a bias tee circuit (Fig. 4.4). The bias tee is a filter designed to separate the if signal from the dc signal. Both the dc and the if ground consist of the mixer mount and the ground plane. The bias tee is constructed on a 10 mil Duroid [4] substrate (ε=2.1) using adhesive Cu tape [5]. A 62 pF chip capacitor and a wire inductor are soldered on the substrate. For the if signal, the low-impedance path is provided by the capacitor, while the dc signal travels through the wire inductor. The if impedance of this capacitor is less than 2 ohms.

After the bias tee, the IF signal enters a latching single pole six throw coaxial switch, which mechanically switches to one of six output ports via electromagnets [6]. This switch is modified at NRAO by placing a 10kΩ dc-shunting resistor at each port to reduce electromagnetic transients in switching. Such transients can generate a large voltage pulse across the tunnel junction and damage the device. The input port of the switch is connected to the if output of the mixer block. Of the six output ports only four are used; 1) a 50Ω termination

at 4.2 K, 2) a variable temperature 50Ω if hot/cold load (Fig. 4.5), 3) a short circuit, 4) output to a circulator.

The two 50Ω terminations are used to determine the noise temperature of the if chain, in a similar manner as the rf hot/cold load. The short circuit is used to determine the gain of the if chain. In the receiver mode, the if signal is directed to the circulator. The circulator serves multiple functions. The most important one is to isolate the tunnel junction if output port from the if amplifier input port. This is necessary since the if amplifier generates a substantial amount of noise at its input port, enough to saturate the tunnel junction. By using an attenuator at the third port of the circulator, the reflected noise power is reduced by >15dB. This is a shortcoming of SIS mixers since circulators are the primary limiting factor in the if bandwidth. With a larger if bandwidth one can observe a much larger spectral range simultaneously. The center frequency of this circulator is at 1.4 GHz with a bandwidth of < 0.3 GHz.

A secondary function of the circulator is to measure the IF mismatch of the mixer. For this purpose a test signal is bounced back from the mixer and detected at the if amplifier output. This output is then compared to the reflection off the short circuit. The ratio of the two reflection coefficients is the mismatch of the mixer to the if amplifier. The *measured* mixer gain is divided by this factor to obtain the *available* mixer gain.

The gain of the if chain is determined by measuring the reflection of a test signal from the short circuit. This is limited to the bandwidth of the circulator. The directional coupler allows one to measure the gain and stability of the if amplifier over a large bandwidth. This is a straight forward transmission measurement. The two-stage FET if amplifier is provided by the Univ. of Mass. The noise, bandwidth, and gain spectrum depends strongly on the bias conditions of the FETs. Depending on the mixer configuration, the biasing needs

to be varied slightly to avoid saturation of the mixer from the excess noise at the input of the if amplifier. Typical numbers are; 26 dB for gain at 1.4 GHz, a bandwidth of >0.6 GHz, and a noise temperature of 10 - 15 K. The if signal is further amplified by 67dB with a room temperature two-stage GaAs amplifier [7].

Most measurements are taken using a variable if bandpass filter with a bandwidth of about 70 MHz [8]. This is necessary to avoid saturation effects on the amplifier and detector. The source for if test measurements is a tunable sweeper [9]. The signal is detected with a diode detector for most measurements. The vector analyzer is used for some measurements done on the if chain to obtain phase information.

The cryogenic He dewar is an Infrared Labs dewar with a 10 inch diameter 4 inch deep workplate, modified for pumped He operation [10]. The three if coaxial lines going to room temperature electronics, are heat sunk both at the nitrogen and helium bath. Between room temperature and nitrogen, a stainless steel coaxial cable is used, and between the nitrogen and helium baths, the signal travels through a specially constructed stainless steel coaxial section with no insulator. The 64 "dc"wires are all heat sunk to the He bath with Stycast KT [11] and a pc-board. At the nitrogen stage all wires are heat sunk to individual grooves in a metal piece using Ge varnish. Finally all wires go through separate EMI filters to a control box [12].

4.3 Control Circuitry :

Both the coaxial if switch and the rf hot/cold load vane are driven using similar solenoids to simplify the driving circuitry design. Both switches are latching types, and this requires a current pulse rather than a constant current. This is done to reduce the resistive heating, and increase the hold time of the dewar. The coaxial switch consists of 12 solenoids. Each one of the 6 positions

on this switch has a pair of set/reset solenoids. At 4.2 K a 100 mA current pulse for ~100 msec is necessary to set or to reset any switch. Due to the latching process it is critical that all switches are reset before setting another one. A two pole twelve throw mechanical switch is used to control the solenoids (Fig. 4.6). The voltage necessary for switching is ~28 volts. In order to interface the switches with the computer, two supplies are used ; a 34 volt supply for the high voltage switching, and a 6 volt battery to bias the CMOS logic chips. One pole of the mechanical switch is connected to the input of a 555 timer to provide a clock pulse to control the duration of the switching current. The second pole is used to set or reset the corresponding switch. The NOR gates are used to reset both neighbours of the reset position on the rotary switch (so that one can switch clockwise and counterclockwise). The diodes are necessary to short the back emf of the switching solenoids, which would otherwise burn the transistor.

The control circuitry for the rf hot/cold load solenoids is slightly more complicated since it can be controlled not only by a digital signal, but also by an analog input. This is required for rapid switching of the solenoid such that the if output can be observed on a lock-in amplifier or on an oscilloscope. Thus a comparator is used at the input.

All these switches were controlled by an HP computer during most of the experiments. In order to control 14 switches (6 set for coax, 6 reset for coax, 2 for vane), a 4-to-16 line decoder (CD4514B) is used. A 4 bit word from the computer is fed into a HP3421a Data Acquisition unit [11] with an array of FET switches. The output is then fed into the decoder which controls the driving circuitry in parallel with the mechanical switch.

The dc-biasing circuit for the tunnel junction is designed to stable biasing with a variable load line, and also provide optional feedback and sweeping functions (Fig. 4.7). AD2702 provides a stable bipolar voltage. The reference

input of the AD524 is used to offset the external sweep range. PMI1012 is used in the feedback circuit for stable biasing when in the internal mode. The external mode is used when acquiring data with the computer. The external sweep input can be an oscillator as well as a computer controlled voltage source. The load resistor (R_L) for the bias is also used as the current sensing resistor. The output of the voltage and current sensing amps can be connected to computer interfaced DVMs, an X-Y recorder, or an oscilloscope.

The sweeper circuit shown in Fig. 4.8 is designed to provide single sweeps, as well as continuous sweeps with a variable frequency. The digital switching circuitry is designed such that one can switch between any two modes continuously without creating a voltage pulse or an error. One op amp is used for feedback and another one for integration. The oscillation is controlled by mainly a flip-flop and FET switches. Thus the upper circuit is the basic oscillator, while the lower circuit provides for the various functions.

4.4 Hot/Cold Load Measurements:

The receiver gain and noise temperature were determined using the Si vane as a variable rf signal source. The power spectral density of a black body radiator (or source) is given by Plank's formula:

$$\frac{P}{B} = \frac{\hbar\omega}{\exp(\hbar\omega/k_B T) - 1} \qquad 4.1$$

where B is the bandwidth of detection, T is the physical temperature, and ω is the center frequency. This function is plotted in Figure 4.9 for a 100 GHz source or detector. From this figure we see that above 4 K, one can approximate the full

Plank radiation law with a linear function given by the Rayleigh-Jeans law. This simplified formula is:

$$P = k_B T B \qquad 4.2$$

This approximation can be used to describe the radiation from a blackbody source and also the power spectrum of a noise source characterized by a noise temperature. This expression ignores zero point fluctuations, but is accurate within a degree for physical temperatures down to 2.5 K at 100 GHz.

Even though radioastronomy applications of SIS mixers require molecular line observations at a given signal frequency, the mixer itself can be accurately evaluated using a blackbody source. Since the blackbody radiation spectrum is very broad, coupling with finite bandwidth should eliminate higher harmonics of the frequency of interest. Otherwise the receiver will respond to those frequencies as well and the measurement will yield an apparently higher gain. Waveguide structures filter out of band signals well enough, such that harmonic response is usually not a major problem.

To determine the receiver noise temperature, the if output power is monitored as a function of the Si vane temperature. The if output power is given by:

$$P_{if-out} = G_{if} G_m (P_S + P_r) \cong G_{if} G_m k_B (T_S + T_r) \qquad 4.3$$

where G_{if} and G_m are the gain for the if system and the mixer, P_S is the input signal power from a load at temperature T_S, and T_r is the equivalent noise temperature of the receiver. Thus, the if output power should be a linear function of the hot/cold load temperature (Fig. 4.2). From the slope of this curve

vs. T_S one can determine the receiver gain, $G_{if}G_m$ and from the x-intercept the receiver noise temperature, T_r.

In order to separate the contributions in gain and noise of the if-system, a similar measurement was done for the if system. For this purpose the coaxial switch was switched to the if hot/cold load setting. Then the temperature of the if hot/cold load was varied between about 5 and 50 K and the output power was measured. This power is given by:

$$P_{if-out} = G_{if}(P_S + P_{if}) \cong G_{if}k_B(T_S + T_{if}) \qquad 4.4$$

where T_{if} denotes the noise temperature of the if system . Here $\hbar\omega << k_B T_{if}$, so the Rayleigh-Jeans formula is essentially exact.

Again the slope determines the gain of the if chain beyond the if-switch, and the x-intercept the noise temperature of the if system (Fig. 4.5). The if noise is mainly due to the cooled amplifier, since it is the first stage of amplification. Figure 4.10 shows the measured output power as a function of the hot/cold load temperature for the if system. Also shown is the dependence of the noise temperature on the if frequency. The frequency is scanned using a high Q filter at room temperature. The noise temperature is pretty constant as a function of frequency from 1.15 to 1.45 GHz. The usable if window for the mixer is smaller due to the circulator.

Figure 4.3 shows a typical measured output power as a function of the hot/cold load temperature for the receiver. Note that the curve is very linear. This shows that the rf vane is radiating in proportion to the measured physical temperature as expected. This is the method used to get accurate receiver data. For fast optimization, the vane is kept at a constant temperature and moved in and out of the waveguide. The difference in the if output is then maximized.

This method of evaluating receiver parameters is called the Y-factor method, which refers to the ratio of power outputs for two input temperatures. In the case of a black body radiator or load at two temperatures, T_c and T_h ($T_c < T_h$);

$$Y = \frac{P_{if}^{h}}{P_{if}^{c}} = \frac{T_r + T_h}{T_r + T_c}. \qquad 4.5$$

Since the thermometry, the power meter, and the control circuitry for both hot /cold loads are interfaced to the computer, the Y-factor measurements and optimization could be done with ease. For the set of measurements reported in this chapter, there are two variables to optimize in mixing experiments; the bias voltage, and the lo power.

4.5 Receiver Results:

Device B:

As seen in chapter 2, the shape of the rf-induced tunneling steps depends strongly on the embedding circuitry which affects receiver performance. Figure 4.11 shows four pumped I-V curves for Device B, each for a different frequency. At 100 GHz, the dynamic resistance on the first photon step is negative. This implies good rf-matching at this frequency. This is expected since this is an inductor tuned device. At lower and higher frequencies the dynamic resistance becomes positive, but the step remains relatively flat. The if output power is shown as a function of dc bias voltage for two load temperatures. We see that the largest Y-factor is obtained in the middle of the first photon step. Receiver data for this device and others tested is listed in Table I and plotted in Figures 4.12 and 4.13.

A unique feature of this device is the large non-uniformity in the areas of the two junctions in series. The structure in the I-V curve above the current rise at the gap voltage is due to the proximity effect [Ruggiero, 1986]. From the proximity effect steps in this array we estimate that there is approximately a 30% difference in the areas of the two devices. The pumped I-V curves, however do not show structure below the gap and the receiver shows good performance. Calculations have shown that up to a 40% difference in area should not cause a substantial decrease in receiver performance [Feldman], and our results agree.

Device E:

This is an untuned device with a large normal state resistance of 619 Ω and a capacitance of 5 fF. Due to the large mismatch to the rf source resistance, this device did not show good receiver performance in spite of its low capacitance.

Device A:

This is also an untuned device with a small capacitance. However since the resistance is much better matched to the source resistance of 50Ω, it shows the best performance at 80 GHz. The increase in noise at midband is unexplained. It may be due to series resonances present in the mixer mount.

Device C:

This device showed mixer gain over the whole waveguide band. This is an impressive result considering that there are no mechanical tuning elements. A low $\omega R_n C$ product of 0.9, and a reasonably well matched normal state resistance are the reasons for the good receiver performance of this device.

Device I:

This is also an inductor tuned device, but with a much higher $\omega R_n C$ product (3.5). The resistance is matched well, and the mixer noise is lower than in device C, probably because of the larger capacitance which shunts higher harmonics better. The fact that the mixer gain is lower suggests a loss

mechanism in the tuning inductor or degradation of performance due to non-uniform array properties.

4.6 Discussion and comparison with theory:

Our receiver results have implications as to the effectiveness of the design approach discussed in the previous chapter. The devices have shown good performance across the band with integrated or no tuning elements. A ωR_nC product of ≈ 4 seems to result in lower *mixer* noise when devices C and I are compared. For large mixer gain , a small ωR_nC product is better, and also results in a larger bandwidth (compare C vs I). Thus the choice of the ωR_nC product is still dominated by the specific system requirements. Achieving a small receiver noise temperature with a noisy if amplifier requires a large mixer gain. This in turn means a small ωR_nC product (<2) for the mixer. If one has access to a very low noise and stable if system with enough bandwidth, a ωR_nC product of ~ 4 is a good choice for the mixer when integrated tuning elements are used. Our if system suffers from insufficient isolation of the if noise from the mixer, and a large if noise temperature. Thus the mixer gain plays a big role in determining the receiver performance.

A way of determining the effectiveness of the rf coupling scheme in a SIS mixer is to compare the embedding admittance calculated from the pumped I-V curves with the expected embedding admittance. In our case the design embedding admittance is inferred from scale model measurements and is shown in Fig. 4.14. The embedding admittances calculated from the pumped I-V curves are also shown for devices I and E. This calculation is done using the voltage match method [Skalare,1989]. Briefly, this method calculates the rf-induced current at various bias voltages and determines an embedding admittance from those values. The three port equivalent circuit model is shown in Fig. 2.2. The

higher harmonics are assumed to be shorted by the junction capacitance in the three frequency approximation. We see that even though there is agreement around the center frequency, the calculated embedding admittances show more dispersion. This can be due to machining tolerances on the waveguide ridge, or the field distribution around the junction (this is obviously difficult to study with a scale model). Still, as shown in Fig. 4.15 the magnitude of the reflection coefficient has a similar shape for the scale model and the calculated embedding circuit.

The receiver performance is also compared with theory. This is again in the three frequency approximation where we assume that harmonics are shorted. There is a distinct disagreement between theory and experiment in the mixer gain, most probably due using this three frequency approximation (Fig. 4.16). Recent calculations have shown that for $\omega R_n C$ products less than four, one needs to use the five-port model, where the first harmonic effects are included [Kerr,1993; Tong,1990]. The disagreement in mixer noise may also be attributed to additional tunneling currents, which are not included in theory (Fig. 4.17). Since the quantum theory of mixing assumes that all currents (electrons) are modulated by the rf field, shot noise contributions from inelastic tunneling is not included. All devices tested show a proximity effect at the gap-rise. The effects of this structure on mixing properties is not known [Hu,1990b]. Another source of error in noise is the if amplifier input noise coupled into the junction through the circulator. Even though this noise is attenuated by the circulator by ~16 dB, it still has a contribution due to the finite effective bandwidth of the circulator. This reflected noise effect can be quantified by using a calibrated noise source at the directional coupler port.

[1] Model AVD-26240/W , Avantek Corp., Santa Clara, CA.

[2] Model MU-10 tripler, Millitech Corp., South Deerfield MA.

[3] Dupont Inc., Newark,Delaware.

[4] Rogers Corp., Chandler, AZ.

[5] Electrical tape No. 1245, 3-M Co., St. Paul, Minnesota.

[6] Model M6-413C901S, Dynatech Inc., Calabasas, CA.

[7] Model 16179, Omni Spectra Inc., Merrimack, NH.

[8] Texcan Inc. Indianapolis, IN

[9] Model HP8350b with 83525b RF plug-in, Hewlett Packard, Palo Alto CA.

[10] Model HD-10, Infrared Laboratories Inc., Tuscon, AZ.

[11] Emerson & Cuming Inc. Canton MA.

[12] Erie Inc., Trenton, Ontario, Canada.

[13] Hewlett Packard, Palo Alto CA.

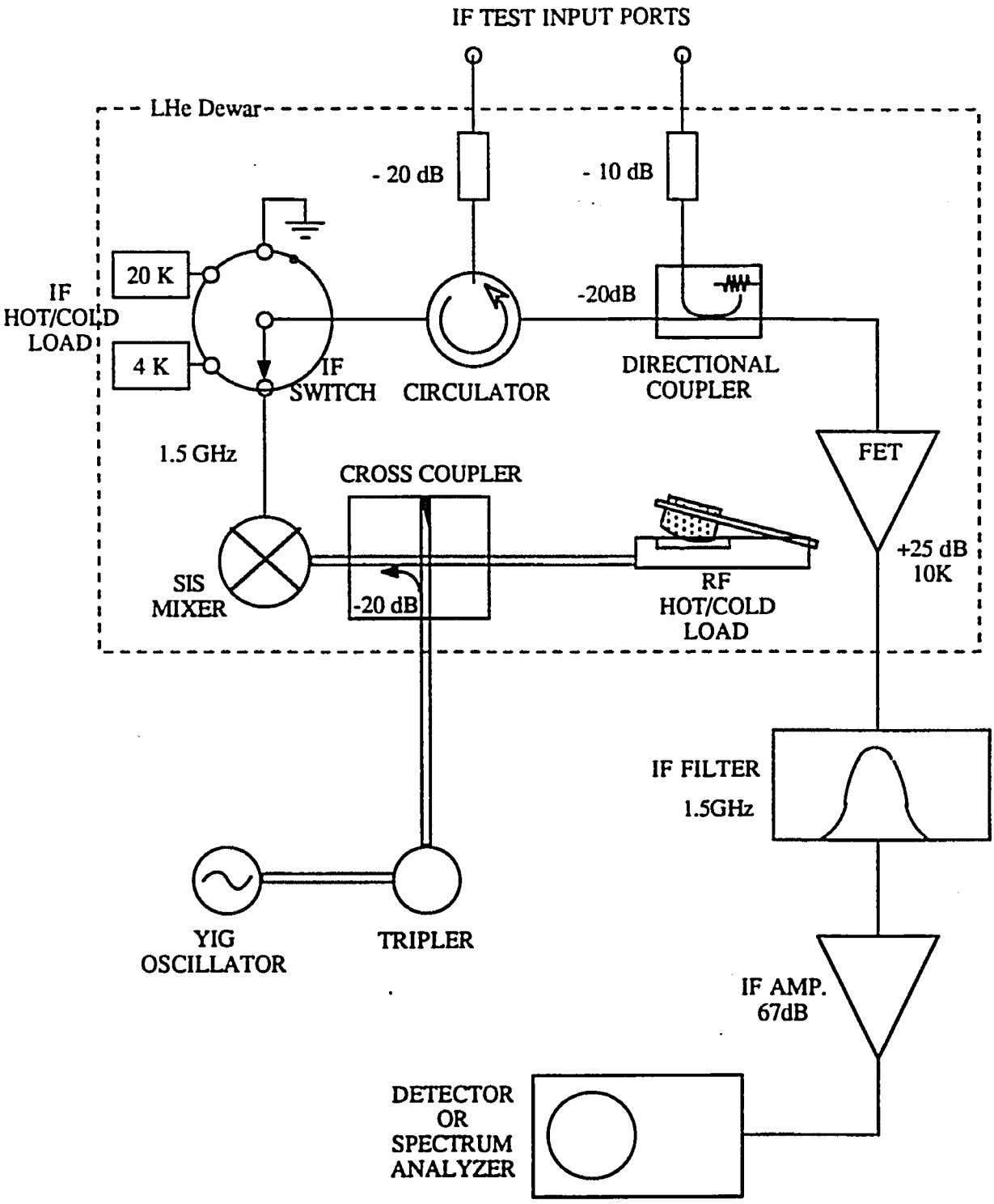

Fig. 4.1: Layout diagram of the test receiver. Objects within the dashed line are mounted in the cryogenic dewar. Single lines indicate coaxial lines, while double lines are waveguides.

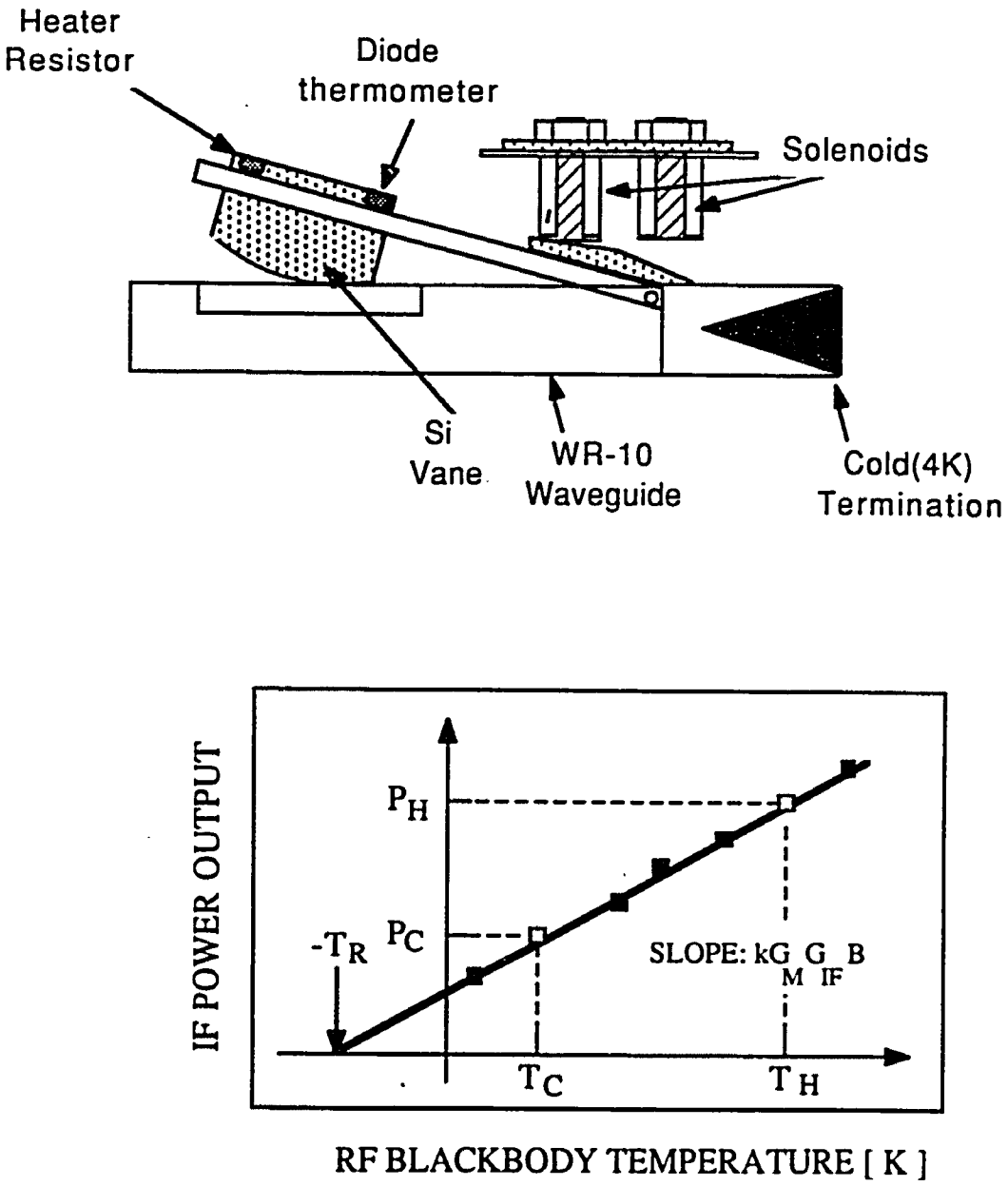

Fig. 4.2: The rf hot/cold load (top) and expected if power output curve (bottom). This design allows rapid switching between the loads, as well as slow cooling of the heated vane for more accurate measurements.

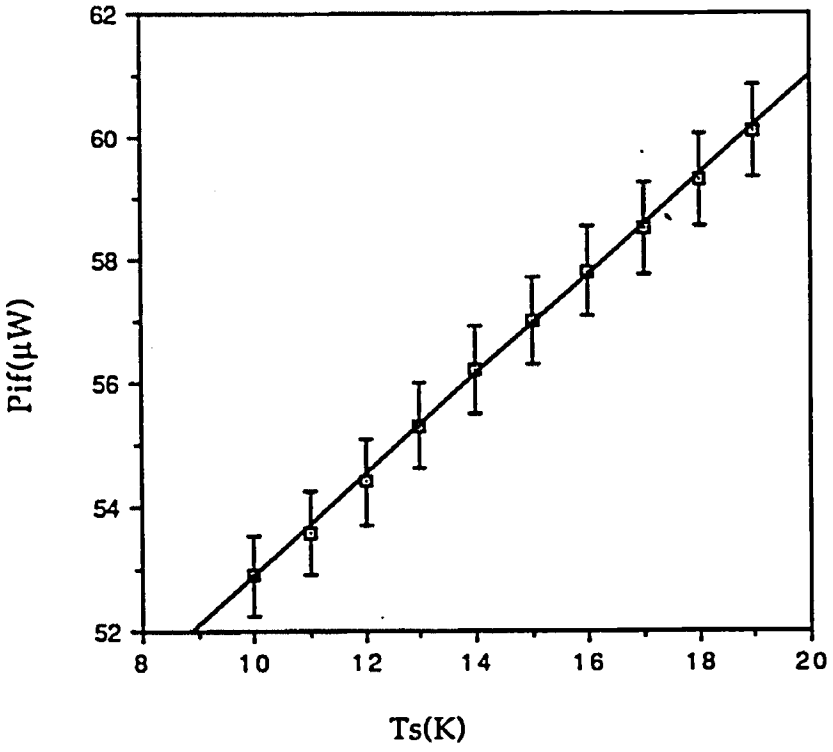

Fig. 4.3: Experimental if output power as a function of the vane temperature as read by the diode thermometer. The linearity of the line indicates that the vane is heated and cooled uniformly.

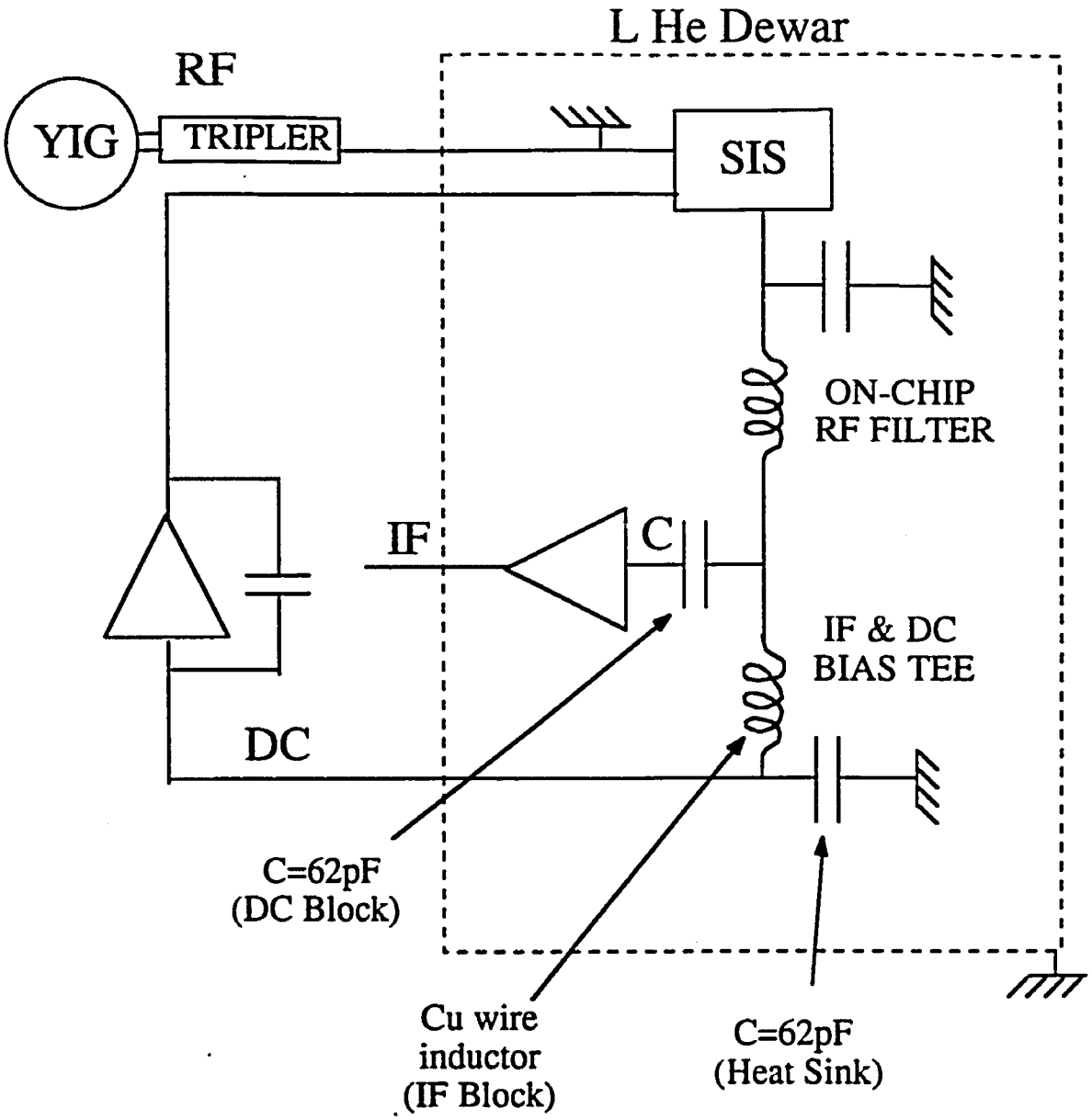

Fig. 4.4: Schematic layout of the bias tee and rf circuitry. All grounds shown in this figure are contacts to the dewar.

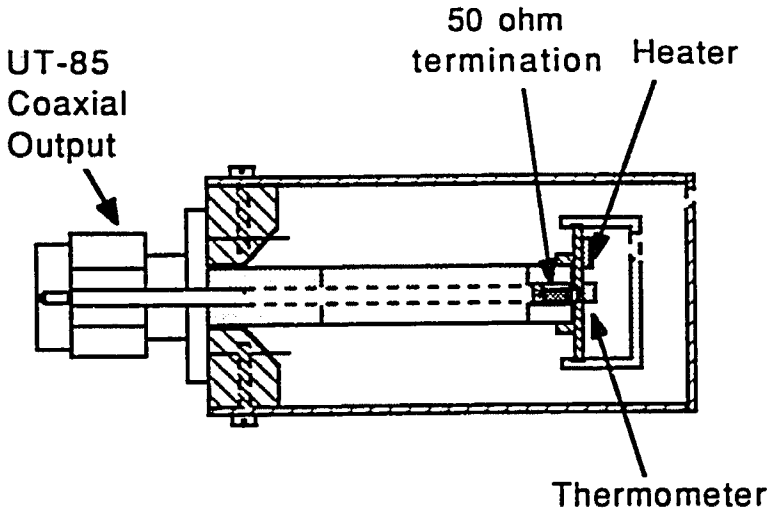

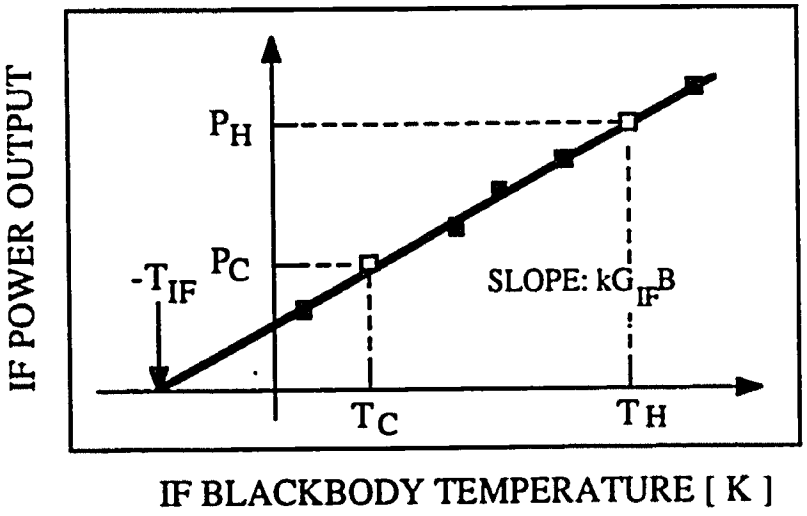

Fig. 4.5: Hot/cold load for the if system. The termination is heated with a 100Ω carbon resistor, and cooled slowly. As shown in the plot, the output gives information about the if gain and noise.

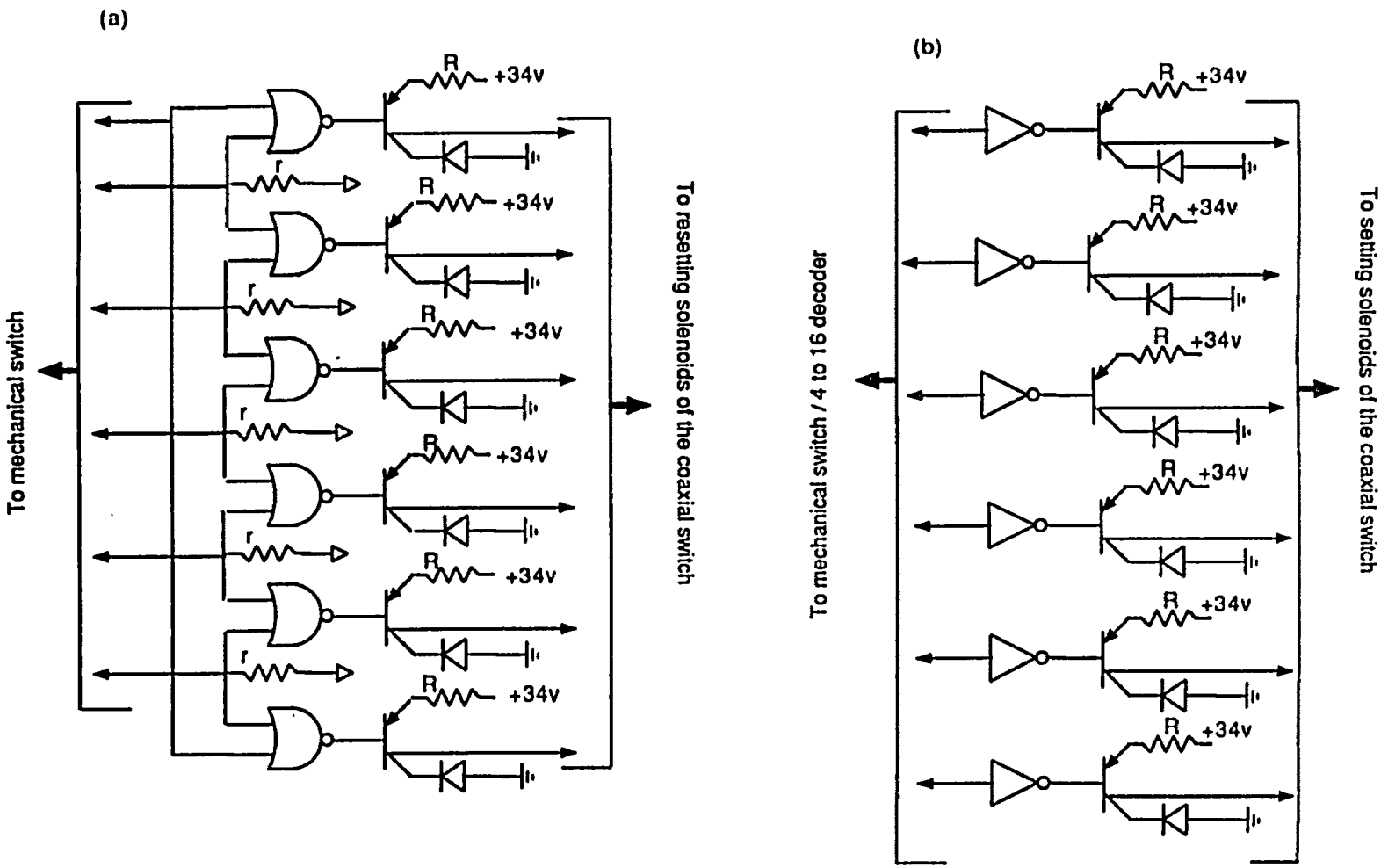

Fig. 4.6: Control circuitry for the if solenoid switch. A similar circuit is used for the rf hot/cold load solenoids.

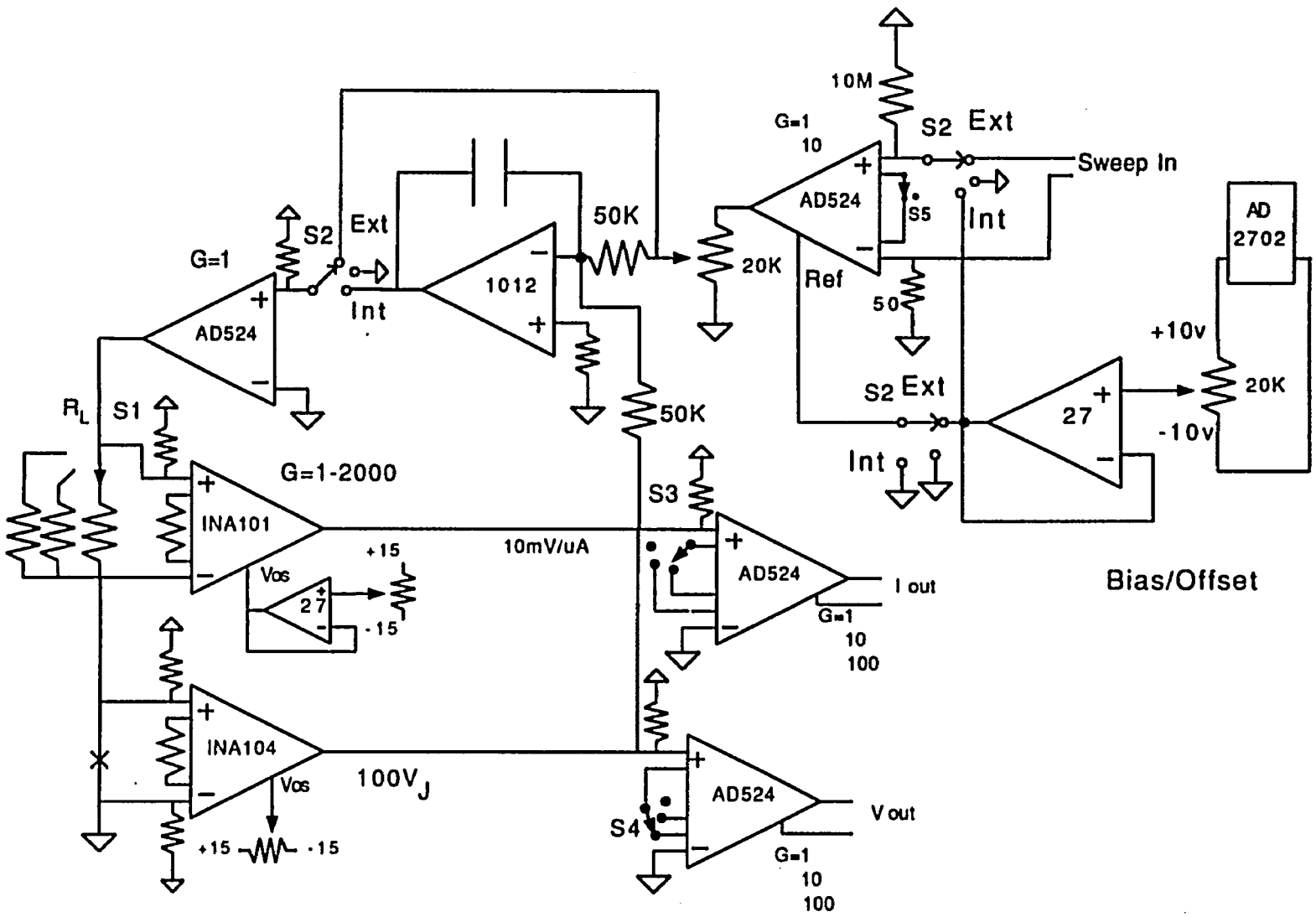

Fig. 4.7: DC biasing circuit for the mixer. This is a stable, low-noise, and versatile biasing scheme. The load line can be changed from voltage to current bias readily, without changing the gain. The bias can also be swept and externally controlled.

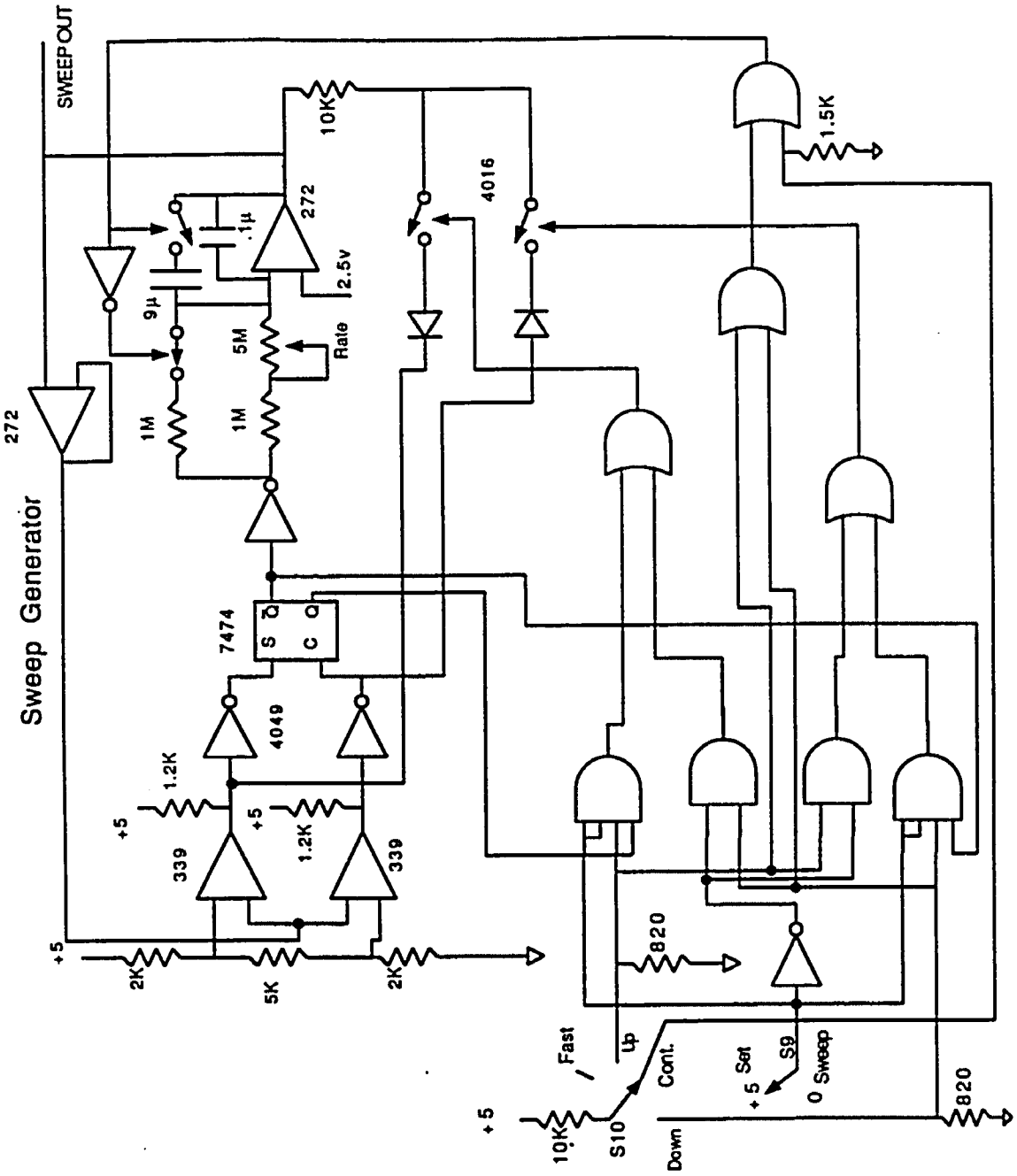

Fig. 4.8: Sweeping circuit for the mixer bias. The upper half is a basic oscillator, and the bottom half is a logic circuit to control the sweeper.

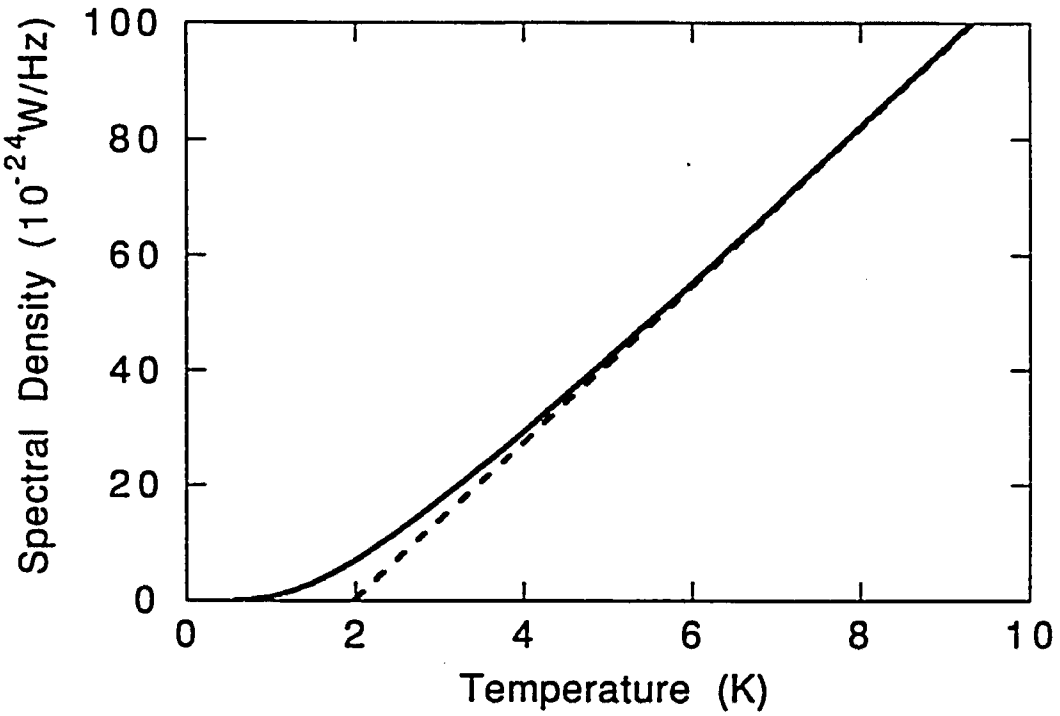

Fig. 4.9: Spectral power density at 100 GHz calculated using Plank's radiation law, and compared to a linear approximation. Above 4 K the difference is negligible.

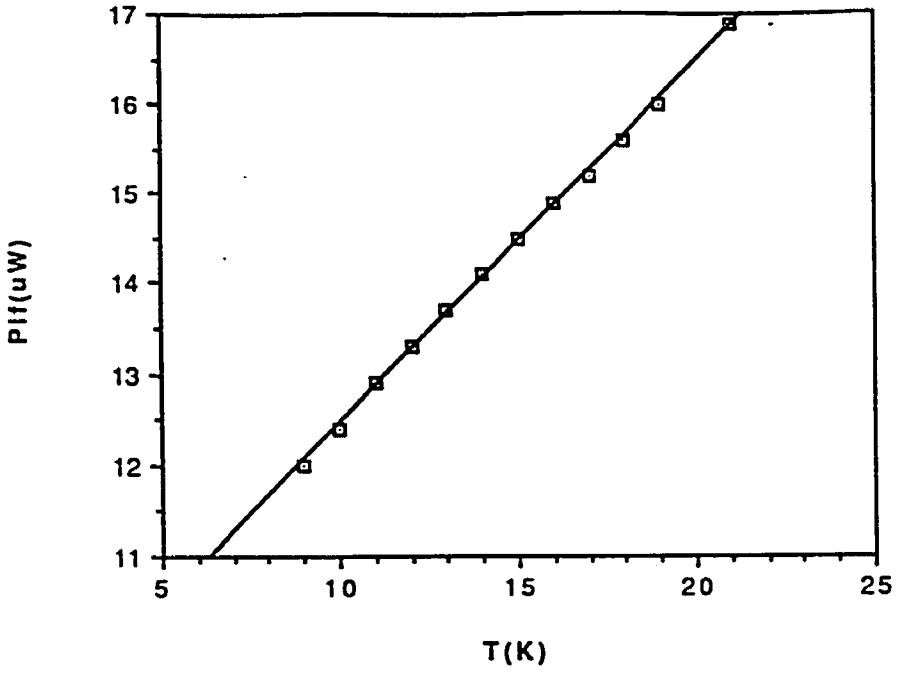

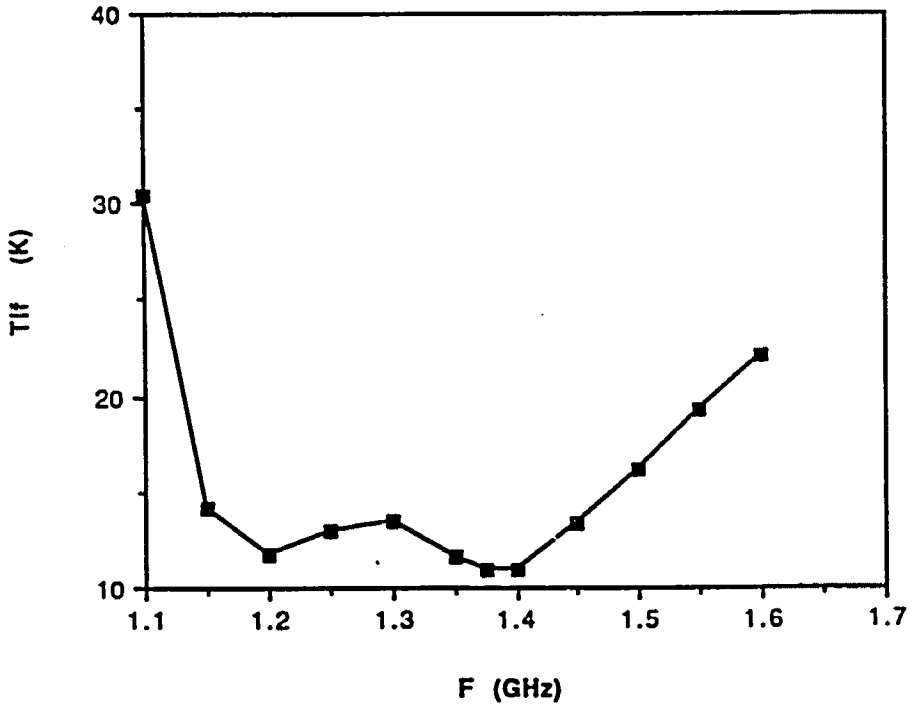

Fig. 4.10: If system data; a) The if output power as function of the if load temperature. The slope determines the gain and the x-intercept the noise. b) The noise temperature of the if system as a function of frequency. This is with a cooled FET amplifier. The frequency is swept using a 70 MHz bandwidth filter. Mixer measurements are taken between 1.35-1.45 GHz, where the if noise temperature is ~12 K.

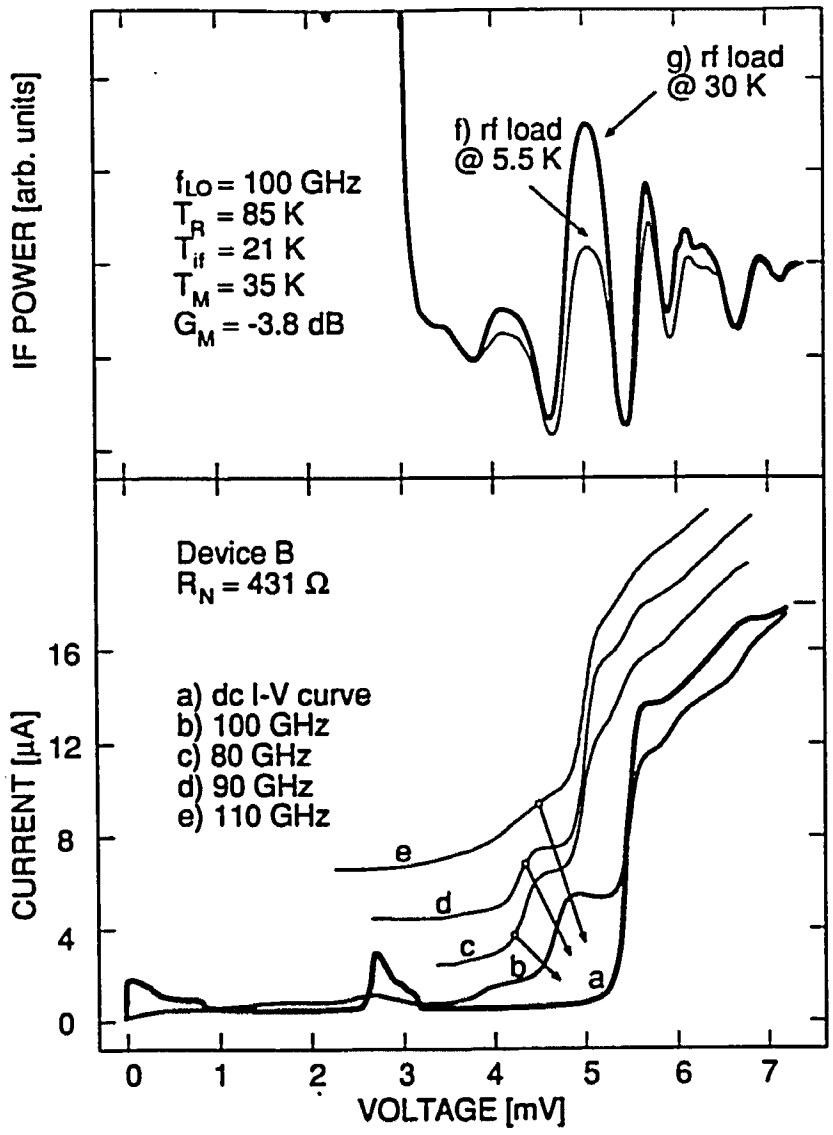

Fig. 4.11: Mixing results for device B; a) The if power output for two different load temperatures with a lo frequency of 100GHz. b) Pumped I-V curves for four lo frequencies. Note the negative slope at 100 GHz. This shows that proper tuning is achieved at mid-band.

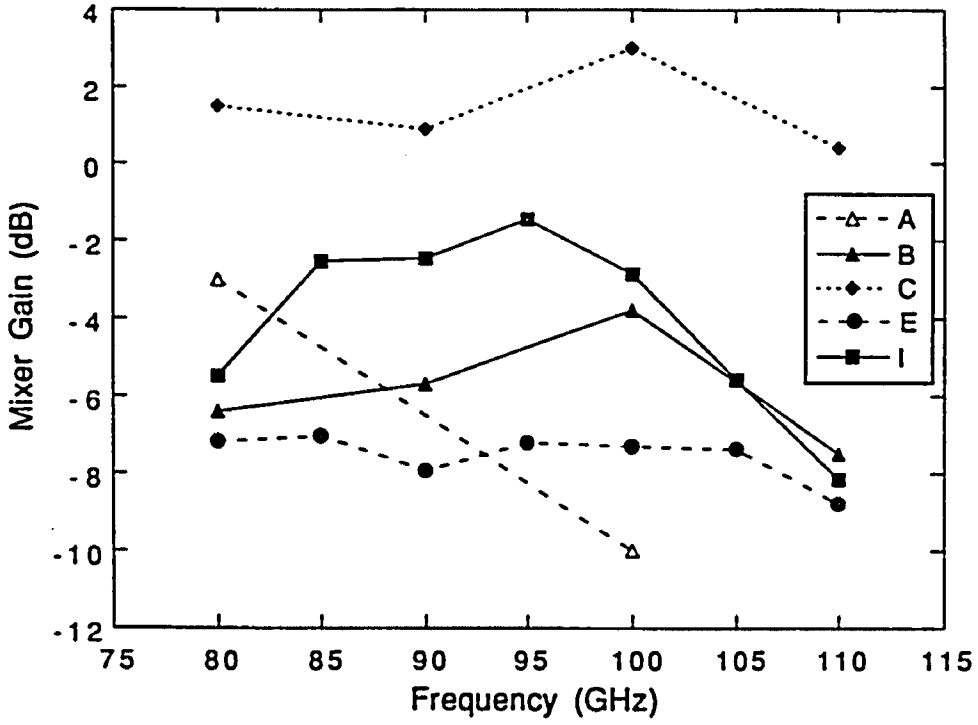

Fig. 4.12: Mixer gain for the devices reported in this chapter. Note that device C shows a gain larger than one over the waveguide band.

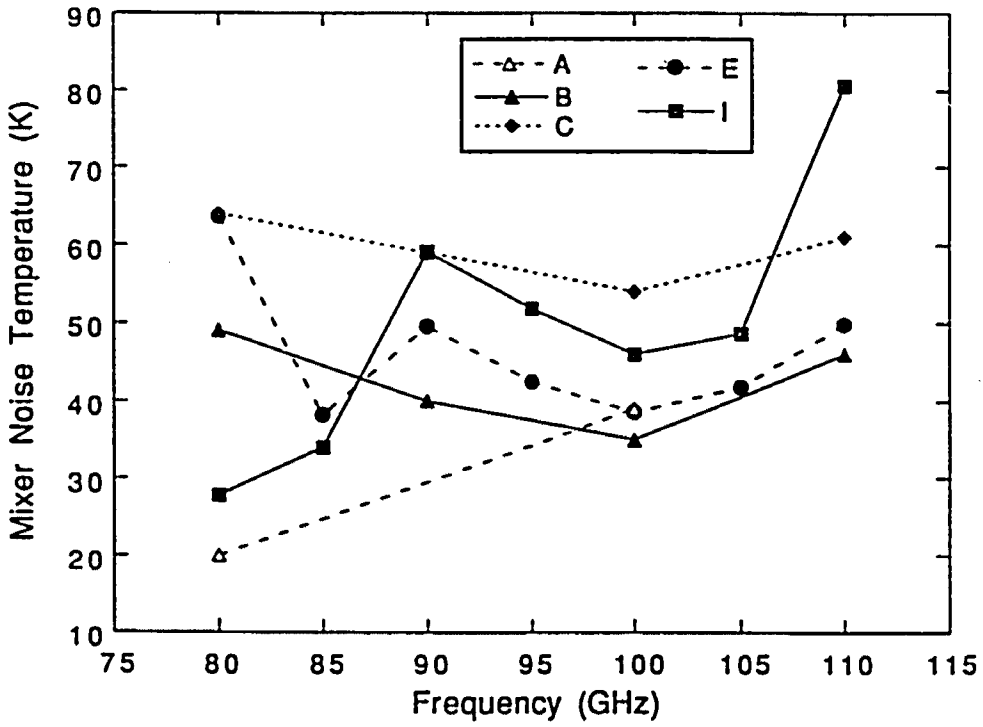

Fig. 4.13: Mixer noise temperature for the devices reported in this chapter. Note that the lowest noise occurs for device A.

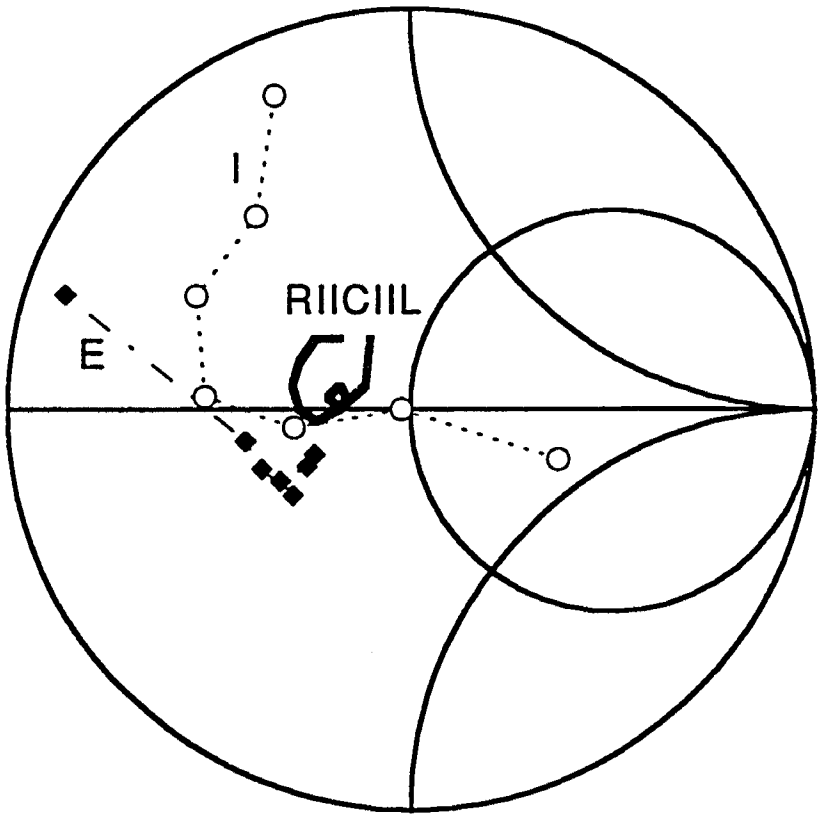

Fig. 4.14: The embedding admittance for devices I and E as calculated from the pumped I-V curves. Also shown is the embedding admittance inferred from scale model measurements (RIICIIL).

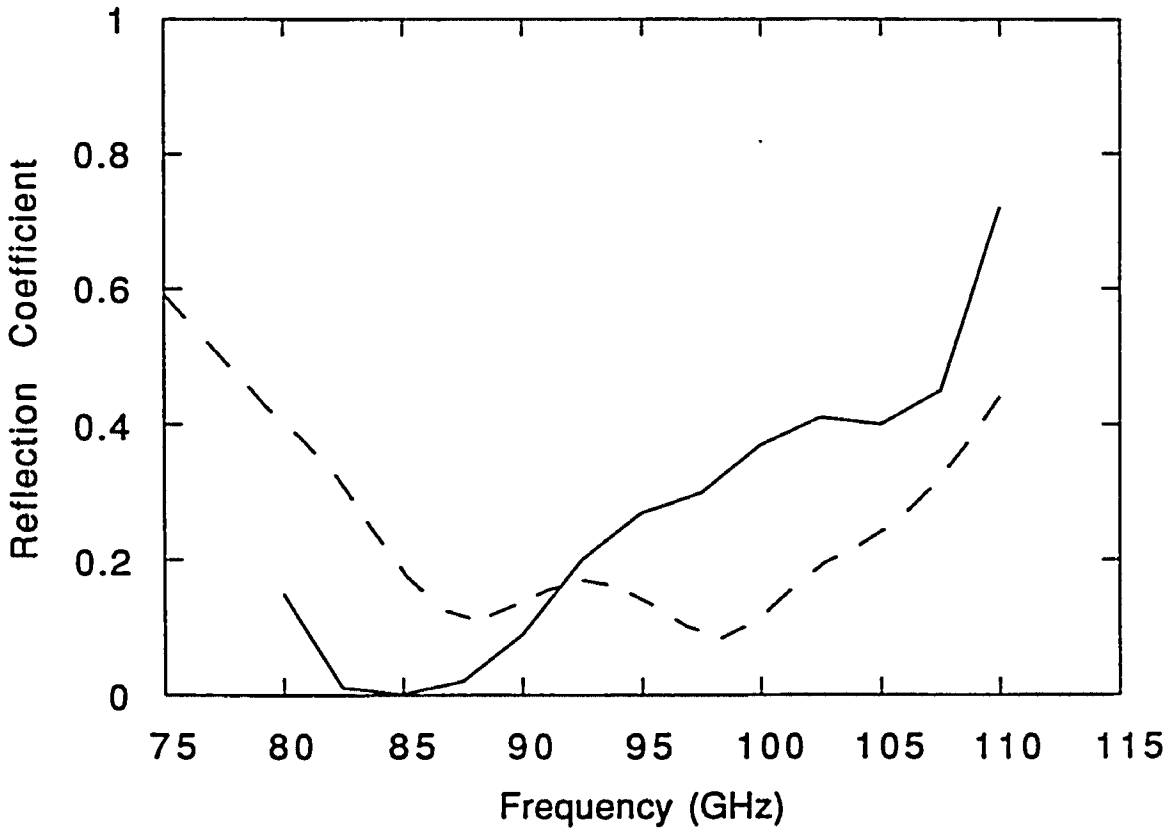

Fig. 4.15: The reflection coefficient of the scale model with a wire inductor and the actual mixer junction as inferred from the embedding admittance calculations.

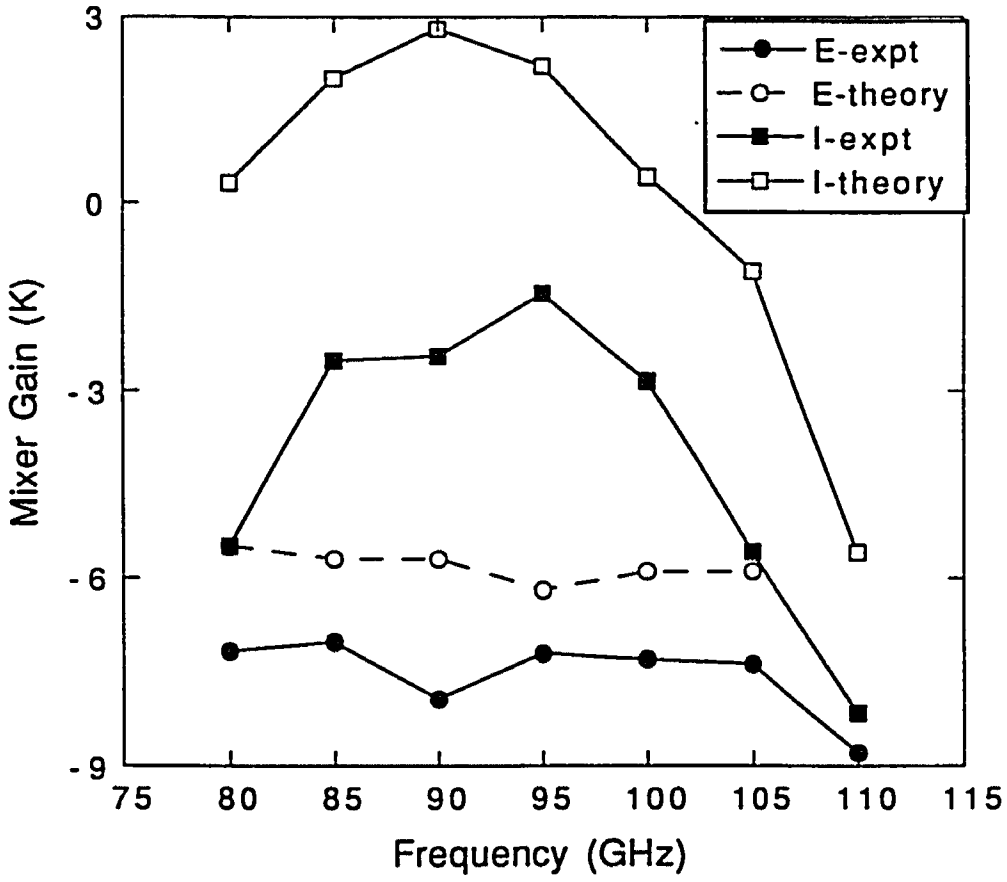

Fig. 4.16: Experimental and theoretical mixer gain for devices E and I.

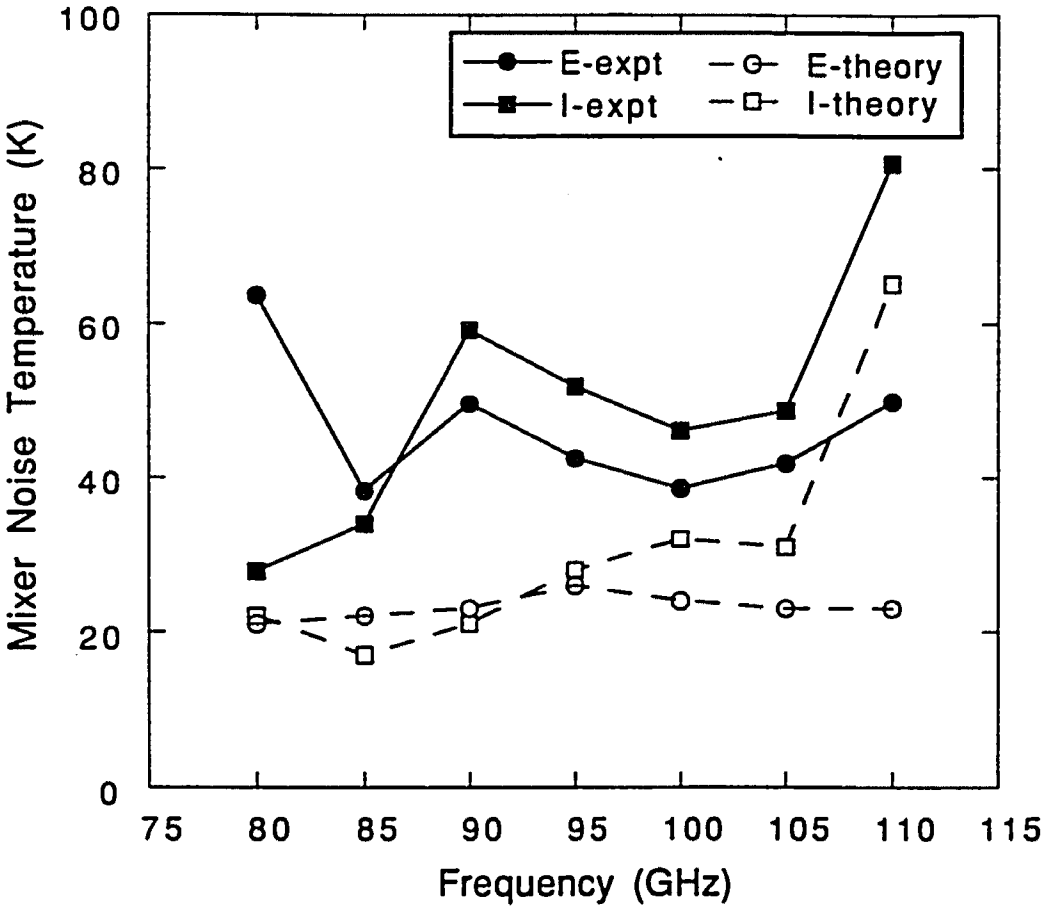

Fig. 4.17: Experimental and theoretical mixer noise for devices E and I.

V - Quasiparticle Admittance

In the previous two chapters the non-linearity in the quasiparticle dc tunneling I-V curve was used for heterodyne detection. In this chapter the photon assisted tunneling process is discussed in more detail, and the experimental observation of the high frequency quasiparticle tunneling admittance is presented.

5.1 Two-level atomic system

The interaction of a SIS tunnel junction with incident radiation can be better understood by considering a two-level system, particularly a two-level atomic system. In electromagnetic systems the admittance is given by $Y_\omega = H_\omega / E_\omega = I_\omega / V_{\omega,}$ and describes the ratio of an induced response to a driving force [Liboff and Dalman, 1985]. The quasiparticle susceptance and conductance describe the tunneling currents induced by an electrical field, or a time-varying voltage V_ω. Similarly, we can derive the currents induced in a two-level atomic system in response to an external electric field. This current is given by the time derivative of the magnetic dipole moment P(t). Let us consider an atom with two states separated by an energy of ΔE as shown in Fig. 5.1. In the presence of electromagnetic radiation of energy $\hbar\omega$ and amplitude E, the transitions between the two states are described by the electric dipole moment P(t) given by:

$$P(t) = \mathrm{Re}(\varepsilon_o \chi E e^{i\omega t}) \qquad 5.1$$

where E is the applied electric field, ε_0 the dielectric constant, and χ the atomic susceptibility [Yariv,1975]. The dissipation is equal to the product of the

electrical field and the time derivative of the electric polarization. The induced current then is given by the time derivative of the dipole moment,

$$I(t) \propto dP(t)/dt = Re(i\omega\varepsilon_o \chi E e^{i\omega t}), \qquad 5.2$$

Since the electric field E is proportional to the rf voltage V_ω, we can deduce the admittance of the system from this equation. This admittance is,

$$Y(\omega) = I(\omega)/V(\omega) = Re(i\omega\varepsilon_o \chi E e^{i\omega t})/E e^{i\omega t} \propto (i\omega\varepsilon_o \chi). \qquad 5.3$$

The problem of deriving the admittance is then reduced to calculating the atomic susceptibility $\chi=\chi'+i\chi''$. This calculation is carried out in Yariv using the density matrix formalism. The resulting equations include lifetime effects, and a resonance with a Lorentzian lineshape. Here we extend the results of that calculation to the transitions in a tunnel junction between two levels using the arguments above. We can then express a proportionality for the admittance due to tunneling between two states as:

$$Y_\omega = \frac{I_\omega}{V_\omega} = G_\omega + iB_\omega \qquad 5.4$$

where:

$$G(\omega_o) \propto \omega\chi'' \propto \frac{\omega}{1+(\omega-\omega_o)^2\tau^2}, \text{ and}$$

$$B(\omega_o) \propto \omega\chi' \propto \frac{\omega(\omega_o-\omega)\tau}{1+(\omega-\omega_o)^2\tau^2}. \qquad 5.5$$

Here τ is the quasiparticle lifetime in the excited state, ω_o is the energy difference between the two states expressed as angular frequency. These functions are plotted in Figure 5.2. This figure shows that there is a peak in the conductance at the resonant frequency with a full width at half maximum determined by the lifetime. The susceptance associated with a two-level

transition has a positive (capacitive) peak below resonance, and a negative (inductive) peak above. Away from the resonant frequency, both terms diminish, implying that transitions between these two levels do not play a role at those frequencies.

From the derivation of the two-level susceptibility, it follows that the real and imaginary components are Kramers-Kronig transforms of each other:

$$\chi'(\omega)=\frac{1}{\pi}\text{P.V.}\int_{-\infty}^{+\infty}\frac{\chi''(\omega')}{\omega'-\omega}d\omega',$$

$$\chi''(\omega)=-\frac{1}{\pi}\text{P.V.}\int_{-\infty}^{+\infty}\frac{\chi'(\omega')}{\omega'-\omega}d\omega' \quad . \qquad 5.6$$

where P.V. stands for the Cauchy principal value of the integral. A similar rule applies for the conductance and susceptance associated with a two level transition.

The physical significance of the complex atomic susceptibility is that the real part results in attenuation or absorption, while the imaginary part causes a phase delay [Yariv,1975]. The attenuation of the electrical field in a distance z is given by $e^{(\gamma/2)z}$, where:

$$\gamma(\omega)=-\frac{k\chi''(\omega)}{n^2}, \qquad 5.7$$

where n is the index of refraction, and k the propagation vector. The change in the phase delay per unit length due to the imaginary part is:

$$\Delta k(\omega)=-\frac{k\chi'(\omega)}{2n^2}. \qquad 5.8$$

In a similar way the conductance results in the attenuation of an incident field, while the susceptance delays the phase.

5.2 Theory of Quasiparticle Admittance:

In trying to understand photon assisted tunneling in a superconducting tunnel junction, one has to consider all quasiparticle states. The energy distribution of the density of states D(E) is given by:

$$D(E)dE = N(0)\frac{E}{\left(E^2-\Delta^2\right)^{1/2}}dE, \qquad 5.9$$

where N(0) is the density of states at the Fermi level of the electrode in the normal state and Δ is the gap energy [Bardeen,1957]. To derive at an expression for the collective tunneling, let us imagine that one electrode is grounded, while all electronic states in the other electrode are modulated by the incident signals. The applied signal may have a dc and an ac voltage component appearing across the tunneling barrier as:

$$V(t) = V_o + V_\omega \cos\omega t; \qquad 5.10$$

where V_0 is the dc bias voltage, and V_ω is the magnitude of the rf voltage at frequency ω. The resulting current is given by [Tucker and Feldman,1985]:

$$I(t) = a_o + \sum_{m=1}^{\infty}\left[2a_m \cos(m\omega t) + 2b_m \sin(m\omega t)\right]. \qquad 5.11$$

This expression includes all tunneling currents including higher harmonics of the signal. The first term, a_0, is the dc component of the tunneling current. The coefficients a_m and b_m are given by:

$$a_m = \tfrac{1}{2}\sum_{n=-\infty}^{n=+\infty} J_n(\alpha)\left[J_{n+m}(\alpha) + J_{n-m}(\alpha)\right] I_{dc}\left(V_o + n\hbar\omega/e\right)$$

$$b_m = \tfrac{1}{2}\sum_{n=-\infty}^{n=+\infty} J_n(\alpha)\left[J_{n+m}(\alpha) - J_{n-m}(\alpha)\right] I_{KK}\left(V_o + n\hbar\omega/e\right). \qquad 5.12$$

In these equations J_n is the Bessel function of order n, $\alpha = eV_\omega / \hbar\omega$, I_{dc} is the dc current and I_{KK} is the Kramers Kronig transform of I_{dc}. The second term in the series expansion of the a_m coefficient gives the *dissipative* component of the rf tunneling current at the signal frequency. Higher terms represent the higher harmonics of the rf current. Similarly the first term of the b_m coefficient gives the Kramers-Kronig transform of the dc I-V, while the second term represents the *reactive* current at the signal frequency and so on.

Since we wish to derive the tunneling admittance at the signal frequency, we will assume that all higher harmonics are negligibly small. This is true in most tunneling experiments since the junction's capacitive admittance is large at the higher harmonics. With this assumption, we include only the m=1 coefficient, and the tunneling current becomes:

$$I_\omega = I_\omega^D + iI_\omega^R, \qquad 5.13$$

where the dissipative and reactive parts are given by:

$$I_\omega^D = \sum_{n=-\infty}^{n=+\infty} J_n(\alpha)[J_{n-1}(\alpha) + J_{n+1}(\alpha)]I_{dc}(V_o + n\hbar\omega / e) \qquad 5.14$$

$$I_\omega^R = \sum_{n=-\infty}^{n=+\infty} J_n(\alpha)[J_{n-1}(\alpha) - J_{n+1}(\alpha)]I_{KK}(V_o + n\hbar\omega / e).$$

The complex admittance is given by:

$$Y_\omega = G_\omega + iB_\omega = \frac{I_\omega \cos\omega t}{V_\omega \cos\omega t}, \qquad 5.15$$

where the rf voltage amplitude is: $V_\omega = (\alpha\hbar\omega)/e$. By substitution we get:

$$G_Q(\omega, V_o) = \frac{e}{\hbar\omega} \sum_{n=-\infty}^{n=+\infty} J_n(\alpha)[J_{n-1}(\alpha) + J_{n+1}(\alpha)] I_{dc}(V_o + n\hbar\omega/e)$$

$$B_Q(\omega, V_o) = \frac{e}{\hbar\omega} \sum_{n=-\infty}^{n=+\infty} J_n(\alpha)[J_{n-1}(\alpha) - J_{n+1}(\alpha)] I_{KK}(V_o + n\hbar\omega/e). \quad 5.16$$

It is informative to consider the implications of these equations both as a function of frequency ω and dc bias voltage V_o. The frequency characteristics are useful for understanding the physical origin of the quasiparticle admittance, while the voltage dependence is useful for practical applications.

In these equations terms with n>1 represent tunneling events in which more than one photon is involved. For illustrative purposes it is useful to consider the case when only single photon tunneling is allowed. This is true for a small rf signal such that $\alpha << 1$. Including only the lowest order terms, we get:

$$G_Q(V_o) = \frac{e}{2\hbar\omega}[I_{dc}(V_o + \hbar\omega/e) - I_{dc}(V_o - \hbar\omega/e)]$$

$$B_Q(V_o) = \frac{e}{2\hbar\omega}[I_{KK}(V_o + \hbar\omega/e) - 2I_{KK}(V_o) - I_{KK}(V_o - \hbar\omega/e)]. \quad 5.17$$

The conductance then is the slope of the line connecting the current points one photon energy above and below the bias voltage. Thus one would expect a step-like structure within a photon step of the gap voltage (Fig. 5.3a). For voltage V_o below one photon energy of the gap, the conductance diminishes while far above the gap voltage the conductance approaches the normal state conductance. Thus, even though the density of states has a singularity at the gap edge, for the high frequency signal the quasiparticle absorption is smeared evenly over a range determined by the photon energy.

For single photon tunneling ($\alpha << 1$) The susceptance is the difference in two slopes of the Kramers Kronig transform as shown in Fig. 5.3b. The

physical origin of the susceptance has been discussed as a 'quantum sloshing' process [Tucker, 1979] in which a quasiparticle absorbs a photon and tunnels across momentarily, eventually emitting a photon of the same energy and tunneling back. In a classical sense this results in a phase delay in the transmitted or reflected wave. As a function of the bias voltage, the susceptance has a small positive peak one photon energy below and one photon energy above the gap voltage, and at the gap voltage exhibits a large negative peak.

It is important to distinguish at this point between the expressions valid for a two-level system and the ones for a tunnel junction. As expected, the tunnel junction admittance shows a dc-bias voltage dependence, which controls the energy difference between the electrodes. This is fixed at $\Delta E = \hbar\omega_o$ in a two-level system. Secondly, the frequency dependence is different for the two cases. The conductance of a tunnel junction, regardless of the bias voltage has close to a $1/\omega$ dependence following a sharp peak. On the other hand the atomic conductance has a stronger dependence on frequency ($\sim 1/\omega^2$) away from resonance.

One similarity between the two systems is that Kramers Kronig relations hold between the real and imaginary parts [Hu, 1990a]. Thus:

$$G_Q(\omega, V_o) = \frac{1}{\pi} P.V. \int_{-\infty}^{+\infty} \frac{B_Q(\omega, V_o)}{\omega' - \omega} d\omega', \qquad 5.18$$

and vice versa.

Previous calculations of the bias voltage and frequency dependence of the admittance was carried out by Hu (1990b). In Figure 3 of that paper the quasiparticle susceptance and the conductance of a tunnel junction are plotted for a fixed bias voltage as a function of frequency. The susceptance is shown

to cross zero at resonance, where the conductance has a peak. This would be expected for a two-level system. However it is not consistent with a similar calculation we have done for a tunnel junction. This calculation was done using Eq. 5.16 for a typical niobium tunnel junction dc biased at 2.3 mV, 0.5 mV below the gap voltage. As shown in Fig. 5.4, until the frequency approaches the difference in frequency between the bias voltage and the gap, the conductance is equal to the subgap conductance due to the leakage currents. At resonance, the conductance is at half maximum. The susceptance, on the other hand, increases uniformly from zero until resonance, where it has a large capacitive peak. After resonance it decreases sharply to a negative value and at above twice the gap frequency it approaches zero. Also shown in Fig. 5.4 is the Kramers-Kronig transform of the conductance, which overlaps the susceptance except a constant slope term, which is due to a dc offset. This confirms the accuracy of our analysis.

An interesting feature of the quasiparticle susceptance appears around the gap voltage. As shown in Figure 5.5, within one photon energy of the gap voltage, the susceptance curve rises from a minimum with two different slopes. First it rises sharply to about half a photon width, and then with about half the initial slope, it approaches the capacitive peaks on either side. This can be explained by the two-level model. In region 1, the quasiparticles absorb the energy of the photons to tunnel across, and there is a susceptance due to these transitions. This susceptance has the shape associated with the reactive part of the atomic susceptibility shown in Fig. 5.1. Thus it is capacitive for voltages (frequencies) below resonance, and inductive above. Above the gap voltage, the tunneling current resembles a stimulated emission process. This can be understood as creating a mirror image of the frequency axis in Fig. 5.1 with respect to the origin. Clearly the two-level susceptibility is now

inductive at energies below resonance, and it is capacitive above resonance as in region 3. Increasing the bias voltage of the tunnel junction from the gap voltage can be viewed as approaching resonance from lower frequencies. Thus the susceptance due to this process is initially negative, becoming positive above resonance. Adding these two processes of absorption and emission results in two slopes, since within half a photon energy of the gap voltage (region 2) both processes contribute inductively to the total susceptance.

5.3 Experimental Technique:

The quasiparticle admittance has a real and an imaginary component, and in order to extract these two orthogonal quantities one needs to either determine the phase and the attenuation (or absorption). A previous experiment has studied the admittance using a resonant technique, which limits one to a low input power level and to a single frequency [Hu,1990b]. The restriction to the low power limit is because the junction has to remain in the linear regime ($\alpha<<1$). We use a standing wave technique to measure the phase and the attenuation of the reflected wave from the tunnel junction [Liboff and Dalman, 1985]. The complex quasiparticle admittance is then calculated by normalizing the phase and the attenuation to those of a matched and of a short circuited termination. This method is not limited to the low-power limit, and can be used at various frequencies in the waveguide band.

In any transmission line, the reflected signal from an unmatched load along with the incident wave forms a standing wave pattern. Usually the maxima and minima of such a pattern are measured. The ratio of these two quantities is the voltage standing wave ratio (VSWR), and is a figure of merit

for how well the load is matched to the impedance of the transmission line. However this method does not determine the phase of the reflected wave unless the position of the maxima and the minima are also recorded. This is what is done on this experiment to determine both the magnitude and the phase of the reflected wave.

The power level of the standing wave as a function of distance is given by:

$$P_{SW}(d) = P_o\left[1+(\sigma\rho)^2+2\sigma\rho\cos\left(2\beta_g d+\theta-\theta_o\right)\right], \qquad 5.19$$

where P_o is the rms equivalent of the incident power, ρ is the magnitude of the reflection coefficient, d is the distance from the reference plane, θ_o is the phase at the reference plane, and θ is the measured phase. The phase constant, β_g is given by:

$$\beta_g = \frac{2\pi}{\lambda_g}. \qquad 5.20$$

Here the waveguide wavelength, λ_g is related to the free space wavelength λ_o by:

$$\lambda_g = \frac{\lambda_o}{\left[1-\left(\lambda_o/\lambda_c\right)\right]} \qquad 5.21$$

The attenuation factor σ is given by:

$$\sigma = e^{-\alpha' d} \qquad 5.22$$

where α' is the attenuation coefficient. From this formalism one then can extract the phase θ and the magnitude ρ of the reflection coefficient by measuring the standing wave amplitude as a function of distance from the

load. With this information in hand the complex load impedance can be calculated using:

$$\Gamma_r = \rho e^{i\theta} = \frac{Z_L - Z_o}{Z_L + Z_o} \qquad 5.23$$

where G is the complex reflection coefficient, Z_L is the load impedance, and Z_o is the line impedance.

The experimental setup is shown in Fig. 5.6. The signal source is the YIG tuned oscillator used in mixing experiments. The tripled output of this oscillator is fed into the dewar through a waveguide vacuum window. This window is made out of Rexolite and acts as a Fabry-Perot plate. Since the waveguide impedances on two sides of this window are approximately equal, the thickness is $\lambda_g/2$ to minimize reflections. The window is held in the waveguide by an adhesive, and forms a good vacuum window with ~ 0.1 dB insertion loss, and no observable degradation of the base pressure of the dewar.

In the dewar the signal travels through three waveguide sections; two are of coin silver, and one is a gold-plated stainless steel section. The signal is then directly coupled into the mixer block. The reflected wave travels through the same path in reverse. The standing wave power pattern resulting from the interference of these two signals is measured with a slotted line probe. The power coupled into this probe goes through an isolator into the signal port of a room temperature balanced Schottky diode mixer. The local oscillator source for this mixer is a cavity tuned Gunn diode oscillator. The output is amplified by a 4-8 GHz GaAs amplifier and heterodyned a second time with a diode mixer to 1.5 GHz. At this frequency additional gain

is obtained with a two stage GaAs amplifier. Finally the signal is filtered with a 70 MHz wide filter and detected.

The most crucial element of this setup is the Schottky mixer, since it is the first stage of detection. Its relatively low noise is important, as well as the low amount of local oscillator leakage out of the signal port typical of the balanced mixer. The isolator minimizes the effect of this leakage on the measured signal. This is to make sure that the standing wave power detected in the waveguide is due to the signal and does not have other frequency components which would cause a phase error.

Measuring the phase shift of the reflected wave relative to a reference plane is rather trivial as long as the reflections in the system are dominated by the mismatch at the load and not other reflections. However amplitude measurements are complicated by the fact that the signals are attenuated in the waveguides. A second difficulty is due to the noise power of the detection scheme. These two adverse effects can be understood by considering the extreme cases of large attenuation and high noise. When the attenuation constant is large, the magnitude of the reflected wave is very small compared to the incident wave, making it difficult to resolve the changes of power with position, and thus detect phase shifts. It is intuitive that the noise power of the heterodyne detection scheme should be much smaller (x10) than the power coupled into the probe. The probe can only be inserted into the waveguide until it distorts the standing wave pattern slightly. Both of these effects are minimized in this experiment.

5.4 Results:

The measured standing wave patterns for two different bias voltages are shown in Fig. 5.7. These are normalized to the incident power level after

the noise floor of the heterodyne detection system is subtracted. Note that for these two bias voltages the phase changes by almost 90°, and the magnitude of the reflection is different by ~30%. These standing wave patterns are measured for all relevant bias voltages and power levels.

By fitting the standing wave pattern to Equation 5.19, one can obtain the complex reflection coefficient. The phase and the magnitude of this reflection coefficient are normalized to the reference plane. This requires accurate knowledge of the attenuation coefficient, α'. This coefficient is calculated from the lengths of different waveguide sections, by estimating the temperature distribution [Pan,1989; Pan,1986].

The device used in this experiment is an array of four tunnel junctions, each with a normal state resistance of 10.5 Ω. The dc I-V curve along with its Kramers-Kronig transform is shown in Fig. 5.8. Two pumped I-V curves corresponding to the admittance measurements reported in the following section are also shown in this figure.

The complex reflection coefficient in the low power case is shown in Fig. 5.9. This is for a maximum normalized rf voltage of α=0.3 at the gap voltage where the array is best matched to the line impedance of 50 Ω. This condition is necessary for applying the low power approximation in the photon assisted tunneling calculation. In this approximation only single photon absorption/emission processes are allowed, and the expression in Eq.5.17 can be used. Note that the phase changes by almost 90° as a function of bias voltage.

This complex reflection coefficient is then used to calculate the load impedance which includes the quasiparticle admittance of the tunnel junction. The circuit model used in this calculation is shown in Fig.5.10. The tunnel junction is modeled as a lumped circuit element with a geometric

capacitance in parallel with a voltage dependent susceptance and conductance. The line impedance, Z_0 is assumed to be 50Ω, which is the design value for the output impedance of the ridge transformer and the microstripline. The series impedance of the radial stub at its apex, Z_r, is estimated from scale model measurements and CAD simulations to be -j 5Ω. The other parameter needed for extracting the quasiparticle admittance from reflection measurements is the geometric capacitance of the array. The specific capacitance of $Nb/AlO_x/Nb$ tunnel junctions with current densities below 5000 A/cm^2 is generally accepted to be 45 $fF/\mu m^2$ [Lichtenberger,1989]. There is an uncertainty in this figure since for higher current density junctions higher numbers have been quoted for the capacitance [Stern,1992]. Using 45 $fF/\mu m^2$ the array capacitance is estimated to be 45 fF, since the equivalent area of four $4\mu m^2$ tunnel junctions in series is $1\mu m^2$. The load impedance in the circuit model is then given by:

$$Z_L = Z_r + \frac{1}{i\omega C + G_Q + B_Q} \qquad 5.24$$

Z_L is calculated from the reflection data using Eqn. 5.23, and the real and imaginary quasiparticle admittances are then calculated using the equation above. This process can be represented on a Smith Chart as determining the center admittance and the reference angle of the chart.

The result of this calculation is shown in Fig. 5.11, along with the theoretical calculations for a normalized maximum rf voltage of $\alpha = 0.3$. Here we see that the agreement is good in both the conductance and susceptance. This is also the first observation of the singularity at the gap voltage in the reactive quasiparticle tunneling currents. The measured admittance is also plotted in Figure 5.12 on a Smith chart normalized to 1/50Ω . The normalization procedure is discussed further in the next section.

Figure 5.13 shows the quasiparticle conductance and susceptance for a normalized maximum rf voltage of α= 1.1. This is more relevant for practical applications of the quasiparticle currents such as heterodyne detection. Note that there is distinct structure in this data showing two and three photon absorption/emission processes.

5.5 Discussion:

The relevance of this experiment is discussed in the following two chapters. The bias voltage dependence of the quasiparticle admittance determines the performance of the tunnel junction as a mixing element as shown in Hu,1990b. I will discuss here the small, but visible discrepancies between theory and experiment.

The quality of the agreement between experiment and theory is satisfactory, since the singularity in the susceptance at the gap voltage is clearly seen in the experimental data. We also observe the small positive peaks at one photon energy away from the gap. However all these peaks are less in magnitude than expected. The conductance data shows the onset of the conductance at a photon energy away from the gap. This onset is not as sharp as theoretically expected.

The equivalent circuit that is used in extracting the array admittance from the reflection data is the most likely source of errors. The raw reflection data itself has negligible errors, since the probe position, and coupled power can be reproduced to great accuracy. A source of error is in shifting the reference plane from the probe position to the input microstripline. In doing this, it is assumed that there is a constant attenuation in the waveguide, the vacuum window adds no dispersion at the center frequency, the impedance transformation done by the ridge is perfect, and the input microstripline has

an impedance of 50Ω. Any inaccuracies in these assumptions can add a phase or a magnitude factor to the reflection coefficient. This would in turn effect the conductance and susceptance data, since both components of the admittance are transformed by the rf circuitry. Another source of error is due to the rf source. As stated in chapter 4, the YIG/tripler combination has a power spectrum with many resonant features. This implies that the output impedance might vary slightly over the frequency band, and cause errors in the analysis.

In the circuit model, the largest uncertainty is in the line admittance, Z_0. I mentioned in the previous section that extracting the array admittance from the reflection coefficient involves choosing a center admittance and a reference phase for the Smith chart. What is obtained in the reflection measurement is a magnitude (radius on Smith chart), and a phase (angle on Smith chart) for each bias point. Choosing a different Z_0 for data analysis, changes the radial distribution of the data. The reference phase is mostly determined by the choice of the capacitance C and the radial stub impedance Z_r, which is assumed to be purely reactive. A smaller capacitance disperses the data over a larger angular scale on a Smith chart. The effect of Z_r is to rotate the data on a Smith chart.

The reflection coefficient is a phasor quantity; so is the quasiparticle admittance. What is determined in this experiment is the precession of the reflection phasor as a function of bias voltage. Choosing a reference phasor to normalize the reflection phasor expectedly changes the calculated admittance phasor. Ideally one would measure a reference reflection coefficient phasor of two known loads: a short or open circuit and a matched load. The matched load gives a measure of stray reflections in the transmission medium and the effect of any impedance transformations. The short/open circuit

measurement would be useful in determining the phase constant (since it is 90° or 180° at the load), and the attenuation. With this knowledge one could calculate any load admittance from the reflection coefficient exactly. This was not done in this experiment, mainly due to the difficulty in obtaining a perfect short or open circuit. Also the rf source used in this experiment was not frequency or phase locked. Since the YIG cavity is very sensitive to temperature and pressure, it is difficult to reproduce the frequency between experiments without frequency locking. Since the electrical length of the transmission line in this experiment is rather long (~100λ), frequency and phase reproducibility is very important for normalization. Without this capability, the data was analyzed using parameters inferred from design goals and other experiments.

In spite of the good agreement between experiment and theory, one feature does stick out. This is an apparent peak or dip in the conductance at the gap voltage. Unfortunately this feature is strongly dependent on the choice of parameters used in the analysis. Another group has also observed structure in the conductance close to the gap voltage [Hu,1990b]. This structure could be due to the proximity effect. Another feature is the broadening of the peaks in the conductance. This broadening is apparently not rf power dependent. This implies that it is not due to the instability of the measuring apparatus. It may be due to inelastic tunneling which is not included in the photon assisted tunneling theory. The theory assumes that the dc I-V curve contains all necessary information about the density of states and tunneling. The theory also assumes weak coupling between the electrodes, which should hold for tunnel junctions with current densities below 10 kA/cm^2. Another approximation made in the analysis that may add errors is the equivalence of an array to a single junction. This approximation

ignores non-uniformities in the areas of the junctions. Such non-uniformities would result in different bias conditions for each junction in the array. This effect at the rf frequencies can manifest itself as a step-like structure and broadening in the rf conductance.

In the following two chapters some practical applications that arise from these measurements are discussed. One application that has been proposed is a parametric amplifier using the voltage dependent susceptance as a parametric element [Lee,1982]. The experimental technique used in this experiment can be extended to observing the complex admittance in different devices. Reflection measurements have been carried out in Josephson point contacts to determine the real and imaginary Cooper pair currents [Michelson,1981; Rifkin,1976; Rudner,1979]. However there is still much disagreement both in the experimental and theoretical results [Zorin,1979]. It has been suggested that a careful experiment at a frequency much higher than 10 GHz with a well known circuit will yield an answer [Feldman,1980]. The measurement technique described here seems applicable.

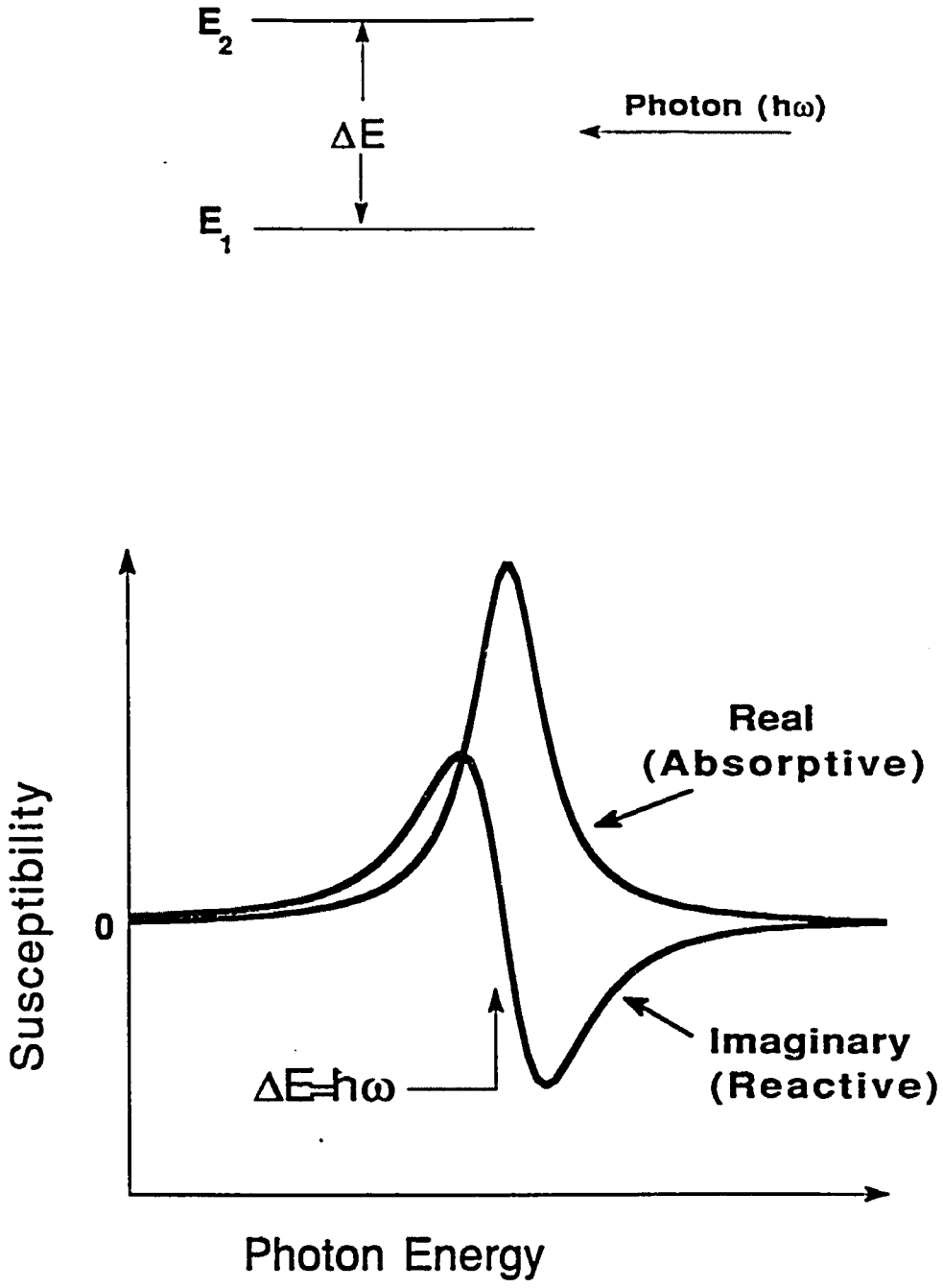

Fig. 5.1: A two-level atomic system in a radiation field (top), and its susceptibility as a function of the incident photon energy. The absorption has a Lorentzian Lineshape due to lifetime broadening.

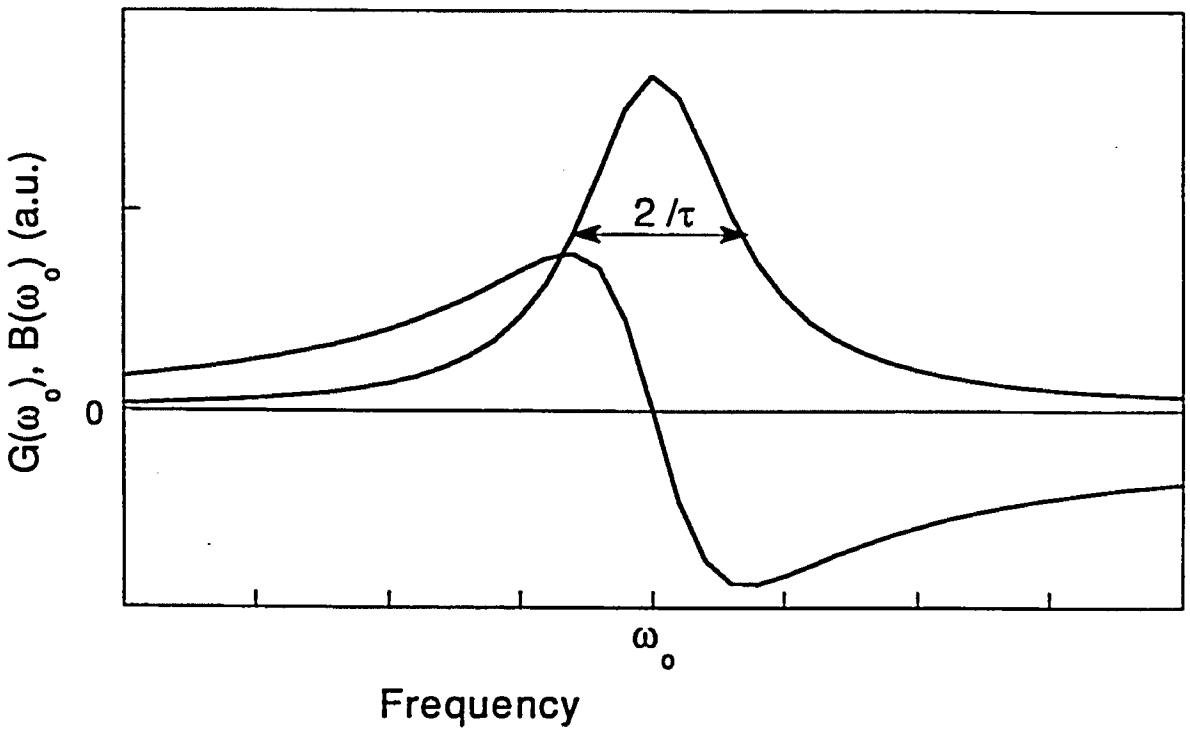

Fig. 5.2: Conductance and susceptance of associated with a two level transition. τ is the particle lifetime, and ω_o is the energy difference in frequency between the two levels.

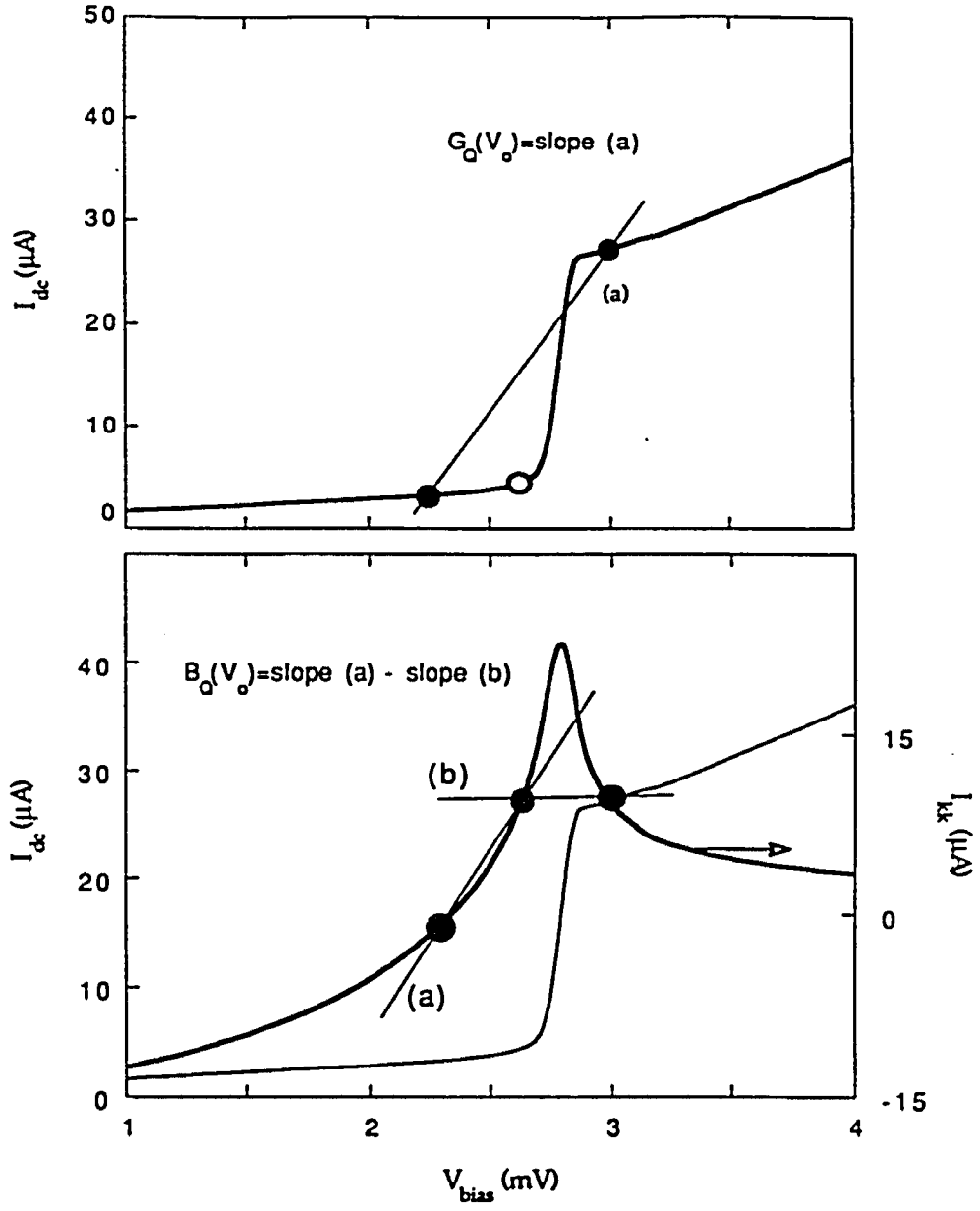

Fig. 5.3: Method of calculating quasiparticle conductance and susceptance in the low-power limit. The conductance (top) for the bias point indicated by the hollow circle is equal to the slope of the line connecting current points a photon energy above and below the bias point. The susceptance (bottom) is the difference of two slopes between points on the Kramers Kronig transform as shown. These point are differ in voltage by one photon energy as well.

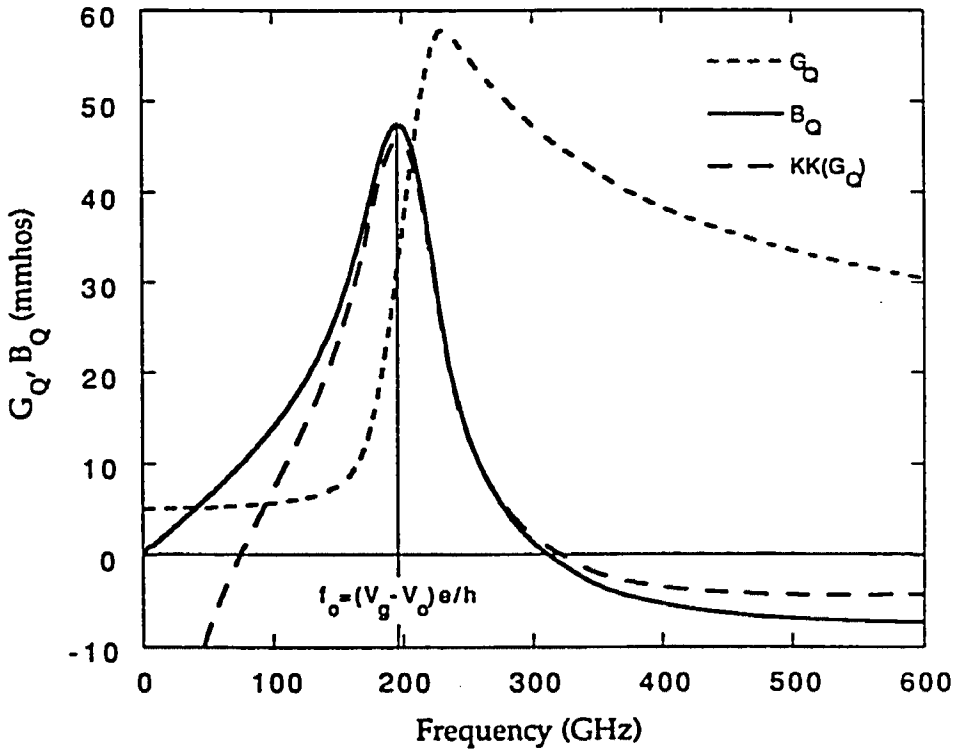

Fig. 5.4: Calculated quasiparticle conductance and susceptance as a function of frequency for a fixed bias voltage of 2.5 mV. Also shown is the Kramers Kronig transform of the conductance which coincides with the shape of the susceptance curve. Note that the susceptance has a capacitive peak at the half maximum of the conductance. This frequency corresponds to the energy difference between the singularities on the two electrodes.

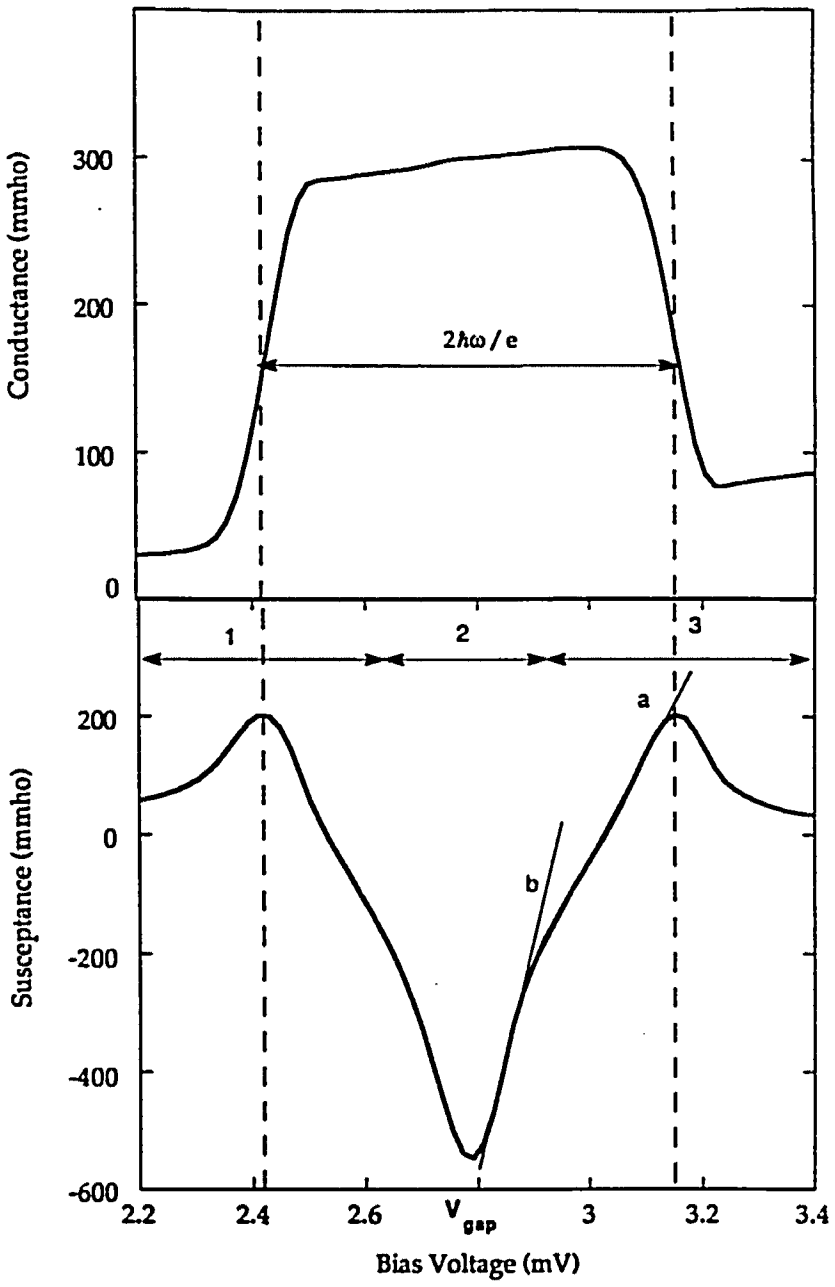

Fig. 5.5: Detail of the quasiparticle conductance and susceptance as function of bias voltage around the gap. The conductance has a relatively flat plateau close to the gap voltage. The susceptance displays a large inductive peak at the gap increasing to two capacitive peaks. The difference in the slopes of (a) and (b) is approximately a factor of two, implying that the absorption and emission processes contribute to the susceptance within a half photon width of the gap.

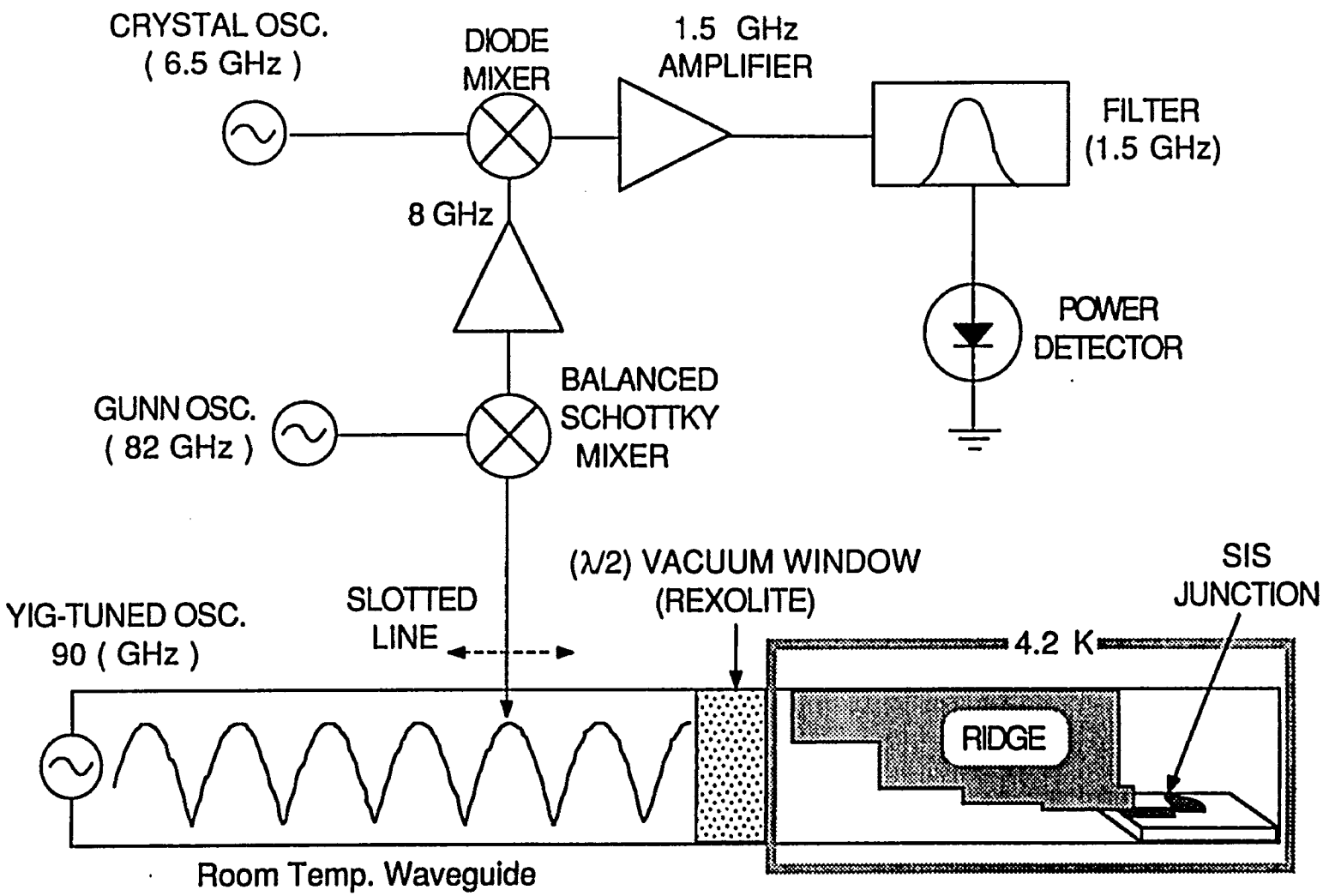

Fig. 5.6: Experimental setup for the reflection coefficient measurements.

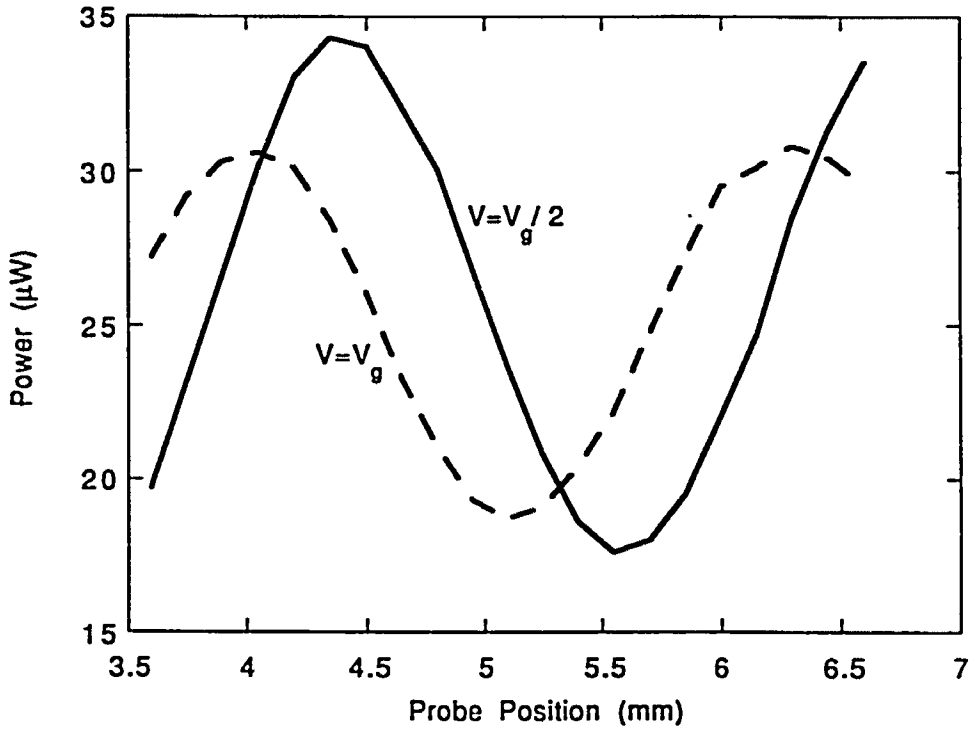

Fig. 5.7: The measured power standing wave pattern inside the waveguide for two bias voltages. There is a difference in the relative phase and amplitude of these two patterns.

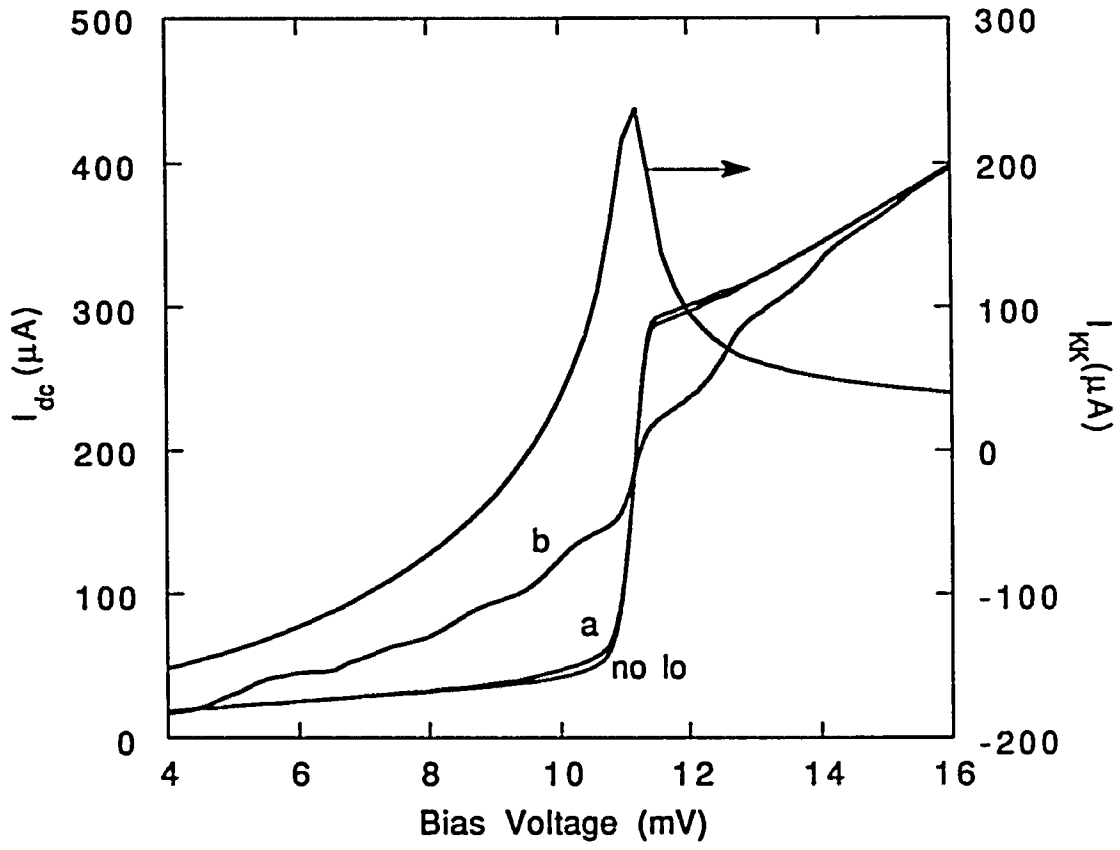

Fig. 5.8: The dc I-V curve, its Kramers Kronig transform, and the pumped I-V curves for low input power (a), and high input power (b). Curve (c) clearly shows photon assisted tunneling steps, while (a) is in the low-power limit.

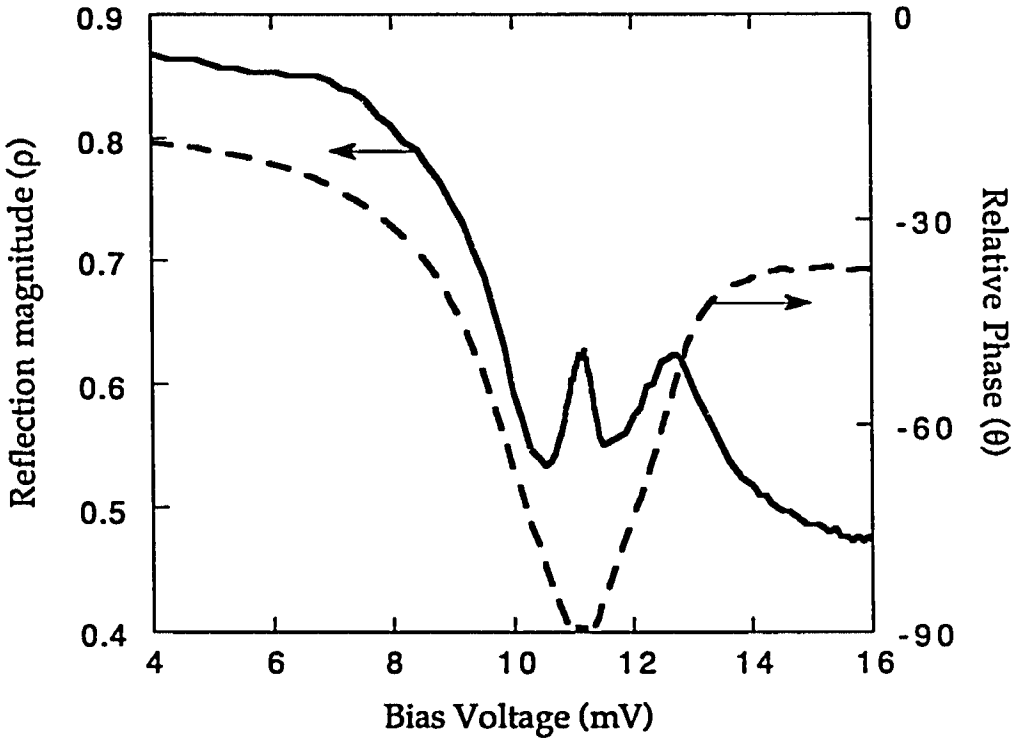

Fig. 5.9: The measured reflection coefficient as a function of dc bias voltage. Note that there is close to 90° phase change close to the gap voltage which is mainly due to the susceptance. The magnitude of the reflected signal is large far below the gap since the junction is almost an open circuit, and it is smaller far above the gap, since the normal state resistance is close to the line impedance of 50Ω.

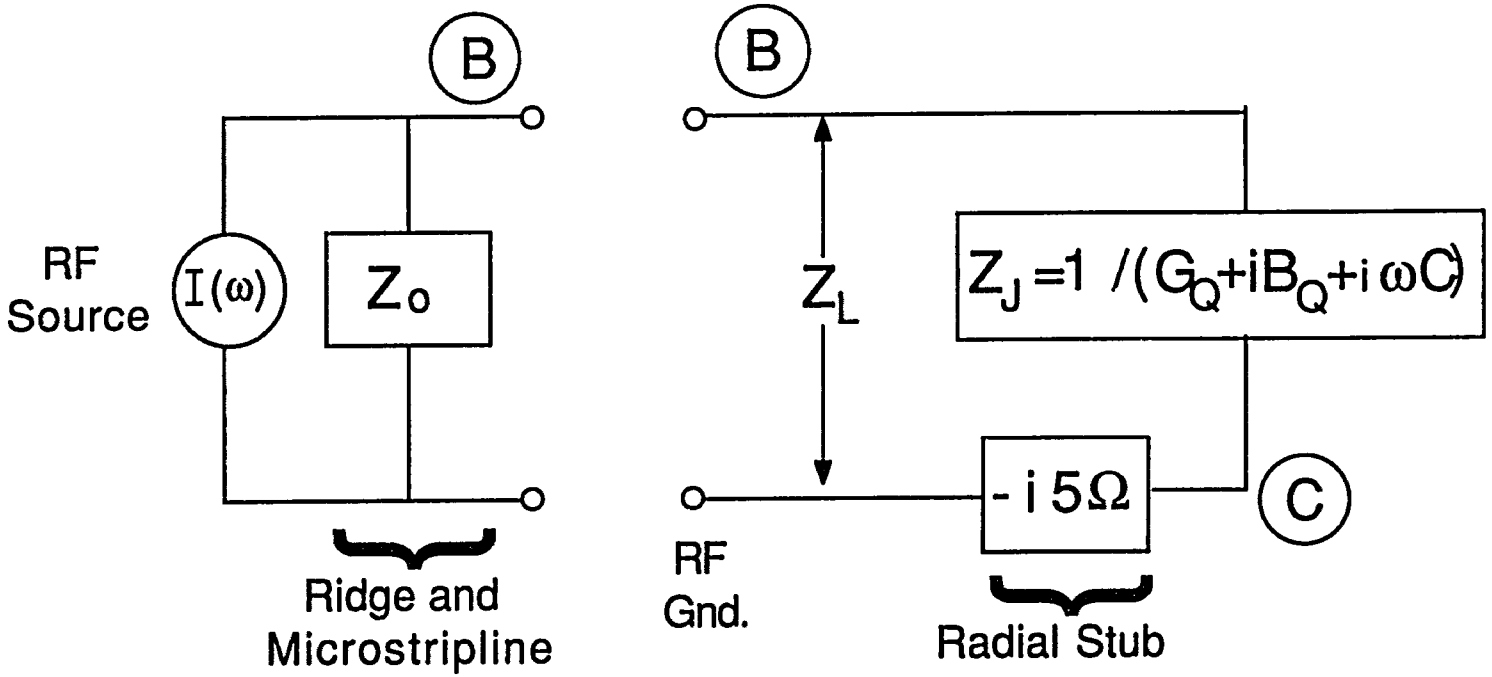

Fig. 5.10: The rf equivalent lumped element circuit model used in extracting the quasiparticle admittance from the load impedance. Here Z_o is assumed to be 50Ω which is the design value. The markers indicate positions on the rf circuit shown in Fig. 3.4.

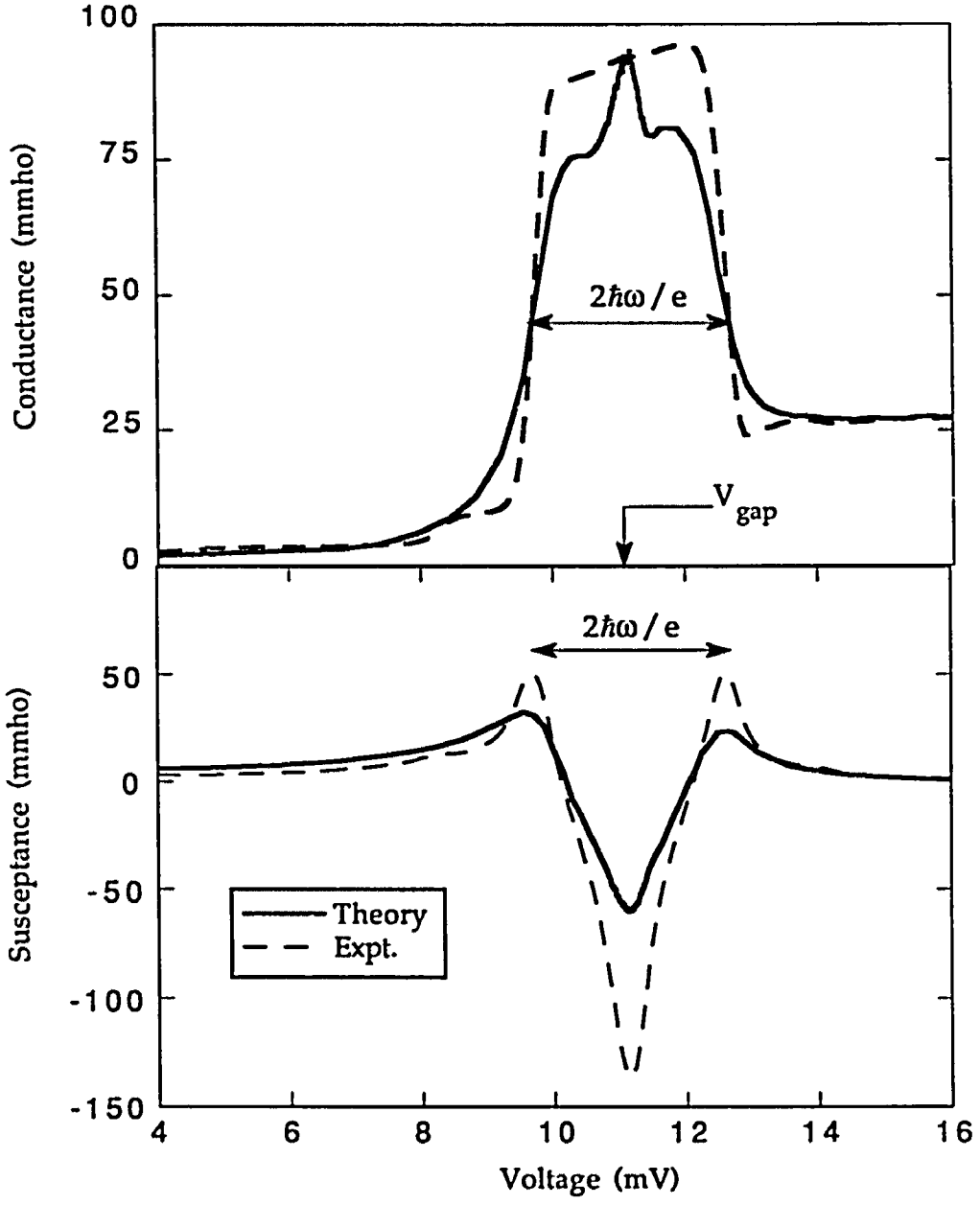

Fig. 5.11: The experimental and theoretical quasiparticle admittances for an input power which corresponds to $\alpha \approx 0.3$ at the gap voltage.

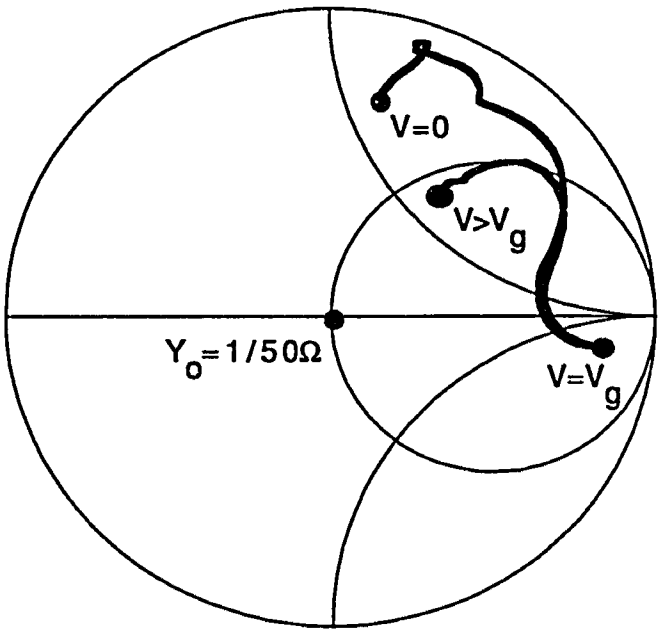

Fig. 5.12: The quasiparticle admittance plotted on a Smith chart normalized to 20 mmhos.

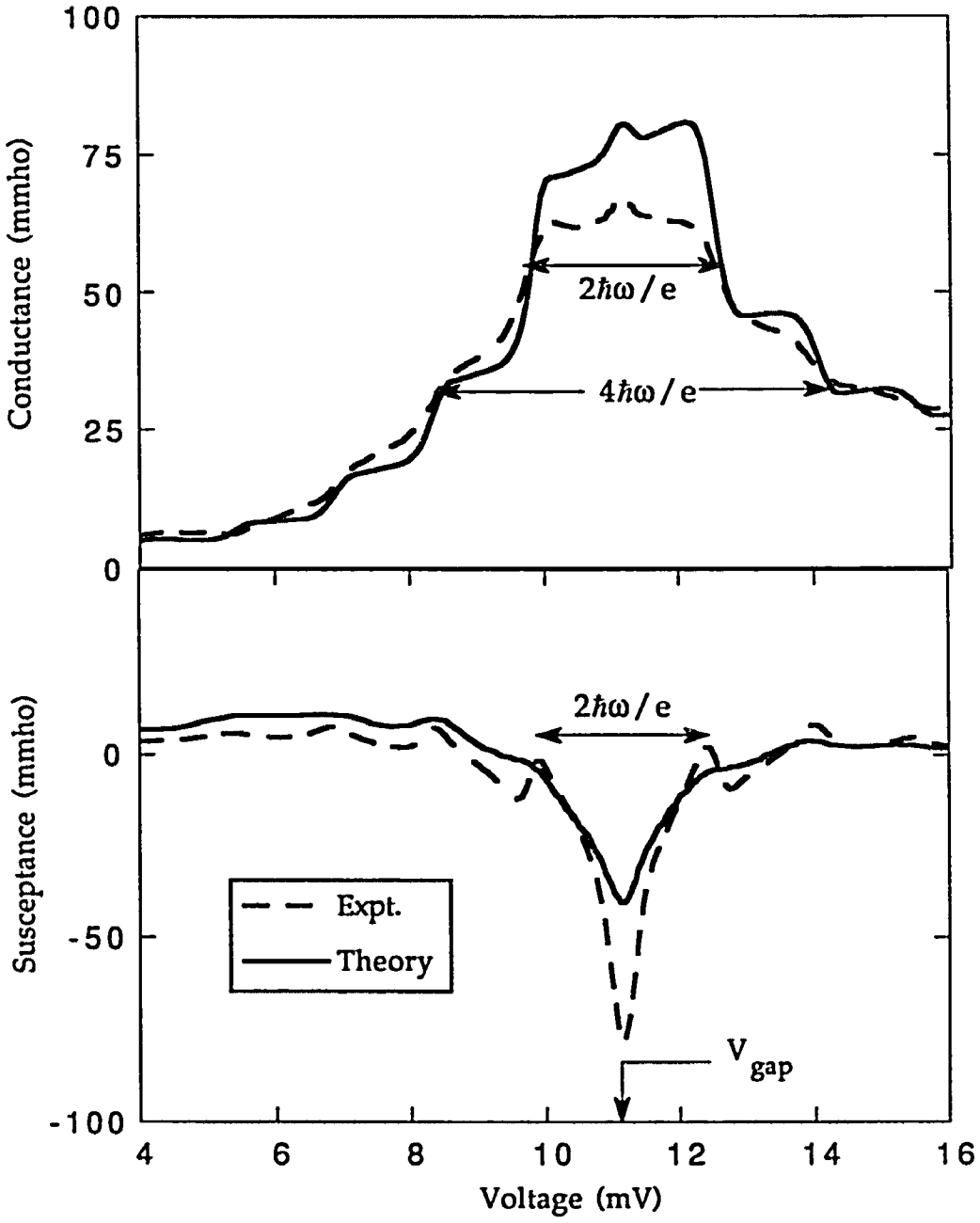

Fig. 5.13: The experimental and theoretical quasiparticle admittances for an input power which corresponds to $\alpha \approx 1.2$ at the gap voltage.

VI - Quasiparticle Tuning

In this chapter I will discuss mixing experiments which employ the quasiparticle admittance of a superconducting tunnel junction as the tuning element for a SIS mixer. This is the first demonstration of an electronic on-chip tuning element for a superconducting detector.

6.1 Motivation:

There is substantial effort to extend the operation of SIS mixers into the sub-mm range and to construct imaging arrays [Blundell 1992, Wengler 1992]. Above 30 GHz, the admittance due to the geometric capacitance of the tunnel junction becomes significant. A finite capacitance is desirable in order to minimize out-of-band noise detected by the harmonics of the Josephson (pair) current as discussed in previous chapters. At 100 GHz a good compromise is achieved with a $\omega R_n C$ product of about 4, where R_n is the normal state resistance. For $\omega R_n C \geq 1$ one must resonate the junction capacitance C at the frequency of operation [Kerr 1992]. Mechanical tuning elements in the form of waveguide backshorts have been used successfully to tune out the capacitance at frequencies up to 500 GHz, but become increasingly cumbersome above 200 GHz [Kerr 1992]. These backshorts come mainly in two forms; a double-stub tuner configuration to tune out the conductive and susceptive mismatches separately or an E-plane and a H-plane tuner to again resonate the orthogonal components of the incident field. Some designs utilize only one such backshort, sacrificing the tuning range of one of the components for ease of use. Still all such elements become cumbersome above 200 GHz and likely impractical for array applications. A more recent design has a shorting metallic bar which slides over a coplanar transmission

line, providing a variable backshort which can be in close proximity to the device at high frequencies [Lubecke,1991]. Scale modeling results of this approach have shown relatively low-loss (<1dB) and a wide range of tunability in the double stub tuner configuration, however implementation at practical frequencies has proven rather difficult.

The practical tuning approach for array applications is to use fixed integrated tuning elements which are microfabricated on the same chip as the device, and are non-dissipative. A simple approach is to place a microstrip in parallel with the mixer junction. An open circuited stub of length $(3/8)\lambda_0$ in such a configuration will resonate the junction capacitance at frequency f_0. The resonance bandwidth will be a third of the intrinsic bandwidth of the device [Büttgenbach,1992]. This limits the range of operation for the mixer, but is easy to implement. In this work we have used thin film inductors taking advantage of the magnetic inductance in a rf-current carrying small wire. Even though we have achieved good coupling with this approach, these inductances are not variable, thus making it impossible to adjust the resonant frequency or to compensate for variations in microfabrication. The ideal tuning element for a mixer would be microfabricated on-chip, and provide variable tuning with minimal dissipation.

In this chapter I will discuss two approaches to obtain on chip electronically variable tuning. Previous attempts to obtain electronic tuning with a superconducting circuit used the ac Josephson current. This current is reactive in the zero voltage state and the magnitude of this inductive reactance depends on the dc bias current. Use of this pair reactance as a tuning element has been proposed, but not tested with success [Irwin, Kaplan]. The disadvantage of this approach is that the Josephson inductance is highly nonlinear, and can introduce large noise sidebands resulting in

similar problems as with Josephson effect mixers. This is discussed in the last section.

6.2 Quasiparticle Tuned Mixer:

I demonstrate in this chapter a novel electronic on-chip tuning element where the *quasiparticle* susceptance provides a voltage controlled inductance. Figure 6.1 shows the calculated quasiparticle conductance and susceptance at 90 GHz for a low input power (α~0.3). The conductance has a flat peak within one photon energy of the gap voltage, is small at lower voltages, and approaches the normal state conductance (R_n^{-1}) above this region. The susceptance, on the other hand, has a small positive peak one photon energy below and one photon energy above the gap voltage, and at the gap voltage exhibits a large negative peak. Thus, close to the gap voltage the quasiparticle response of a tunnel junction can be modeled as a voltage-variable susceptance, $B_Q(V_o) = -j/\omega L(V_o)$, in parallel with a constant conductance which is about $3G_n$.

In order to resonate the capacitance of the SIS element at the frequency of operation, one needs to place the mixer in rf-parallel with a tuning inductor. In this design we use a series array of four tunnel junctions as the mixing element. The inductance is provided by a separate series array of seven tunnel junctions which is referred to as the tuning array. This tuning array is independently dc-biased and is in rf-parallel with the mixing array. The junctions of the tuning array have the same current density and area (thus also resistance) as the junctions of the mixing array. In order to decrease the absorption of photons from the input signal by the tuning array, there are about twice as many tuning junctions as mixing junctions. This ensures that the dominant mixing effect is from the mixing array since the resistance of

the tuning array is higher. We do expect a division of signal power between the mixing array and the tuning array. Still, the mixer gain is improved by using the tuning array, when the tuning array is properly biased. The use of a series array for tuning adds less capacitance than a single junction.

The mixer block is the same one used for the mixing experiments reported in Chapter 4. The mixer chip is shown in Fig. 6.2 along with an electrical model of the microstrip circuitry. The signal is coupled into the mixing and tuning arrays in parallel. The on-chip filters following the mixing and tuning array are similar, except the larger contact pad for the tuning array. This is tolerable since the if signal is not used and shunted to ground eventually. DC contact to this pad is made with a pogo pin. Another difference in the two paths is that the capacitor in the bias tee of the tuning array is connected to the dewar, which is an if ground. This is necessary to avoid developing an if voltage across the tuning array. This ensures that the heterodyne detection takes place in the mixing array, and also guarantees that any tuning achieved is at the rf port and not the if port. This is a very important point since the claim of this chapter is the first utilization of the quasiparticle susceptance as a tuning element at the signal frequency. The quasiparticle susceptance is negligible at the if frequency, but the quasiparticle conductance is significant (~dI/dV). We use a capacitor to short the if signal across the tuning array. This fixes the if impedance of the tuning array at zero. Thus any changes in the tuning conditions are at the rf frequency.

The detail of the junction area and the lumped element circuit models are shown in Fig. 6.3. This is for a single junction tuned by an array of two tunnel junctions. The circuit model consists of the capacitances of the arrays, the mixing element, and the voltage dependent quasiparticle admittance of the tuning array modeled as a conductance in parallel with the susceptance.

6.3 Receiver Results:

Several methods are used to test the performance of this tuning approach and the results are compared quantitatively with the quantum theory of mixing [Tucker 1985]. As discussed in Chapter 2, the shape of the rf-induced tunneling steps depends on the amplitude of the rf signal and the admittance presented to the device by the embedding circuitry. As one changes the embedding admittance from capacitive to inductive, the shape of the individual steps becomes better defined and the dynamic resistance in the middle of the first photon step increases (i.e., the step becomes flatter). The if output resistance of the mixer is the differential resistance of the dc I-V curve in the middle of the first photon step. The input impedance of the if amplifier should match this differential resistance for best if coupling efficiency. For optimum receiver performance with a 50 ohm if amplifier input impedance, the rf conductance of the mixer needs to be within a range of values around the microstripline admittance of 20 mmhos, and the capacitive susceptance of the mixer should be resonated by the inductive embedding susceptance of the tuning array [Kerr 1993, McGrath 1988].

Experimentally obtained I-V curves with tunneling steps at 90 GHz are shown in Fig. 6.4 for two different biasing conditions for the tuning array. When the tuning array is biased at the gap voltage (point a in the inset) the dynamic resistance of the mixing array in the middle of the first photon step is a factor of two larger than for bias voltage b; this is evident in Fig. 6.4. This shows that we have altered the embedding admittance seen by the *mixing* array by changing the bias voltage of the *tuning* array.

From the shape of the tunneling steps in Fig. 6.4 we calculate the embedding admittance seen by the mixing array (Skalare). The embedding

admittance is

$$Y_{emb} = [G_t + G'] + i\,[\,\omega C_m + \omega C_t + B_t(V_o) + \delta\,]\,. \qquad 6.1$$

This includes the conductance of the tuning array G_t, the microstripline conductance G', the geometric capacitance of the mixing array C_m and the tuning array C_t [Lichtenberger note], the dc-voltage-dependent susceptance of the tuning array $B_t(V_o)$, and δ, which accounts for the susceptance of the radial stubs and other stray susceptances.

Values of B_t and G_t are obtained by fitting the I-V curves; these are given in Table I. The susceptance change between curves a and b is $\Delta B_t = 42 \pm 9$ mmhos. (The uncertainty arises from the range of embedding admittances which result in similar I-V curves). The theoretical value is ΔB_t (calc) = 49 mmhos, from Eqn. 5.16. This is in good agreement with the experimentally derived value.

Figure 6.5 shows the mixer gain g_m and receiver noise temperature T_R of this mixer at 90 GHz as a function of the dc-bias voltage of the *tuning* array. Here the if amplifier noise temperature, T_{if}, is around 8K. The negative susceptance of the tuning array increases as V_t approaches the gap voltage, where it resonates the capacitance. (The susceptance due to the capacitance is $\omega(C_m + C_t) = 40$ mmho.) Resonating this capacitance at $V_t \sim V_g$ gives the largest mixer gain and the lowest receiver noise. Above the gap voltage there is an increase in the receiver noise due to the shot noise added by the dc current in the tuning array. The results for g_m and T_R for three specific values of V_t are given in Table 6-I. The conductance G_t of the tuning array does not appear to play a major role in determining the mixer gain, as seen by comparing columns b and c of the Table.

The theoretical mixer gain was calculated for various values of V_t, using the embedding admittances inferred from the pumped I-V curves. The trends seen in Fig. 6.5 for the calculated values of g_m agree rather well with those observed experimentally, including the peak at $V_t \sim V_g$. This agreement and the agreement of the experimental value of ΔB_t with the theoretical value verify the validity of the model we have employed of a separate quasiparticle tuning element. The mixer gain is significantly improved compared to the case of no tuning junctions, listed in the last column of Table I. This confirms the success of this approach of using the quasiparticle susceptance as a voltage variable tuning element.

Figure 6.6 shows the noise temperature of this receiver configuration as a function of frequency for two bias voltages. The receiver performance is improved over the full frequency range. There is also no apparent shift in the resonant frequency. This is due to two reasons. First, since the total capacitance is not resonated by the susceptance, one would not expect to see a resonance in this frequency band. Secondly, as observed in scale model measurements, there are various series resonances associated with the impedance transformations. These are not strongly effected by the tuning array, and thus the resonant structure remains.

We observe similar results with another mixer element (Fig. 6.7). This is a device with a higher normal state resistance (R_n=115Ω), and thus a larger $\omega R_n C$ product. It also consists of a four junction array tuned by an array of seven tuning junctions. Note that in this device there is a definite improvement in receiver performance at the higher frequencies, but not in frequencies below mid-band. These characteristics are closer to what one would ideally like to observe. However due to series resonances, the resonant frequency again does not shift substantially.

In conclusion, the approach of using the quasiparticle susceptance as a tuning element is demonstrated. However, in order to achieve a substantial tuning range, one needs to place a fixed inductor in parallel to aid in resonating the geometric capacitance. Secondly, this tuning approach suffers from similar limitations as in any tuning approach, mainly the need to tune both series and parallel components of the embedding admittance. This is necessary in order to make available a larger area of the Smith chart as possible embedding admittances. One conclusion we can draw about the mixer block design is that the impedance transformers play a big role in determining tuning conditions as a function of frequency, due to their somewhat resonant structure. Scaling this design to much higher frequencies poses a machining and fabrication challange due to the small dimensions of the waveguide ridge and the thin substrate. At submillimeter wavelengths a quasioptical design using a loaded line tuning scheme has been demonstrated [Büttgenbach, 1992]. This design may be extended to utilize the reciprocity of the quasiparticle admittances of two junctions and achieve tuning over a wide band. The difference in this design from the one discussed in this chapter would be the fact that both junctions would be used for mixing. This is similar to the approach suggested by Belitsky and Tarasov (1991), but with additional tuning that would be variable.

6.4 Josephson Tuning:

An alternative tuning approach would take advantage of the reactance associated with the Josephson currents. The advantage of this approach is that it is non-dissipative. The behavior of the Josephson tunneling current is described by two equations; $I=I_c\sin\phi$ and $V=(\phi_o/2\pi)\, d\phi/dt$, where I_c is the critical current, ϕ_o the fluxon (2×10^{-7} Weber), and ϕ the phase difference in the

order parameter between the two electrodes. It is important to note that in this section V and I denote instantaneous values. For a sinusoidal voltage $V=V_\omega \cos\omega t$, we can integrate the second equation to solve for ϕ. This gives;

$$\phi=\phi'+\frac{2eV_\omega \sin\omega t}{\hbar\omega}=\phi'+2\alpha\sin\omega t \qquad 6.2$$

where ϕ' is the phase at the dc bias point, and $\alpha=eV_\omega/\hbar\omega$ is the same coefficient as defined previously for quasiparticle currents. The factor of two arises since we are considering a pair of electrons. Substituting into the first describing equation gives:

$$I=I_c \sin(\phi'+2\alpha \sin\omega t) \qquad 6.3$$

For small rf signals such that $\alpha<.2$, we can separate this expression into two parts: a dc component which designates the current bias point, and an ac component which is purely reactive.

$$I=I_o+I_\omega \sin\omega t \qquad 6.4$$

where $I_O=I_C \sin\phi'$, and $I_\omega= 2\alpha I_C \cos\phi'$.

Using the definition of an inductance, $V=LdI/dt$, we can derive an equivalent Josephson inductance:

$$L_j=\frac{V}{dI/dt}=\frac{V_\omega \cos\omega t}{\omega I_\omega \cos\omega t}=\frac{V_\omega}{\omega I_\omega} \qquad 6.5$$

We need to solve for I_ω using the expressions; $I_O=I_C \sin\phi'$, and $I_\omega= 2\alpha I_C \cos\phi'$. Using trigonometric identities we get, $I_\omega=2\alpha \sqrt{(I_c^2-I_o^2)}$. Substituting $V_\omega=\hbar\omega\alpha/e$, we obtain an expression for L_j;

$$L_j = \frac{\hbar}{2eI_c\sqrt{1-\left(I_o/I_c\right)^2}} \qquad 6.6$$

There are two important properties of this inductance to consider. One is the Josephson inductance at zero dc bias current given by $L_{jo}=\hbar/2eI_c$, which is plotted in Fig. 6.8. There is a sharp drop in this inductance as a function of the critical current. The dc bias current dependence of the normalized inductance is plotted in Fig. 6.9. We see that a 25% increase in inductance is achieved by biasing at 60% of the critical current.

We have established that the Josephson ac current at the zero voltage state is reactive and the magnitude of its inductance depends on the dc bias current. Using this inductance as a tuning element has been proposed, but never tested with success (Irwin , Kaplan, Winkler). There are three possible problems with this approach (Feldman). The most obvious one is the fact that the expression for the inductance as derived above is only valid for $\alpha<0.2$, while most quasiparticle mixers operate with $\alpha\sim1$. This would require the use of about five times as many tuning junctions in series as there are mixer junctions. This is certainly feasible, however one has to consider the series reactance added to the circuit by the interconnecting microstriplines in such a large array of junctions.

Secondly, in order to achieve inductive tuning the junctions need to operate below their plasma frequency which is set by their geometric capacitance and the zero-current Josephson inductance:

$$\omega_p = \frac{1}{\sqrt{L_{jo}C}} = \frac{1}{\sqrt{(\hbar/2eI_c)AC_s}} = \frac{1}{\sqrt{(\hbar/2eJ_c)A^2C_s}} \qquad 6.7$$

Since these junctions will need to be microfabricated along with mixer

junctions, the critical current achievable and the junction area will be decided by the present fabrication capabilities and signal coupling method. For highest tunability one would need a large J_c and a small area. With present technology, SIS junctions with good tunneling characteristics can be made as small as $1\mu m^2$ with current densities as high as $10^4 A/cm^2$. This would correspond to a plasma frequency of 350 GHz.

The third and maybe the most severe problem is intrinsic to the approach, which is the need to employ the Josephson current. It is well established that quasiparticle mixers at frequencies higher than 300GHz suffer from excess noise due to the Josephson effect. Usually a magnetic field strong enough to fully suppress the dc Josephson current is applied to minimize this noise. Otherwise the if output over the photon step is not smooth and one observes peaks at bias voltages corresponding to the Josephson frequency, $V_o = 2e/\hbar\omega_j$. This limitation prohibits the use of the Josephson inductance as a tuning element unless the Josephson tuning junctions have a smaller cross-sectional area for the magnetic field than the mixer junctions as shown below, in which case one can retain ~50% of the Josephson current in the tuning junctions while it is completely suppressed in the mixer junctions.

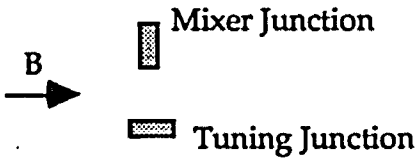

We have designed mixers based on this tuning approach, with up to three times more tuning junctions than mixer junctions in an array. These mixers were tested at 100 GHz, which is a low enough frequency such that Josephson effect noise is not a major problem. 100 GHz is also below the

plasma frequency assuming a specific capacitance of 45 fF/μm^2. We did not observe a change in the shape of the photon assisted tunneling steps even for relatively small input powers. The if output of the mixer became noisy when the tuning junctions were biased at the zero voltage state. This is due to fact that the Josephson inductance is highly nonlinear, and introduces large noise sidebands as discussed above. Using resistively shunted junctions could solve the problems of unstable operation and sideband generation but might introduce losses [Schoelkopf, 1993].

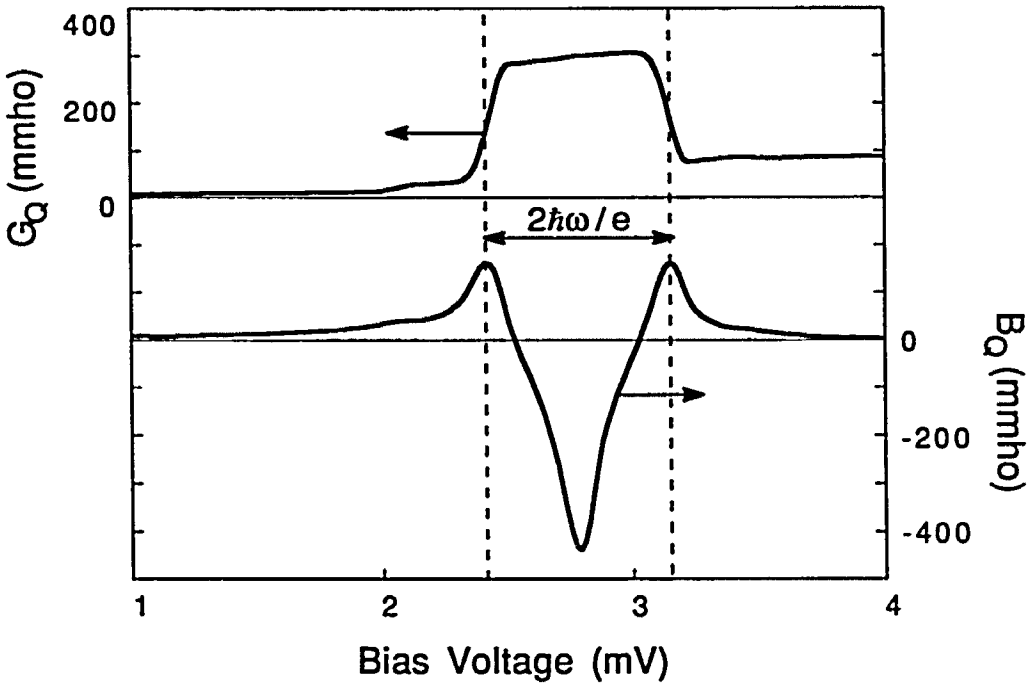

Fig. 6.1: The calculated quasiparticle conductance and susceptance (bottom) for a small input power at 90 GHz. The dotted lines show the voltages corresponding to a photon energy below and above the gap voltage.

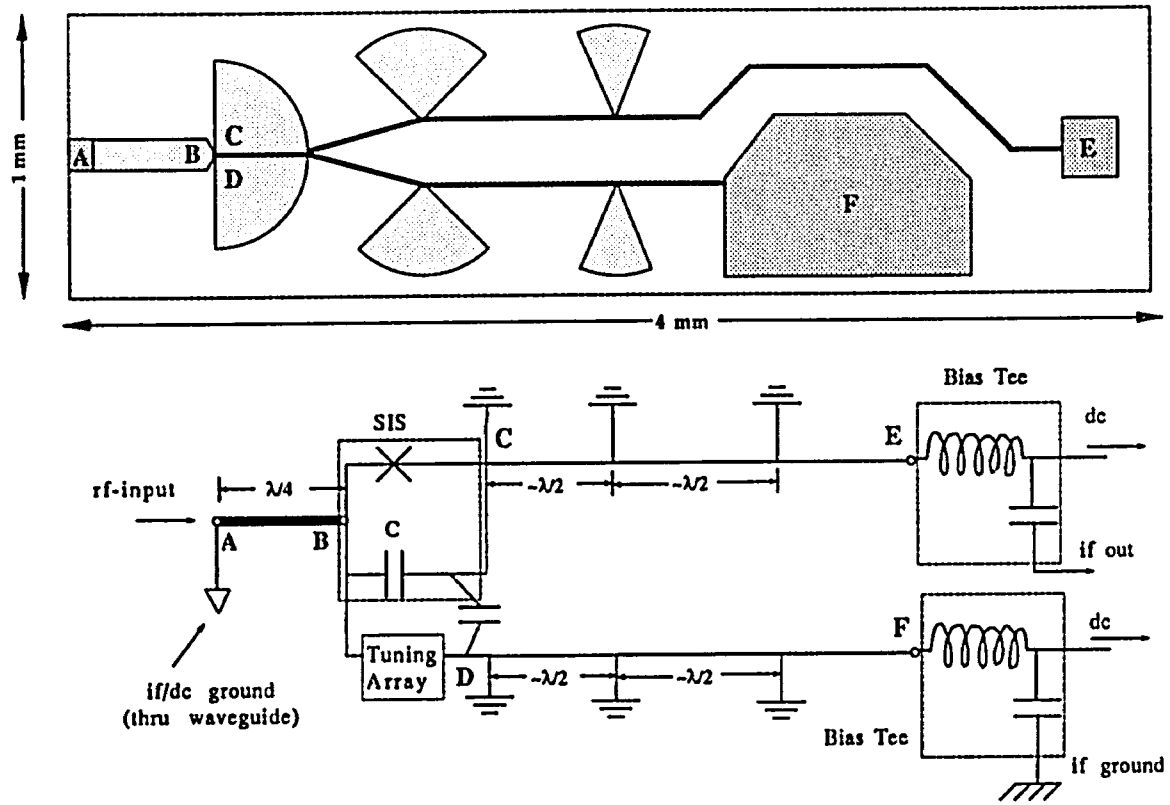

Fig. 6.2: The quasiparticle tuned mixer chip (top) and the lumped element equivalent circuit (bottom). The test signal along with the local oscillator signal is fed into the input microstrip (A). Radial stubs provide two dc-isolated rf grounds near locations C and D. The sections connecting C to E and D to F are rf filter sections. The if and dc signals are separated via a bias tee for the mixing array connected to point E. The if port of the tuning array is shunted to ground with a capacitor using a similar bias tee.

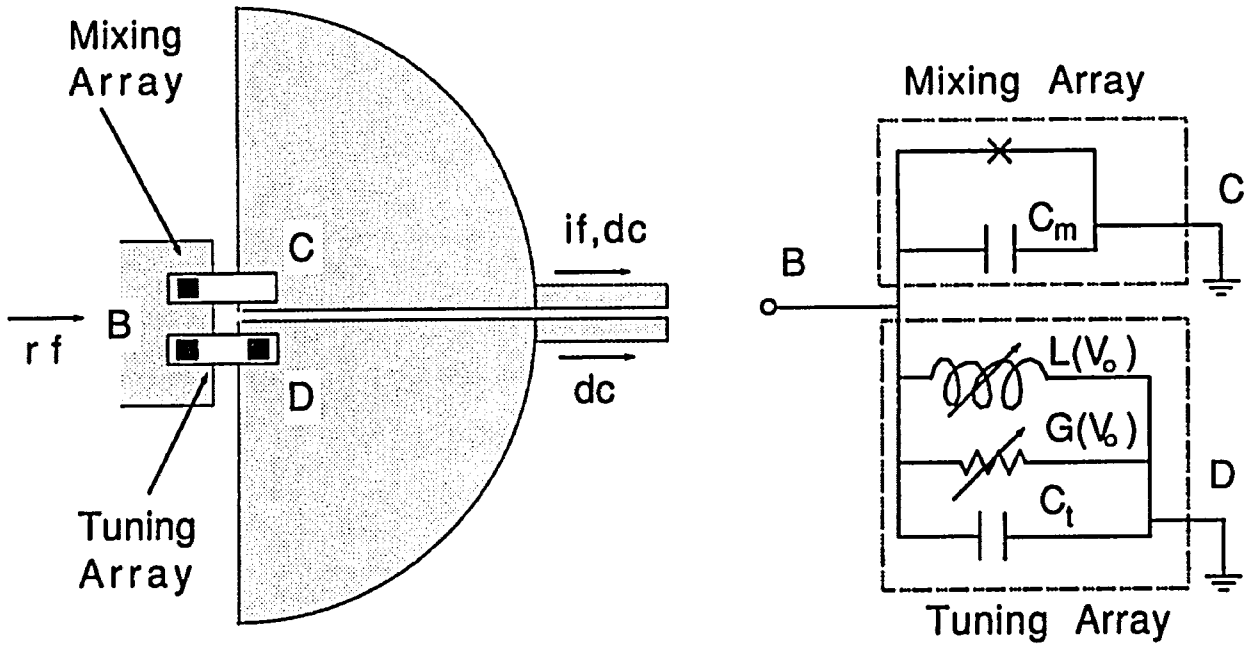

Fig. 6.3: Detail of the junction area on the chip (left) and the rf equivalent circuit (right). Not all junctions are shown. The test signal along with the local oscillator signal is fed into the input microstrip (B). Both arrays are terminated in 90° radial stubs providing two dc-isolated rf grounds near locations C and D, where the junctions connect. The if and dc signals are extracted at C for the mixer while the tuning array is biased through D. In the actual experiment we have used a four junction array for mixing and a seven junction array for tuning.

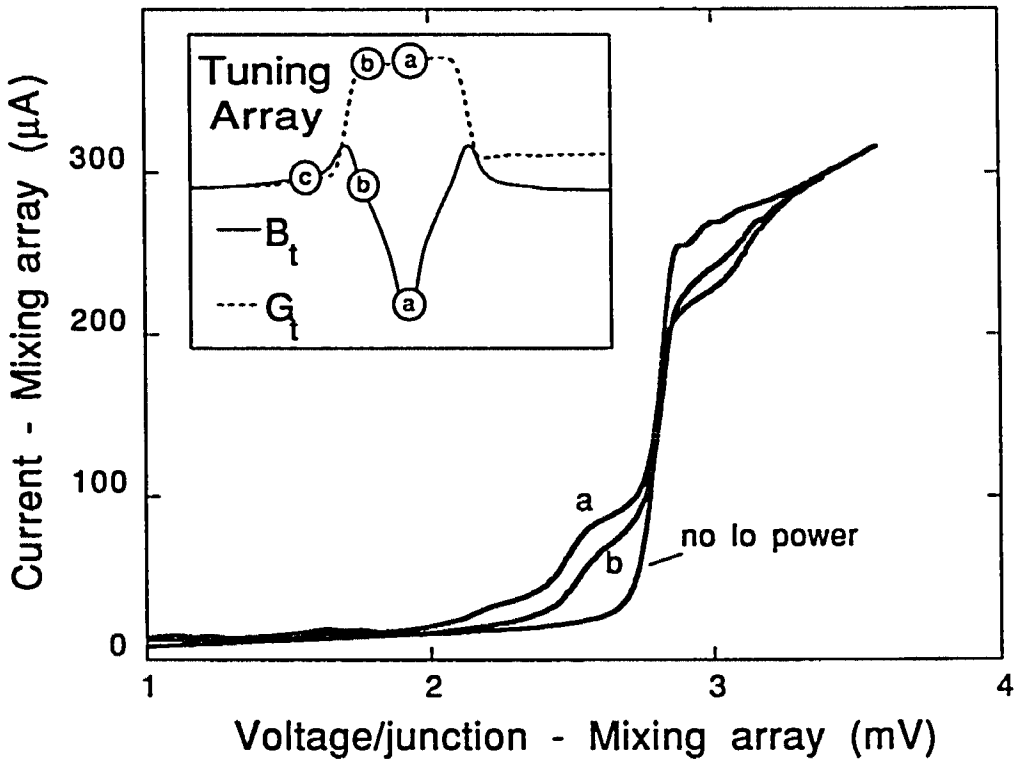

Fig. 6.4 : Measured I-V curves of the mixing array for two different bias voltages on the tuning array. Curves a and b are with lo power applied; curve c has no lo power. The inset shows the conductance and the susceptance of the tuning array at bias voltages a, b, and c on the tuning array.

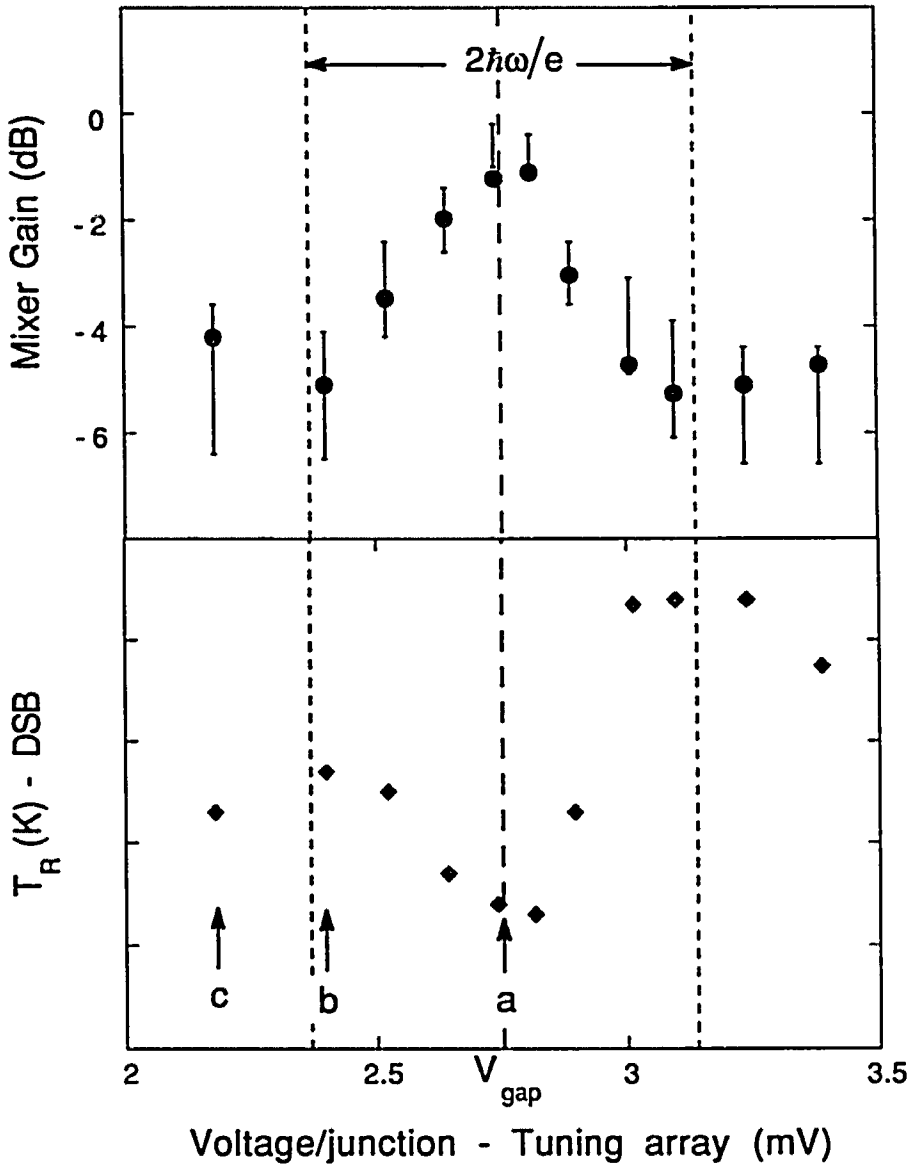

Fig. 6.5: Experimental mixer gain (top) and DSB receiver noise temperature (bottom) at 90 GHz as a function of the tuning array bias voltage. The bars indicate the range of theoretical mixer gains for the embedding admittances derived from the measured I-V curves.

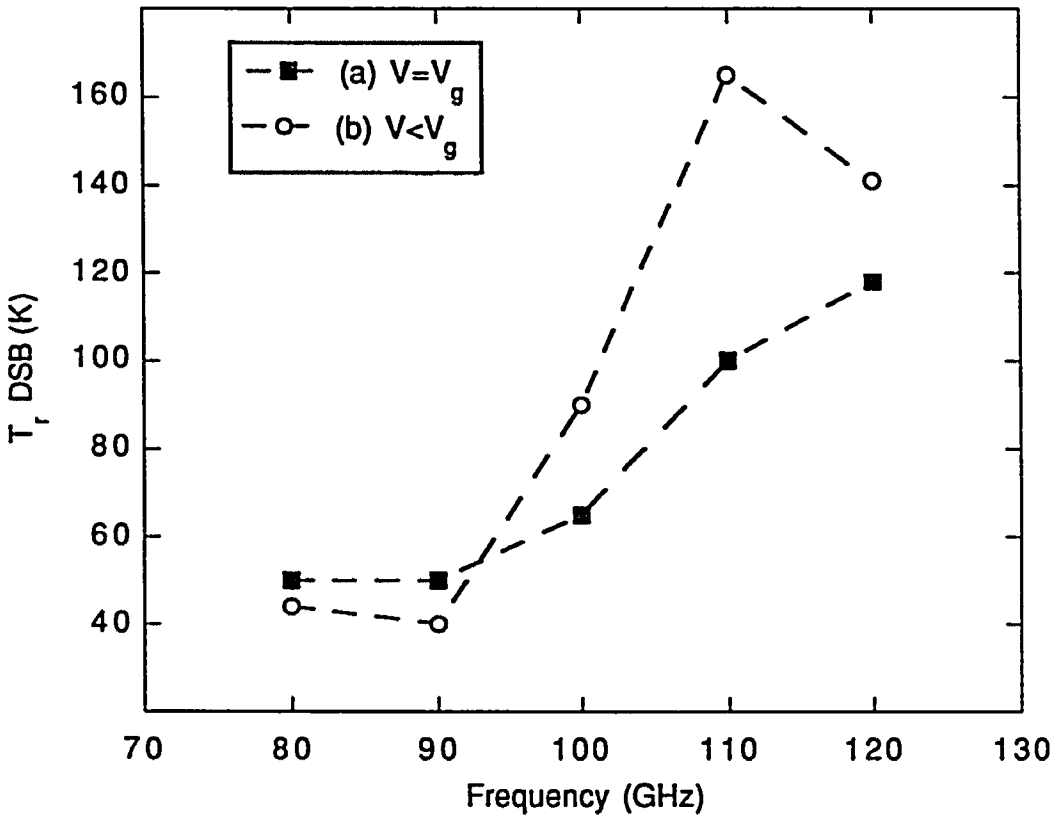

Fig. 6.6: The DSB receiver noise temperature for the device reported as a function of frequency for bias voltages a and b. These voltages correspond to the inset of Figure 6.4.

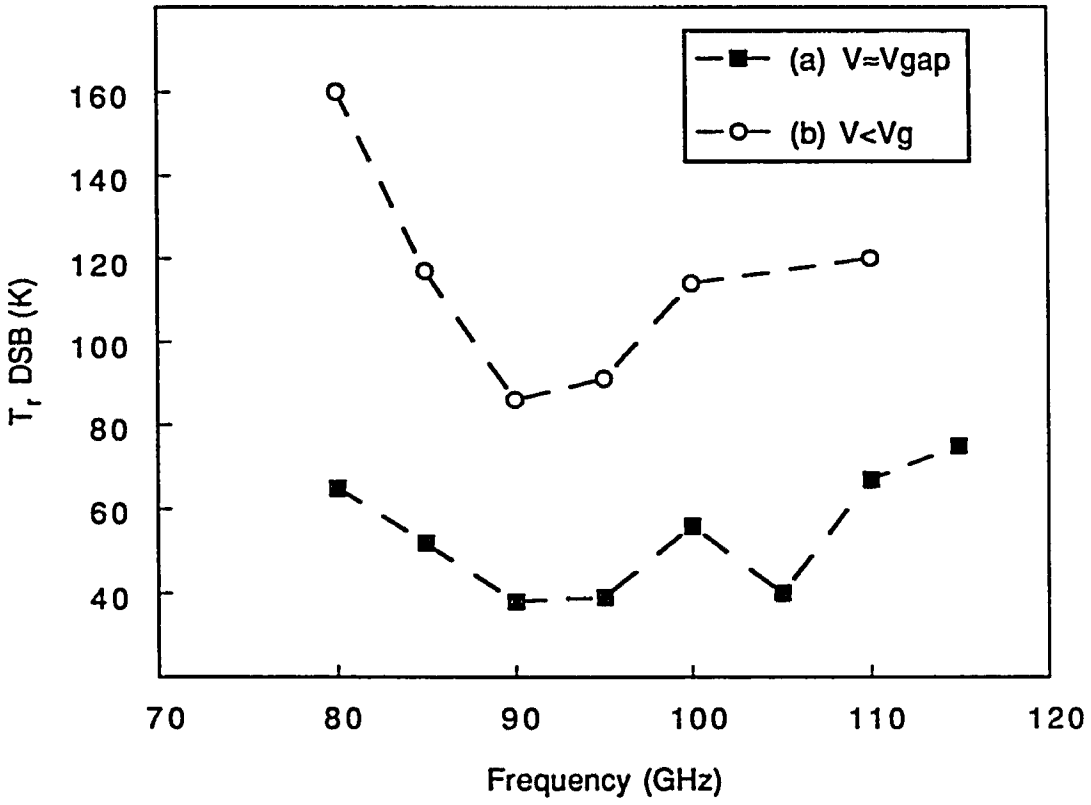

Fig. 6.7: The DSB receiver noise temperature for a 115Ω device as a function of frequency for similar bias voltages on the tuning array.

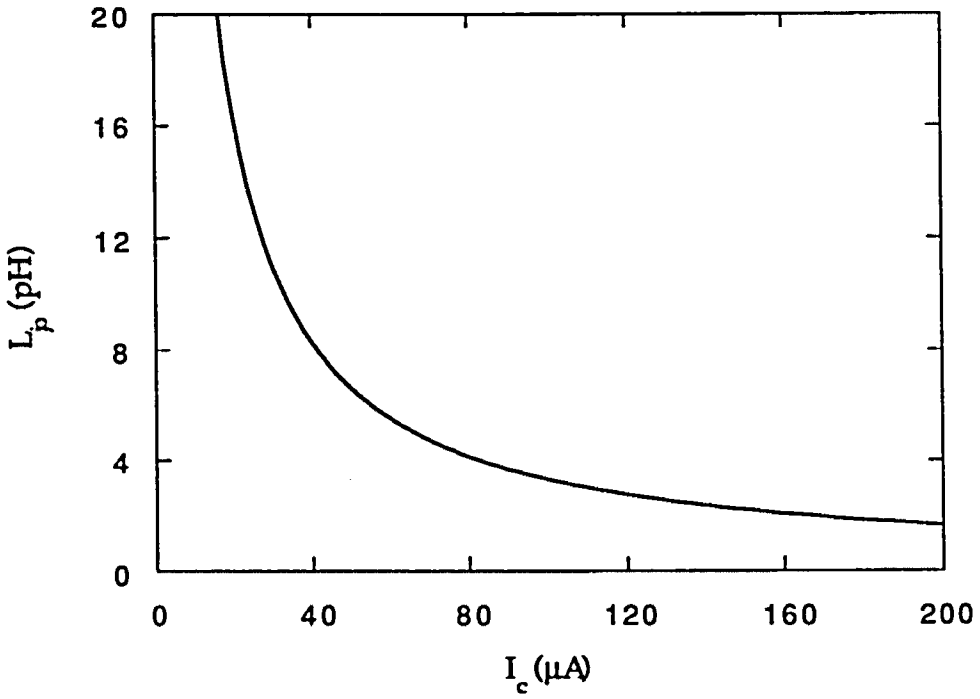

Fig. 6.8: The zero current Josephson inductance as a function of the critical current of the tunnel junction.

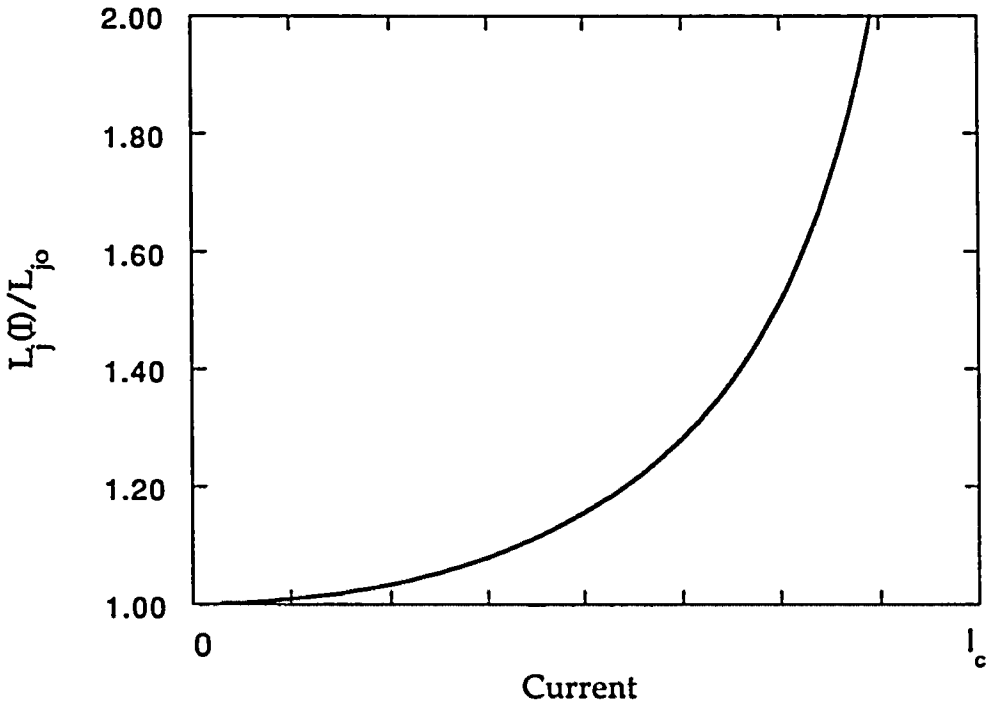

Fig. 6.9: The Josephson inductance normalized to the zero current inductance as a function of the dc bias current.

VII - Superconducting Phase Shifter

In this chapter, I propose using the voltage dependent quasiparticle admittance of the superconducting tunnel junction as a voltage controlled phase shifter. I present three configurations which would provide voltage-variable on-chip phase shifting. The theoretical upper frequency limit of these elements is determined at least by the gap frequency of the superconductor (0.7 THz for Nb), and is actually lower due to electromagnetic constraints. Such circuit elements could be utilized in superconducting systems in telecommunications, phased-array radar antennas, oscillators and in superconducting receivers. However before any of these elements are implemented into a system, more detailed calculations should be carried out. What is presented here is the basic approach.

7.1 Motivation

A communication system based on superconducting electronics is presently feasible, as most of the essential components of such a system have been demonstrated [Van Duzer,1989]. A variable phase shifter is an essential component for such a system, as it can provide variable time delay for signal processing and a phase delay for electronic scanning antenna arrays.

Efforts to realize a tunable superconducting phase shifter have yielded some success. One of these approaches is based on inductance modulation of a superconducting microstripline by excess quasiparticle injection [Track,1991]. The dc current increases the magnetic penetration depth, thus decreasing the phase velocity and increasing the phase delay. This approach has been tested at 100 GHz using interferometric techniques, and some phase velocity modulation has been observed. However in order to achieve substantial

tunability a thin dielectric is needed which in return results in high conductor losses and difficulty in signal coupling [Track,1991]. A second group observed a small change in the resonant frequency of a superconducting microstripline circuit also by modulating the kinetic inductance [Beasley,1992; Anlage,1989]. The attempts to modulate the inductance of a superconducting stripline by heating and also by optical irradiation yield limited tunability as well. These two methods are limited in response time to the phonon lifetimes which would be close to a microsecond for a usable microstrip geometry [Track,1991].

All of the approaches discussed above drive the phase shifting device close to the superconducting phase transition by operating very close to the critical temperature or the critical current. This results in premature breakdown at the edges of the microstrip, and also in increased signal attenuation as the phase is varied. More recently there has been a demonstration of a distributed Josephson inductance phase shifter (DJI), which consists of a series array of 1600 superconducting quantum interference devices (SQUID's), coupled to a superconducting transmission line [Durand, 1992]. By changing the dc current through the SQUID array, the phase velocity of the signal is varied. This results in a maximum phase shift of 60° at 10 GHz for an rf power of -40dBm. However due to the highly non-linear nature of the Josephson effect, such devices are susceptible to harmonic distortion effects.

In this chapter the application I will try to gear towards is a w-band phased radar array. System requirements for such an application include a 180° or a 360° phase shifter with 4-bit resolution in phase, that can handle rf signals around -20dBm. Another requirement is that harmonic distortion should be more than 50 dB down from the amplitude of the signal frequency

[Ralston]. The device concepts presented here approach the dynamic range and the phase shift resolution requirements. Harmonic distortion effects are reduced substantially compared to a Josephson effect device. To quantify this statement calculations of the local oscillator waveform are needed in a five or eight port model, to include higher harmonics.

I propose three device concepts using SIS (superconductor-insulator-superconductor) tunnel junctions as voltage variable phase shifters. The first device is an array of tunnel junctions, where the *quasiparticle susceptance* provides a voltage controlled inductance. Secondly I propose using the *quasiparticle conductance* as a low-loss, voltage controlled rf switch. With this switch one can construct a variable phase shifter in two different configurations.

7.2 Loaded Line Phase Shifter

I propose using the strong variation in the quasiparticle admittance (shown in Fig. 7.1) as a voltage variable phase delay element in the reflection mode as in Fig. 7.2. The reflection coefficient in this configuration is given by:

$$\Gamma = \rho e^{i\theta} = \frac{Y_o - Y_L}{Y_o + Y_L} \quad , \qquad 7.1$$

where ρ is the amplitude and θ the phase of the reflection coefficient, Y_0 is the line admittance, and Y_L is the admittance of the tunnel junction. Assuming that the junctions geometric capacitance is resonated by an integrated tuning inductor, the junction admittance is the quasiparticle admittance given by:

$$Y_1(V_o, V_\omega) = G_Q(V_o, V_\omega) + iB_Q(V_o, V_\omega). \qquad 7.2$$

This equivalence was shown to hold for small and large amplitude rf input power levels in the previous two chapters. There we showed that the tunnel junction can be accurately modeled as a lumped circuit element, where the values of the lumped elements are determined by the incident power level, the frequency, and the bias voltage. In order to gain an understanding of the device concept, I will discuss the parameters for a fixed frequency of 90 GHz. Both the conductance and susceptance show approximately a 1/f fall off as a function of frequency. This poses a severe limit for using the concept at high frequencies. As will be shown below, 90 GHz is far enough from the gap frequency of the tunnel junction for this application. Here the range of phase shifts available at this frequency and the dynamic range are discussed.

The calculated reflection coefficient as a function of bias voltage for a typical tunnel junction with a normal state resistance of 50 ohms coupled to a 50 ohm microstripline is shown in Fig. 7.3. This is calculated at 90 GHz for an available input power of 2 pW. Note that between 2 mV and 2.6 mV the amplitude of the reflection coefficient does not change by more than ± 1 dB, while the phase changes by 140°. This phase is a continuous function of the dc bias voltage. This demonstrates that even though the tunnel junction is a dissipative circuit element, for certain embedding circuitry a substantial phase shift can be obtained as a function of bias voltage without a large loss of rf power.

The dynamic range of a phase shifter is of practical importance. For an equivalent array of n tunnel junctions, the relevant power level increases as n^2 when the array normal state resistance is the same as that of a single junction [Feldman 1983]. But the junctions need to be in close proximity relative to the wavelength of the signal in the microstrip. For a practical circuit at 100 GHz the wavelength is about a third of the free space value of 3

mm. Thus the junctions should occupy a length shorter than about 100 μm. The series inductance due to the length of the microstrip connecting the tunnel junctions adds additional admittance.

If we use the design arguments given above, we find that, for a practical design, the limit on the number of junctions that can be placed in series is about 12. This corresponds to a 22 dB improvement in power handling. In order to evaluate the dynamic range in power, I will consider the relative attenuation, γ, and phase shift, $\Delta\theta$, between two dc bias points:

$$\gamma = 10\log\left(\frac{\rho_1}{\rho_2}\right)$$

$$\Delta\theta = \theta_1 - \theta_2 \qquad 7.3$$

Here the subscripts denote the bias voltages. These quantities are plotted in Fig. 7.4 for an array of 12 tunnel junctions, for bias voltages V_1=2.0 mV/junction and V_2=2.8 mV/junction. Note that for an available rf power of -40 dBm, the available phase shift decreases only by ~ 20°, while the relative attenuation changes by 1 dB.

This phase shifter would not require very high quality tunnel junctions, as long as the voltage rise is narrower than the width of a photon step, i.e. $e\Delta V << \hbar\omega$. This is required in order to have a sizable quasiparticle susceptance [Tucker, 1985]. Most trilayer tunnel junctions with intermediate current densities ($10{,}000 > J_c > 1000$) meet this criterion.

7.3 The Quasiparticle Switch

There are various signal processing functions that can be performed by switching a signal path from a high impedance to a low impedance state. Semiconductor diodes have been employed for such functions in microwave

circuits [Dunn, 1989]. I propose to use the quasiparticle admittance of a superconducting tunnel junction as an equivalent of the semiconductor switching diode for superconductive electronics. In order to employ the tunnel junction as a two-state, high frequency switch, I define the desired junction impedance to be low in the 'on' state and high in the 'off' state. For simplicity, I again assume that the capacitance of the junction is resonated at the frequency of operation.

The change in impedance can be achieved by voltage biasing the tunnel junction at bias point (a) for the 'off' state and bias point (b) for the 'on' state, as shown in Fig. 7.1. For a small input power, the conductance at bias point (a) is equal to the sub-gap conductance (G_{sg}), while the conductance at bias point (b) is about three times the normal state conductance of the tunnel junction (G_n). The susceptance is negligible for both bias points. The performance of the switch depends on the ratio of the conductances. Tunnel junctions with conductance ratios of G_n/G_{sg} ~ 20-1000 have been obtained [Lichtenberger,1991 ; Worsham, 1991]. This ratio usually gets smaller as the current density of the tunnel junctions is increased, it is also a function of the incident rf power.

The optimum normal state resistance of the tunnel junction for minimum total attenuation is given by [Hines]:

$$Z_o = \sqrt{R_n/G_{sg}} \qquad 7.4$$

where Z_o is the real impedance of the transmission line to be switched. At 100 GHz a high quality tunnel junction can be used in a 50 Ω transmission line with less than a 1 dB insertion loss in the 'on' state and achieve 15 dB isolation in the 'off' state. This can be compared to a typical semiconductor

switch; FET's have achieved an insertion loss of ~ 2 dB in the 'on' state and ~ 17 dB isolation in the 'off' state at 44 GHz when their capacitance is resonated with a tuning inductor [Dunn,1989]. FET's are three terminal devices, and thus easier to implement in rf circuits. Since tunnel junctions are two terminal devices, the rf signal and the dc control signal (current or voltage) need to be filtered properly in the circuit. As shown in previous chapters, we have successfully demonstrated a rf coupling scheme using radial stubs to isolate the rf signals from the dc biasing leads. Other groups have also used radial stubs [Zmuidzinas, 1993], and other on chip filtering techniques [Xizhi,1985; Kerr] successfully.

7.4 Switched Line Phase Shifter:

Using the single pole single throw (SPST) switch described above, one can construct a single pole double throw switch or a variable phase shifter. One possible phase shifter would consist of a transmission line with a number of switches along its length which are connected to rf shorts (Fig. 7.5a). The radial stubs provide rf shorts at their apex, while the dc bias is provided via the high impedance microstriplines connected to the radial stubs. By placing one of these switches into the 'on' (low impedance) state while all other switches are 'off' (high impedance), the input signal can be shorted to ground at a given location. The location of this short circuit determines the phase of the signal at the input/output port. This is analogous to a variable backshort in a waveguide, and can also be used as a variable tuner. The circuit layout is similar to a recent design which was used to measure the VSWR along a superconducting transmission line [Smith, 1991].

With this circuit one can obtain a relatively large phase shift. The

resolution (or the number of bits) depends on the number of switches or junctions used. The reflection losses (P_{ref}/P_{in}) due to each junction in the 'off' state and the junction in the 'on' state need to be considered since the switches are not ideal. The phase shift and the reflection loss of a 2-bit, 180° phase shifter at 100 GHz is shown in Fig. 7.6 for different quality tunnel junctions.

Another switched-line phase shifter would guide the input signal through one of a possible number of transmission lines, each with a different electrical length (Fig. 7.5b). This approach has been demonstrated in semiconductor circuits, where individual FET's are used as switches [Dunn,1989; Rascoe,1989]. The limiting factors would be the same as for the design above, i.e. the conductance ratio would limit the number of paths that can be placed in parallel. For example, such a device with a 1-bit resolution would cause a 1.5 dB insertion loss for $G_n/G_{sg} = 20$, and a 0.5 dB insertion loss for $G_n/G_{sg} = 200$. It is also feasible to design a hybrid superconducting phase shifter with a switched line, to provide large nominal phase changes, terminated in a loaded line for finer and continuous variation of the phase. The far-field pattern of an antenna utilizing such phase shifters would depend strongly on the relative attenuation of the signal in different channels for different phase shifts. For some applications, a far-field pattern with acceptable gain and relatively small sidelobes might be obtainable even with the difference in attenuation as large as 5 dB between channels [Rascoe, 1989].

7.5 Design Issues and Limitations

The dependence of the quasiparticle conductance and susceptance on the signal frequency is shown in Fig. 7.7. Below ~20 GHz the loaded line approach is harder to utilize since the quasiparticle susceptance compared to

the conductance is not significant at these frequencies. The switched line would work well, as the conductance ratio, G_Q/G_{sg}, is larger.

At the gap frequency the susceptance approaches $-G_n$, while the conductance approaches the normal state conductance, G_n. Still, around zero bias voltage, there is variation in the susceptance and the conductance up to twice the gap frequency (not plotted here). This is an intrinsic upper frequency limit for the tunnel junction. A practical limit is due to the Josephson effect, which might interfere when the tunnel junction is biased close to the zero voltage state. We may then conclude that above $f/f_{gap} \sim 0.7$, these devices would not be effective in providing a large variation in phase.

The integration of tuning structures poses a difficulty in design. However, there have been numerous successful demonstrations of integrated tuning structures for superconducting circuits at these frequencies [Tucker 1985, Winkler 1991]. The requirements for the quality of the tunnel junctions depend on the application. For the loaded line, the requirements are the same as for quasiparticle mixers; one needs higher current density tunnel junctions at high frequencies with the proper normal state conductance. The switched line requires a low sub-gap leakage current, which is usually large for high current density junctions. The circuits proposed here require good quasiparticle tunneling characteristics. This prohibits the use of high temperature superconductors for this application, at least in the near future.

The switching time for a tunnel junction from one voltage state to another is limited by the quasiparticle response time. The quasiparticle response function, I_{qp0}, in time domain is plotted in Figure 7.8. This is the response of the quasiparticle currents to a voltage pulse at t=0 ignoring the geometric capacitance. This is an ideal tunnel junction biased at zero volts. There are two important features in this response function. First, the current

initially rises almost linearly. The time delay of this rise is on the order of $3\hbar/2\Delta$(0.75 psec. for Nb). After the rise the current oscillates at the gap frequency while settling to its final value. This time delay and the oscillations are due to the sharp onset of tunneling at the gap voltage, and also due to the singularity in the imaginary response at the gap voltage. This singularity causes the current to oscillate. The shape of this response function depends on the bias voltage and the embedding environment of the tunnel junction.

In the loaded line shifters, where I propose to utilize the susceptance, the response time would depend on the initial and final bias voltages. This is because the junctions real and imaginary response functions are voltage dependent. Figure 7.9 shows the conductance and susceptance as a function of frequency for two different bias voltages. Note that the sharp onset of the conductance along with the peak in susceptance shifts in *frequency* as the bias *voltage* is changed. This implies that the response time of the quasiparticles should be different for the two bias voltages. Recently the time domain response of a tunnel junction has been measured [Verghese,1993]. Preliminary results confirm the theory, and imply that for the frequencies considered here, the switching should occur within a few cycles of the rf signal.

The implementation of any of these concepts in an application will first require a full eight port analysis of the rf admittance of the tunnel junction. This will determine the amount of the distortion on the reflected or transmitted signal due to higher harmonics. An error analysis is also necessary to evaluate the tolerances of the output phase to variations in the rf power and dc bias control. The calculations done in this chapter are not sufficient in establishing the utility of the concept for a specific application.

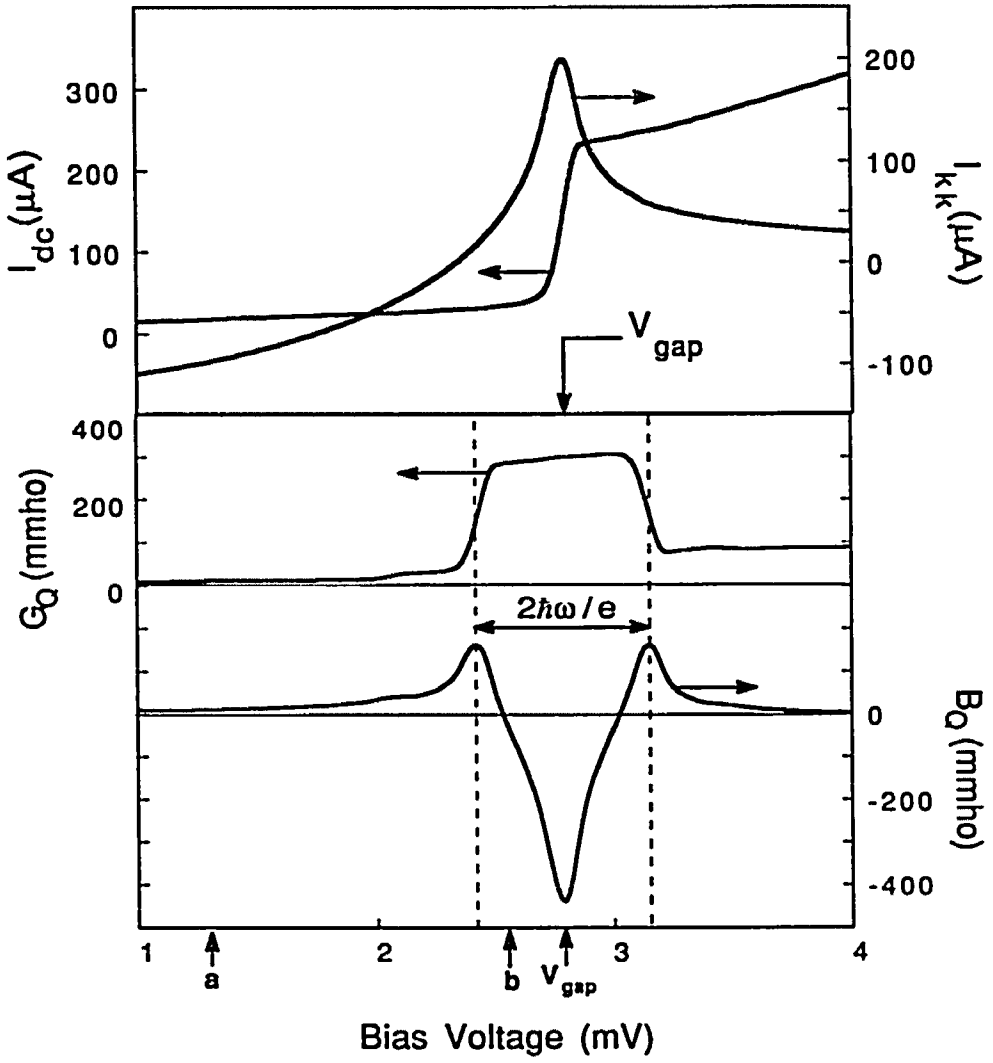

Fig. 7.1: Measured dc I-V curve of a Nb/AlO_x/Nb tunnel junction and its Kramers-Kronig transform (top). The calculated quasiparticle conductance and susceptance (bottom) for a small input power at 90 GHz. The dotted lines show the voltages corresponding to a photon energy below and above the gap voltage. The arrows refer to bias voltages mentioned in the text.

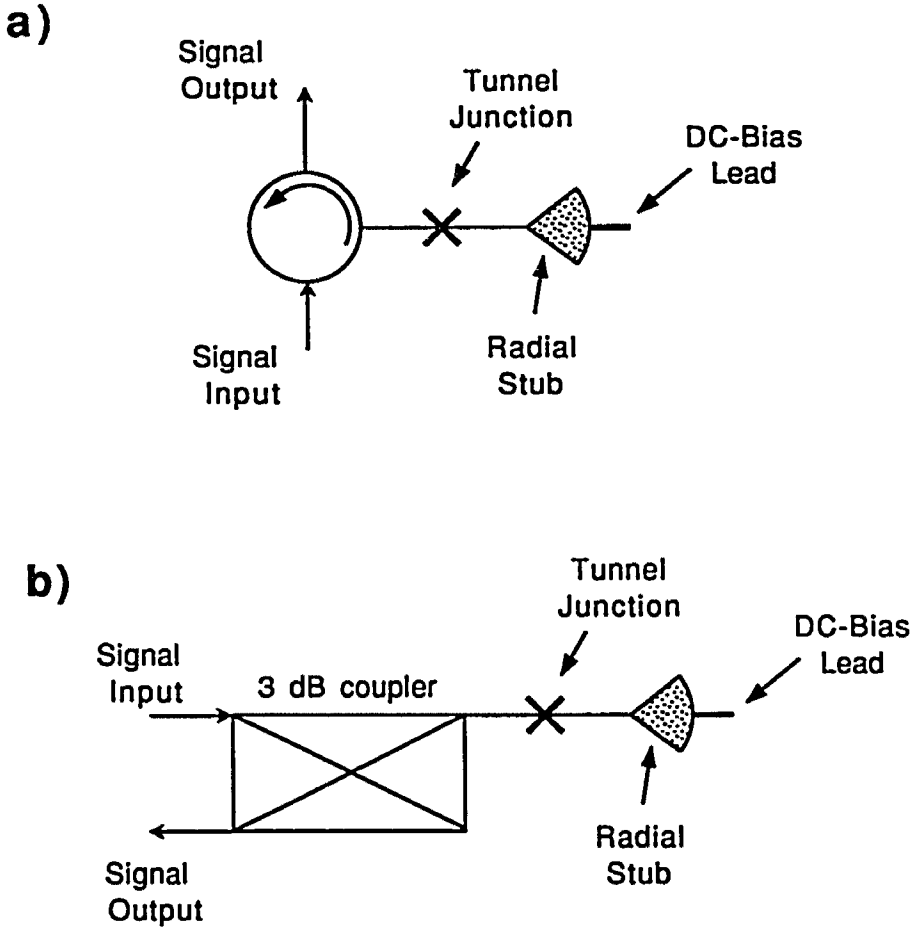

Fig. 7.2 : Two types of reflection mode, loaded-line phase shifters, where tunnel junctions are used as variable terminations. Device a (top) uses a circulator to bounce off the signal from the tunnel junction. Device b (bottom) couples the signal to the junction via a 3-dB coupler, and the reflected signal is phase shifted depending on the bias voltage of the junction.

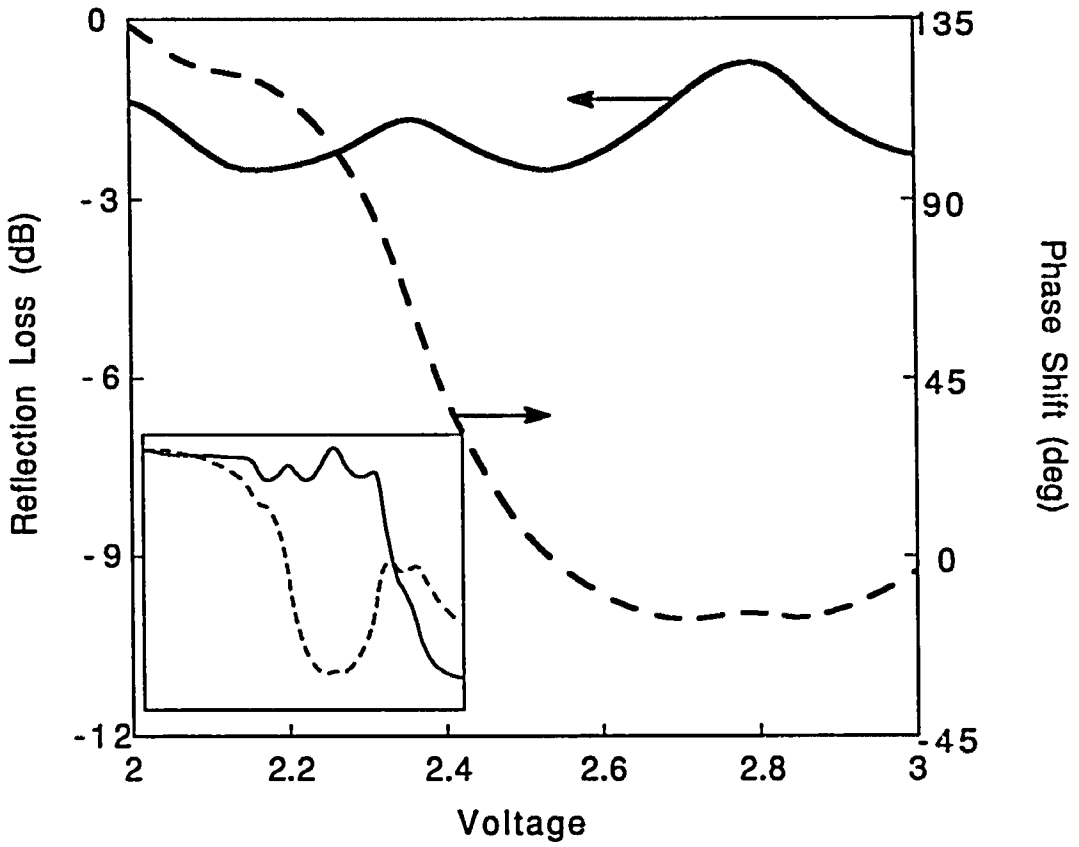

Fig. 7.3: The calculated reflection coefficient as a function of the dc bias voltage for a tunnel junction with $R_n = 50\ \Omega$. This voltage range would be usable for the loaded-line phase shifter. The inset shows the dependence between zero and five millivolts.

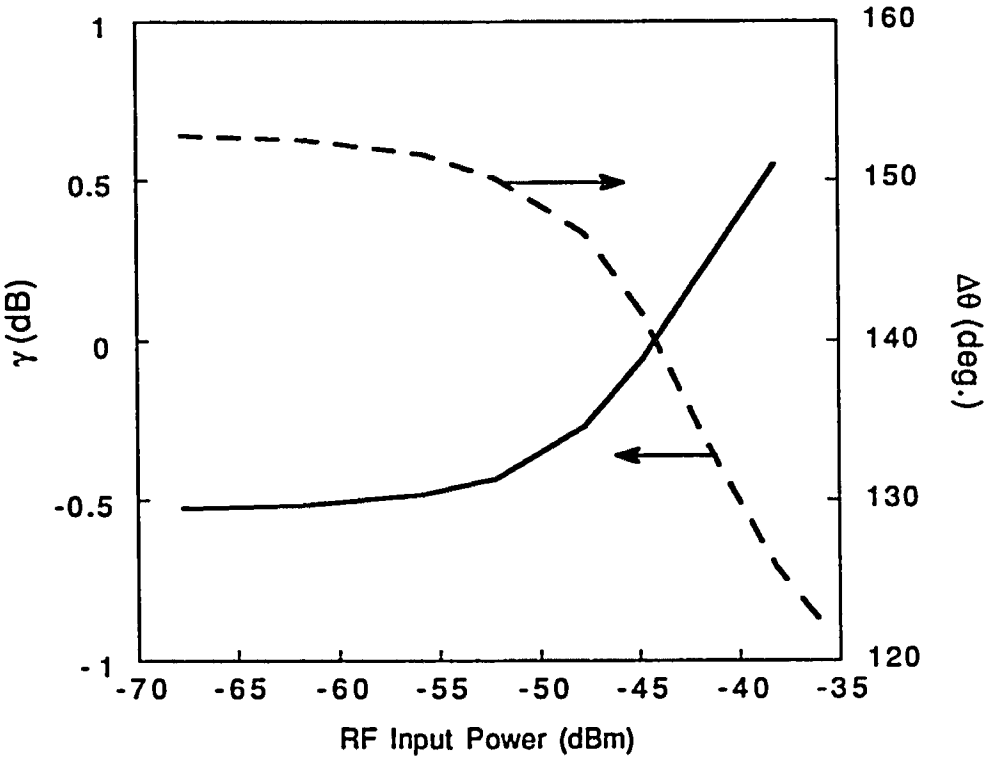

Fig. 7.4: The relative attenuation, γ, and phase shift, $\Delta\theta$, between two dc bias points as a function of input signal power. This is calculated for a 12 junction array at 90 GHz for dc bias voltages of $V_1 = 2$ mV / junction, and $V_2 = 2.8$ mV / junction.

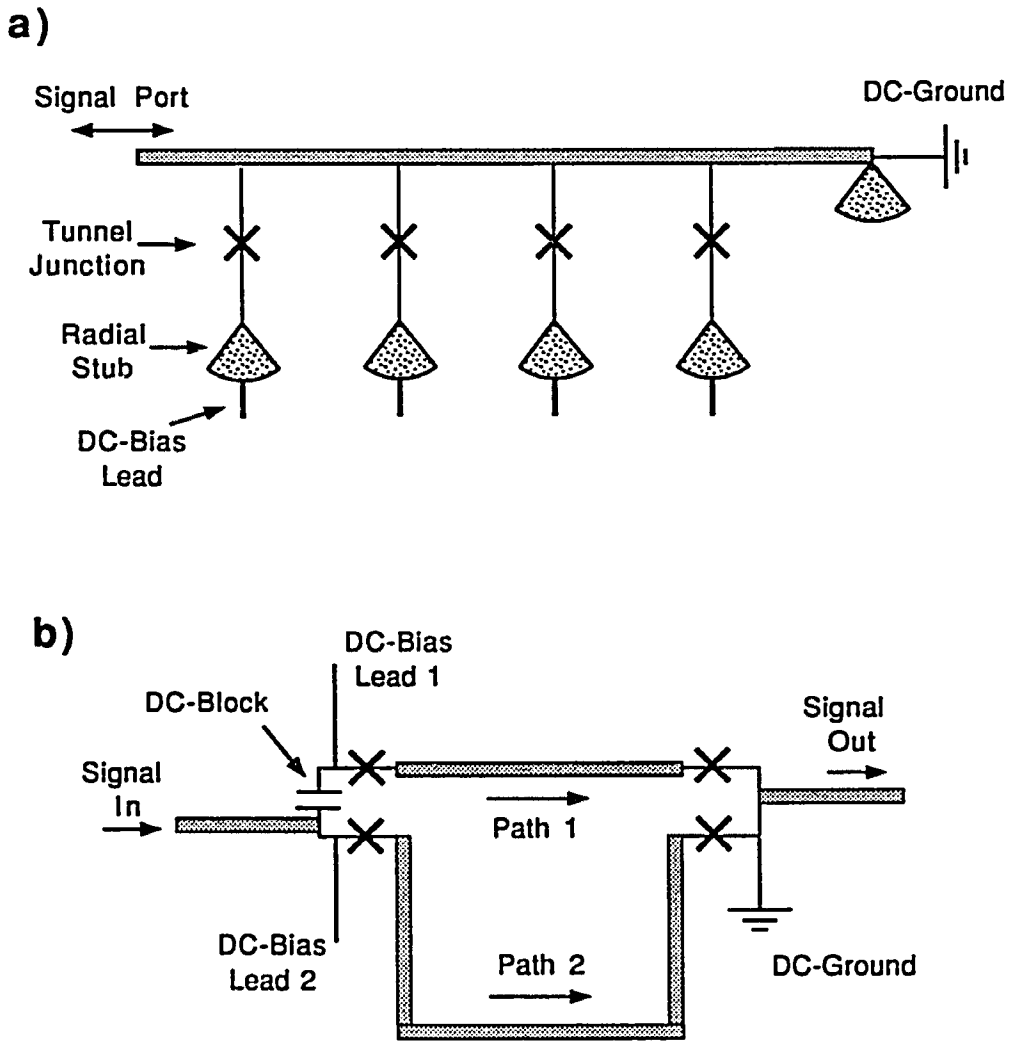

Fig. 7.5 : Two switched-line phase shifters, where tunnel junctions are used as rf switches: a) Device a (top) provides a variable backshort for the input signal, thus varying the phase at the input port. b) In device b (bottom) the phase of the transmitted signal at the output depends on the low-impedance path determined by the dc voltage on the junctions.

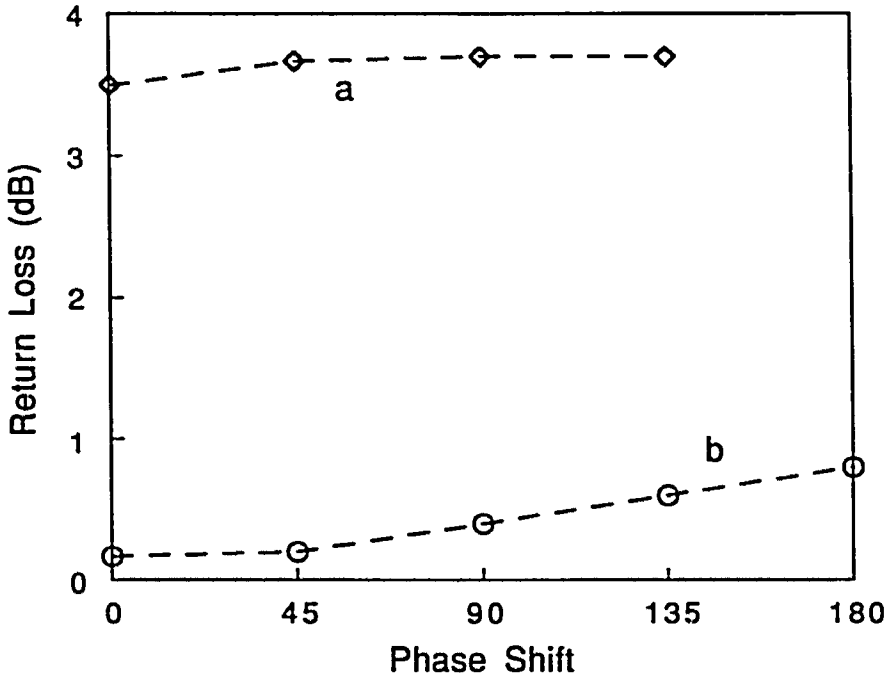

Fig. 7.6: The calculated return loss for the switched-line phase shifter shown in Fig. 6a. The loss and the phase shift is plotted for three devices: a) G_n/G_{sg}=30, b) G_n/G_{sg}=1000. We see that for a typical device (G_n/G_{sg}=30), a relatively constant attenuation can be obtained (curve a). With higher quality tunnel junctions the losses can be reduced to less than 1 dB (curve b).

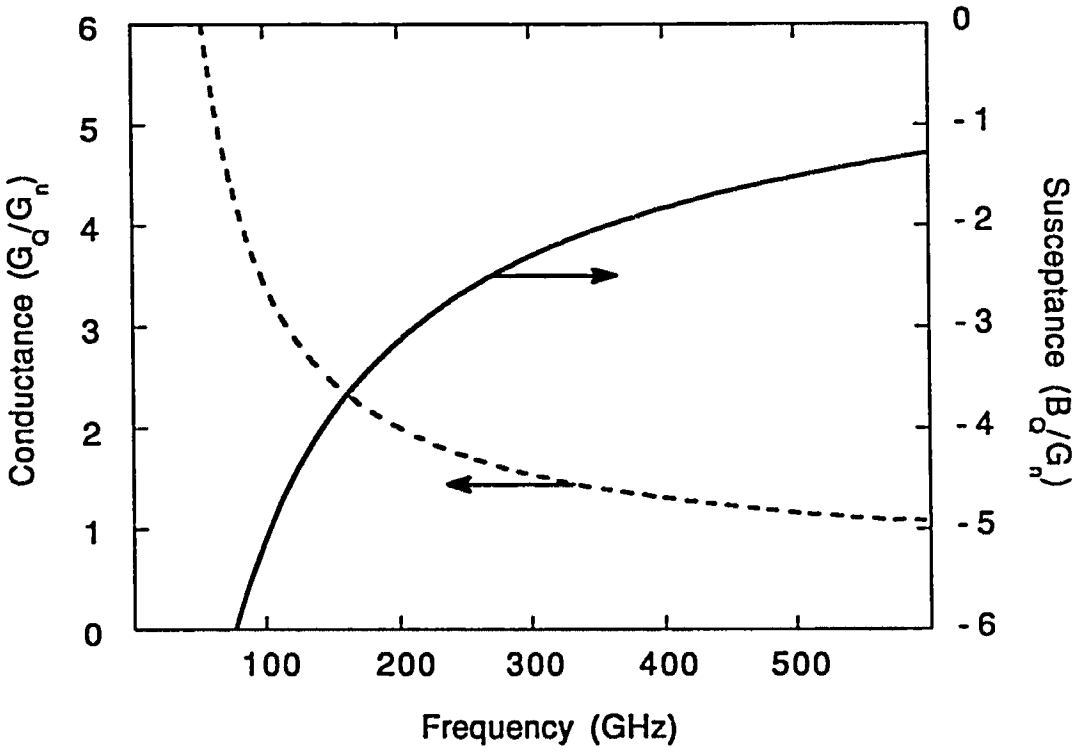

Fig. 7.7: The calculated dependence of the quasiparticle conductance and susceptance on frequency. This is for an ideal (BCS) Niobium tunnel junction, dc biased at the gap voltage.

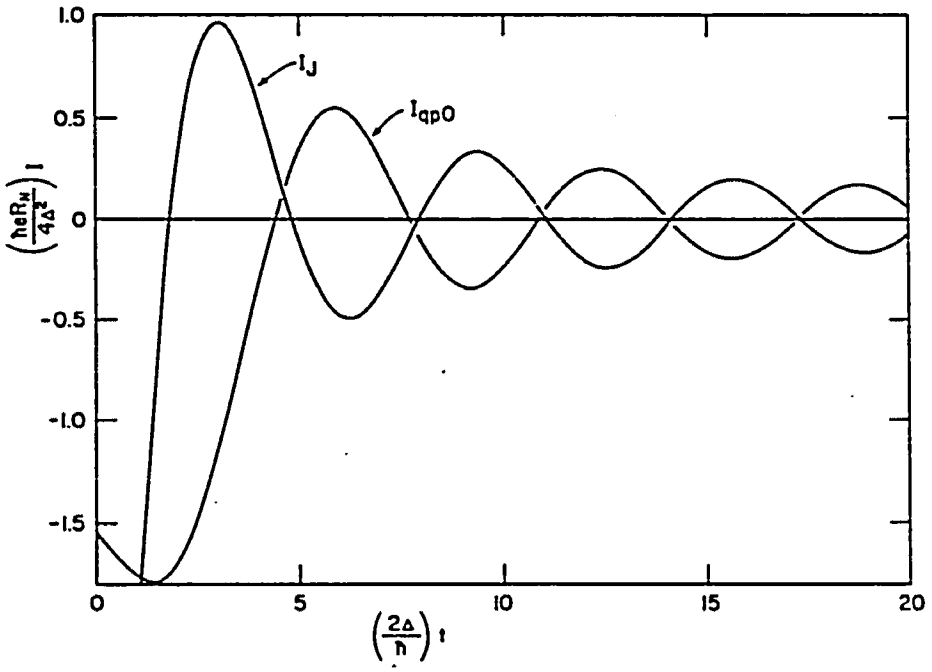

Fig. 7.8: Normalized theoretical response function of a supreconducting tunnel junction in the time domain. This is for an ideal (BCS) tunnel junction, dc biased at zero volts. I_J is the Cooper pair response function, while I_{qp0} is the quasiparticle response. (Reproduced from McDonald, 1980)

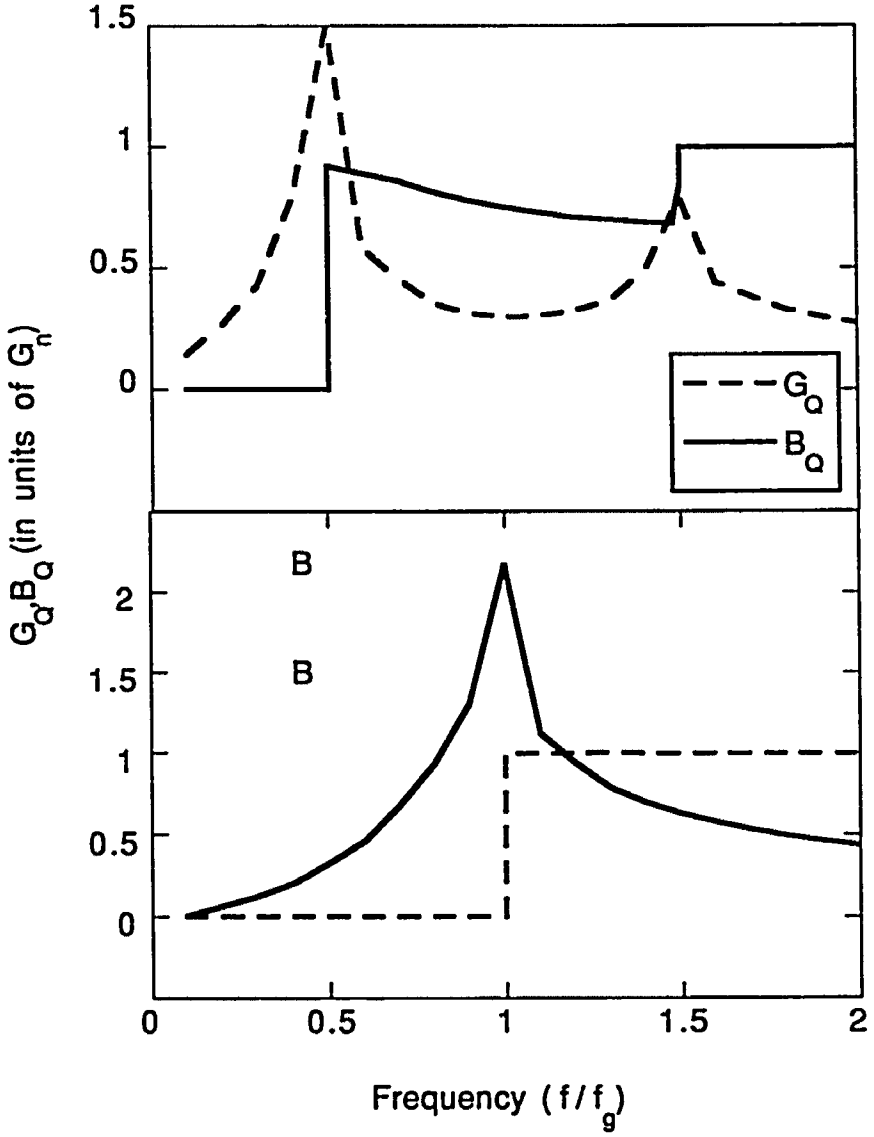

Fig. 7.9: The dependence of the quasiparticle conductance and susceptance on frequency for two dc bias voltages. This is for an ideal (BCS) Niobium tunnel junction. When dc biased at zero voltage (bottom) there is an onset of the conductance at the gap frequency. The susceptance has a logarithmic peak at this frequency. This is the form of the general quasiparticle response function. When biased at $V_g/2$ (top), the onset of the conductance is at a smaller frequency, and there is a second peak corresponding to twice the gap.

VIII - Conclusions:

A superconducting heterodyne receiver with no mechanical tuners was designed and tested. This receiver performed as well as other receivers in this frequency range. Mixer gain larger than one was observed over the full frequency range for some devices. This is a very encouraging result for constructing higher frequency detectors and arrays using a similar design.

The full bias dependence of the quasiparticle susceptance and conductance for various power levels was measured for the first time. This is significant for applications but also for verifying existing theories of superconductive tunneling. Our results agree well with theory.

The singularity in the quasiparticle susceptance at the gap voltage was observed for the first time. An analogy to a two-level atomic system was developed to explain the shape of the susceptance curve. This rather simplified model seems to provide at least an intuitive understanding of photon assisted tunneling. The measured reactive tunneling currents are significant in magnitude even when compared to the conductance. This reactive current was utilized as the first electronically variable tuning element for a superconducting mixer. Finally, an electronically variable superconducting phase shifter was proposed. Theoretical performance of such a circuit element was presented. Such an element would be applicable in telecommunications and signal processing.

References

Anlage, S.M., H.J. Snortland, and M.R. Beasley, IEEE Trans. Magn. 25, 1388 (1989).

Atwater, H.A., IEEE Trans. Microwave Theory Tech. MTT-31, 488 (1983).

Bardeen, J., L. Cooper, and J.R. Schrieffer, Phys. Rev. 108, 1175 (1957).

Bardeen, J., Phys. Rev. Lett. 6, 57 (1961).

Barone, A. and G. Paterno, Physics and Applications of the Josephson Effect, Wiley, New York, (1982).

Beasley, M.R. and H.J. Snortland, Technical Report RL-TR-92-156 available from RL (ERAA) Hanscom AFB MA 01731-5000, (1992).

Belitsky, V.Yu. and M.A. Tarasov, IEEE Trans. Magn. MAG-27, 2638 (1991).

Blaney, T.G., in Infrared and Millimeter Waves, K.J. Button Ed., pg. 62 (Academic, New York, 1980).

Blundell, R. and D. Winkler, to be published in NATO Applied Research Workshop on Superconducting Electronics and 2nd Workshop on Josephson Devices, (Plenum, London, 1991).

Blundell, R., and C.-Y. E. Tong, Proc. IEEE 80, 1702 (1992).

Bruynseraede, Y., C. Vlekken, C. Van Haesendonck, in Superconducting Electronics, edited by H. Weinstock and M. Niesenoff, p35 (Springer-Verlag, Berlin, 1989).

Büttgenbach, T.H., R.E. Miller, M.J. Wengler, D.M. Watson, and T.G. Phillips, IEEE Trans. Microwave Theory and Tech. MTT-36, 1720 (1988).

Büttgenbach, T.H., H.G. LeDuc, P.D. Maker, and T.G. Phillips, IEEE Trans. Appl. Superconductivity, 2, 165 (1992).

Caves, C.M., Phys. Rev. D 26, 1817 (1982).

Claasen, J.H., and P.L. Richards, J. Appl. Phys., 49, 4117 (1978).

Cohen, M.H., L.M. Falicov, and J.C. Phillips, Phys. Rev. Lett. 8, 316 (1962).

Collin, R.E., Proc. IRE 43, 179 (1955).

D'Addario, L.R., Int. J. Infrared Millimeter Waves 5, 1419 (1984).

D'Addario, IEEE Trans. Microwave Theory and Tech. MTT-36, 1103 (1988).

Dayem, A.H. and R.J. Martin, Phys. Rev. Lett. 8, 246 (1962).

Dicke, R.H., Rev. Sci. Instr. 17, 268 (1946).

Dolan, G.J., T.G. Phillips, and D.P. Woody, Appl. Phys. Lett. 34, 347 (1979).

Dunn,V.E., N.E. Hodges, O.A. Sy, W. Alyassini, M. Feng, and Y.C. Chang, IEEE MTT-S Digest, B-4, vol. I , 127 (1989).

Durand, D.J., J. Carpenter, E. Ladizinsky, L. Lee, C. Jackson, A. Silver, A.D. Smith, IEEE Trans. Appl. Superconductivity 2, 33 (1992).

Ellison, B.N. and R.E. Miller, Int. J. Infrared and Millimeter Waves, 8, 609 (1987).

Face, D.W., D.E. Prober, W.R. McGrath, and P.L. Richards, Appl. Phys. Lett. 48, 1098 (1986).

Feldman, M.J., S. Rudner, T. Claeson, J. Appl. Phys. 51, 5060 (1980).

Feldman, M.J., J. Appl. Phys. 53, 584 (1982).

Feldman, M.J. and S. Rudner, Rev. of Infrared and Millimeter Waves 1, ed. K.J. Button (Plenum, New York 1983), p. 47.

Feldman, M.J., S.-K. Pan, and A.R. Kerr, IEEE Trans. Magn. MAG-19, 494 (1983).

Feldman, M.J., IEEE Trans. Magn. MAG-23, 1054 (1987a).

Feldman, M.J. and D.W. Face, Jap. Jour. of Appl. Phys. 26, 1633 (1987b).

Feldman, M.J., unpublished notes.

Fisher, J.C. and I. Giaever, J. Appl. Phys. 32, 172 (1961).

Goldsmith, P.F., in Infrared and Millimeter Waves, 6, Ed. K.J. Button: Academic Press, 335, 1982.

Gundlach, K.H., in Superconducting ELectronics, edited by H. Weinstock and M. Niesenoff, p259 (Springer-Verlag, Berlin, 1989).

Harris, R.E., Phys. Rev. B10, 84 (1974).

Harris, R.E., Phys. Rev. B11, 3329 (1975).

Hicks, R.G., M.J. Feldman, and A.R. Kerr, IEEE Trans. Magn. MAG-21, 208 (1985).

Hines, M.E., Proc. IEEE, 697 (June 1964).

Hoefer, W.J.R. and M.N. Burton, IEEE Trans. Microwave Theory Tech. MTT-30, 2190 (1982).

Hopfer, S., IRE Trans. Microwave Theory Tech. MTT-3, 20 (1955).

Hu, Q., C.A. Mears, P.L. Richards, and F.L. Lloyd, IEEE Trans. Magn. MAG-25, 1380 (1989).

Hu, Q., C.A. Mears, P.L. Richards, and F.L. Lloyd, Phys. Rev. Lett. 64, 2945 (1990a).

Hu, Q., C.A. Mears, P.L. Richards, and F.L. Lloyd, Phys. Rev. B42, 10250 (1990b).

Irwin, K.E., S.E. Schwartz, and T. Van Duzer, in Digest of the Sixth International Conference on Infrared and Millimeter Waves, K.E. Button, ed., M-4-2 (1981).

Javadi, H.H.S., W.R. McGrath, B. Bumble, H.G. LeDuc, Appl. Phys. Lett. 61, 2712 (1992).

Josephson, B.D., Phys. Letters 1, 251 (1962).

Kanter,H., and F. Vernon, J. Appl. Phys., 43, 3174 (1972).

Ke, Q. and M.J. Feldman, to appear in IEEE Trans. Microwave Theory & Tech., March (1993).

Kerr, A.R., S.-K. Pan, and M.J. Feldman, and A. Davidson, Physica 108B, 1369 (1981).

Kerr, A.R., S.-K. Pan, and M.J. Feldman, Int. J. Infrared and Millimeter Waves 9, 203 (1988).

Kerr, A.R. and S.-K. Pan, in Proc. First Int. Symp on Space Terahertz Tech., (1990).

Kerr, A.R., S.-K. Pan, S. Whiteley, M. Radparvar, and S. Faris, IEEE Microwave Theory Tech. MTT-S Digest, 851 (1990).

Kerr, A.R., S.-K. Pan, A.W. Lichtenberger, and D.M. Lea, IEEE Microwave and Guided Wave Lett. 2, 454 (1992).

Kerr, A.R., S.-K. Pan, S. Withington, to appear in IEEE Trans. Microwave Theory & Tech., March (1993).

Kleinsasser, A.W., F.M. Rammo, M. Bhushan, Appl. Phys. Lett. 62, 1017 (1993).

Kroger, H., L.N. Smith, and D.W. Jillie, Appl. Phys. Lett. 39, 280 (1981).

Lee, G.S., Appl. Phys. Lett. 41, 291 (1982).

Liboff, R.L. and G.C. Dalman, Transmission Lines, Waveguides, and Smith Charts, (Macmillan, New York, 1985), Chap. 4.

Lichtenberger, A.W., C.P. McClay, R.J. Mattauch, M.J. Feldman, S.-K. Pan, and A.R. Kerr, IEEE Trans. Magn. MAG-25, 1247 (1989).

Lichtenberger, A.W., D.M. Lea, C. Li, F.L. Lloyd, M.J. Feldman, M.J. Mattauch, S.-K. Pan, and A.R. Kerr, IEEE Trans. Magn. MAG-27, 3168 (1991).

Likharev, K.K., Rev. Mod. Phys. 51, 101 (1979).

Liu, H.C., Phys. Rev. B43, 12538 (1991).

Lubecke, V., W.R. McGrath, and D.B. Rutledge, International J. Infrared and Millimeter Waves, 12, 1387 (1991).

Mears, C.A., Qing Hu, and P.L. Richards, IEEE Trans. Magn. MAG-25, 1050 (1989).

Mears, C.A., Qing Hu, P.L. Richards, A.H. Worsham, D.E. Prober, A.V. Räisänen, Appl. Phys. Lett. 57, 2487 (1990).

Mears, C.A., Qing Hu, P.L. Richards, A.H. Worsham, D.E. Prober, A.V. Räisänen, IEEE Trans. Magn. MAG-27, 3363 (1991a).

Mears, C.A., Qing Hu, and P.L. Richards, IEEE Trans. Magn. MAG-27, 3384 (1991b).

McDonald, D. G., R.L. Peterson, C.A. Hamilton, R.E. Harris, and R.L. Kautz, IEEE Trans. Electron Devices, 27 1945 (1980).

McGrath, W.R., P.L. Richards, A.D. Smith, H. Van Kempen, R.A. Batchelor, D.E. Prober, and P. Santhanam, Appl. Phys. Lett. 39, 655 (1981).

McGrath, W.R., A.V. Räisänen, and P.L. Richards, IEEE Trans. Magn. MAG-21, 212 (1985).

McGrath, W.R., Ph.D. Thesis, UC Berkeley (1985).

McGrath, W.R., P.L. Richards, D.W. Face, D.E. Prober, and F.L. Lloyd, J. Appl. Phys. 63, 2479 (1988).

Michelson, P.F., R. Giffard, IEEE Trans. Magn., MAG-17, 815 (1981).

Moreno, T., Microwave Transmission Design Data, (Dover, New York, 1948), Chap. 7.

Pan, S.-K. and A.R. Kerr, NASA Technical Memorandum 87792, July, 1986.

Pan, S.-K., A.R. Kerr, M.J. Feldman, A.W. Kleinsasser, J.W. Stasiak, R.L. Sandstrom, and W.J. Gallagher, IEEE Trans. Microwave Theory Tech. MTT-37, 580 (1989).

Phillips, T.G., D.P. Woody, G.J. Dolan, R.E. Miller, and R.A. Linke, IEEE Trans. Magn. MAG-17, 684 (1981).

Phillips, T.G. and G.J. Dolan, Physica 109 and 110B, 2010, (1982).

Phillips, T.G., and J. Keene, Proc. IEEE 80, 1662 (1992).

Räisänen, A.V., D.G. Crété, P.L. Richards, and F.L. Lloyd, Int. J. Infrared and Millimeter Waves 7, 1835 (1986).

Räisänen, A.V., D.G. Crété, P.L. Richards, and F.L. Lloyd, IEEE Trans. Microwave Theory and Tech. MTT-S Digest, 929 (1987).

Ralston, R., private communication.

Rascoe, D. L., et al., IEEE Trans. Microwave Theory & Tech., 37, 2165 (1989).

Rifkin,R., S.D. Deaver, Phys. Rev. B, 13, 3894 (1976).

Rudner, S. and T. Claeson, J. Appl. Phys. 50, 7070 (1979).

Rudner, S., M.J. Feldman, E. Kollberg, and T. Claeson, IEEE Trans. Magn. MAG17, 690 (1981).

Ruggiero, S.T., E.K. Track, D.E. Prober, G.B. Arnold, and M.J. DeWeert, Phys. Rev. B34, 217 (1986).

Schoelkopf, R.J., T.G. Phillips, and J. Zmuidzinas, to be published in IEEE Trans. Appl. Superconductivity (1993).

Skalare, A., Int. J. Infrared and Millimeter Waves 10, 1339 (1989); see also Internal Report, S.R.O.N. Space Res. Lab., Groningen, Netherlands, (1989).

Smith, A.D., W.R. McGrath, P.L. Richards, H. Van Kempen, D. Prober, and P. Santhanam, Physica B+C 108, 1367 (1981).

Smith, A.D., J.A. Carpenter, D.J. Durand, and L. Lee, IEEE Trans. Magn. MAG-27, 3370 (1991).

Spencer, E.G. and J.M. Rowell, IEEE Trans. Magn., MAG-17, 322 (1981).

Sutton, E.C., IEEE Trans. Microwave Theory Tech., MTT-31, 589 (1983).

Syrett, B.A., IEEE Trans. Microwave Theory Tech. MTT-28, 925 (1980).

Terman, F.E., in Radio Engineers Handbook, New York: McGraw Hill, p.51 (1943).

Tien, P.K. and J.P. Gordon, Phys. Rev. 129, 647 (1963).

Tinkham, M., Introduction to Superconductivity, McGraw Hill, New York, (1975).

Tong, C.E. and R. Blundell, IEEE Trans. Microwave Theory and Tech. MTT-38, 1391 (1990).

Torrey, H.C. and C.A. Whitmer, Crystal Rectifiers, New York: McGraw Hill, MIT Radiation Laboratory Series Vol. 15, 1948.

Track, E.K., Z-Y Shen, H. Dang, M. Radparvar, and S.M. Faris, IEEE Trans. Magn. 27, 2700 (1991).

Tucker, J.R., IEEE J. Quantum Electron. QE-15, 1234 (1979).

Tucker, J.R., Appl. Phys. Lett. 36, 477 (1980).

Tucker, J.R. and M.J. Feldman, Rev. Mod. Phys. 57, 1055 (1985).

Ugras, N.G., A.H. Worsham, D. Winkler, and D.E. Prober, submitted to Appl. Phys. Lett. (1993).

Van Duzer, T. and C.W. Turner, Principles of Superconducting Devices and Circuits, Elsevier North Holland, New York (1981).

Van Duzer, T. in Superconducting Electronics, edited by H. Weinstock and M. Niesenoff, (Springer-Verlag, Berlin, 1989).

Verghese, S., private communication (1993).
Vincent, D.A. and B.S. Deaver, Jr., Phys. Rev. Lett. 32, 212 (1974).

Vinding, V.P., NEREM RECORD, 108 (1967).

Vowinkel, K. Eigler, W. Hilberath, K. Jacobs, and P. Muller, Int. J. Infrared and Millimeter Waves 10, 579 (1989).

Wengler, M.J. and D.P. Woody, IEEE J. Quantum Electron. QE-23, 613 (1987).

Wengler, M.J. Proc. IEEE 80, 1810 (1992).

Werthamer, N.R., Phys. Rev. 147, 255 (1966).

Winkler, D., Ph.D. dissertation, ISBN 91-7032-307-0 Department of Physics, Chalmers University of Technology, S-412 96 Gothenburg, Sweden, May 1987.

Winkler, D., N.G. Ugras, A.H. Worsham, D.E. Prober, N.R. Erickson, and P.F. Goldsmith, IEEE Trans. Magn. MAG-27, 2634 (1991a).

Winkler, D., N.G. Ugras, A.H. Worsham, D.E. Prober, N.R. Erickson, and P.F. Goldsmith, in progress (1993).

Withington, S. and E.L. Kollberg, IEEE Trans. Microwave Theory and Tech. MTT-37, 231 (1989).

Worsham, A.H., D.E. Prober, J.H. Kang, J.X. Przybysz, and M.J. Rooks, IEEE Trans. Magn., MAG-27, 3165 (1991a).

Worsham, A.H., N.G. Ugras, D. Winkler, D.E. Prober, N.R. Erickson, and P.F. Goldsmith, Phys. Rev. Lett. 67, 3034 (1991b).

Xizhi, Li, P.L. Richards, and F.L. Lloyd, Int. J. Infrared and Millimeter Waves 6, 697 (1985).

Yariv, A., Quantum Electronics, 2nd ed. (Wiley, New York, 1975), Chapter 8.

Zmuidzinas, J. and H. LeDuc, IEEE Trans. Microwave Theory and Tech., 1992.

Zorin, A.B., I.O. Kulik, K.K.Likharev, J.R.Schrieffer, Sov. J. Low Temp. Phys. 5, 537 (1979).